Technical Report Documentation Page

1. Report No.	2. Government Accession No.	3. Recipient's Catalog No.
FHWA/TX-13/0-6491-1		

4. Title and Subtitle	5. Report Date
EVALUATION OF CONCRETE STRUCTURES AFFECTED BY ALKALI-SILICA REACTION AND DELAYED ETTRINGITE FORMATION - PART 2	December 2012 Published: May 2013
	6. Performing Organization Code
7. Author(s)	8. Performing Organization Report No.
Paolo Gardoni, Alex Pagnotta, Qindan Huang, and David Trejo	Report 0-6491-1
9. Performing Organization Name and Address	10. Work Unit No. (TRAIS)
Texas A&M Transportation Institute College Station, Texas 77843-3135	
	11. Contract or Grant No.
	Project 0-6491
12. Sponsoring Agency Name and Address	13. Type of Report and Period Covered
Texas Department of Transportation Research and Technology Implementation Office P.O. Box 5080 Austin, Texas 78763-5080	Technical Report: September 2009 – August 2012
	14. Sponsoring Agency Code

15. Supplementary Notes

Project performed in cooperation with the Texas Department of Transportation and the Federal Highway Administration.

Project Title: Non-destructive Evaluation of In-service Concrete Structures Affected by Alkali-Silica Reaction (ASR) or Delayed Ettringite Formation (DEF)

URL: http://tti.tamu.edu/documents/0-6491-1.pdf

16. Abstract

This report details the results of a comprehensive research project aimed at evaluating the potential use of non-destructive testing (NDT) to assess structures affected by ASR and/or DEF. This project was a collaborative effort between the University of Texas at Austin and Texas A&M University (TAMU). The results presented in this report are those obtained by the team at TAMU. Available data on the performance of large-scale samples exhibiting alkali-silica reaction (ASR) and/or delayed ettringite formation (DEF) are presented, and the analysis of these data shows that steel-concrete bond is affected by ASR/DEF. Multiple techniques for assessing the steel-concrete interface are presented, and the impact-echo method is selected for further study. A small-scale laboratory experiment using impact-echo shows that this technique has the potential to detect ASR/DEF-induced defects at the steel-concrete interface. The application of impact-echo to large-scale samples with ASR yields inconclusive results, and further work is needed to determine if impact-echo can be used to assess the steel-concrete interface of ASR/DEF-affected field structures.

17. Key Words	18. Distribution Statement
Concrete, Non-destructive Testing, ASR, DEF	No restrictions. This document is available to the public through NTIS: National Technical Information Service Alexandria, Virginia http://www.ntis.gov

19. Security Classif.(of this report)	20. Security Classif.(of this page)	21. No. of Pages	22. Price
Unclassified	Unclassified	130	

Form DOT F 1700.7 (8-72) Reproduction of completed page authorized

EVALUATION OF CONCRETE STRUCTURES AFFECTED BY ALKALI-SILICA REACTION AND DELAYED ETTRINGITE FORMATION - PART 2

by

Paolo Gardoni, Alex Pagnotta, Qindan Huang, and David Trejo

Report 0-6491-1
Project 0-6491
Project Title: Non-destructive Evaluation of In-service Concrete Structures Affected by Alkali-Silica Reaction (ASR) or Delayed Ettringite Formation (DEF)

Performed in cooperation with the
Texas Department of Transportation
and the
Federal Highway Administration

December 2012
Published: May 2013

TEXAS A&M TRANSPORTATION INSTITUTE
College Station, Texas 77843-3135

DISCLAIMER

This research was performed in cooperation with the Texas Department of Transportation (TxDOT) and the Federal Highway Administration (FHWA). The contents of this report reflect the views of the authors, who are responsible for the facts and the accuracy of the data presented herein. The contents do not necessarily reflect the official view or policies of the FHWA or TxDOT. This report does not constitute a standard, specification, or regulation.

ACKNOWLEDGMENTS

This project was conducted at Texas A&M University and was supported by the Texas Department of Transportation and the Federal Highway Administration through the Texas Transportation Institute. The authors acknowledge the efforts and contributions of the TxDOT project director, Andy Naranjo, and the members of the Project Monitoring Committee, including Brian Merrill, Geetha Chandar, Leon Flournoy, Eliza Paul, Paul Rollins, and Jeff Tomkins. The authors are grateful and are especially proud of the graduate student researchers involved in the research program including Jason Zidek, Armin Tabandeh, and Shih-Hsiang Liu. The authors thank Dr. Peter Keating and Mr. Matt Potter of the Civil Engineering High-Bay Structural and Materials Laboratory at Texas A&M University for their technical and logistical assistance.

TABLE OF CONTENTS

Page

LIST OF FIGURES

Page

LIST OF TABLES

Page

1 INTRODUCTION

Alkali-silica reaction (ASR) has been identified in reinforced concrete (RC) bridge columns, and petrographic analysis has indicated the presence of expansive ASR products at the interface between concrete and reinforcing steel, possibly changing the steel-concrete bond behavior. Additionally, the potential for delayed ettringite formation (DEF) in RC bridge columns may also alter the bond behavior. A decrease in bond strength in regions critical to the development of reinforcing steel, such as locations where bars are lapped for reinforcement continuity (lap-splice regions), may lead to changes in the flexural capacity of and/or demand on the column. Such changes may subsequently reduce the reliability of the column. The effect of ASR and/or DEF on bond behavior is a clear concern that needs to be explored. In particular, a tool is needed to assess the bond in critical areas of RC columns exhibiting ASR and/or DEF such that the reliability and safety of the structure can be assessed. The work that was part of TxDOT Project 0-6491 that was led by the Texas A&M University/Texas A&M Transportation Institute (TAMU/TTI) team focused on assessing the ability of non-destructive evaluation (NDE) to identify and quantify ASR/DEF-induced distress. In particular, the TAMU/TTI team developed bond-slip models that are a function of the ASR damage, identified an NDE testing strategy, and provided appropriate analyses of the collected data.

Exploring the effects of ASR/DEF on the performance of lap-splices in RC columns was the subject of TxDOT Project 0-5722. As part of this project, multiple large-scale column specimens were constructed and allowed to develop ASR and/or DEF through the use of susceptible materials and harsh exposure conditions. At different levels of ASR/DEF deterioration, selected specimens were load-tested in flexure, and the force-displacement results were recorded. The results of these load tests are used as part of TxDOT Project 0-6491 to calibrate the bond-slip models for ASR-affected reinforcing bars.

Furthermore, multiple methods for NDE of concrete are examined, and one particularly favorable method, impact-echo, is selected for further study. A small-scale experiment is designed to examine samples containing deliberate defects with varying dimensions using impact-echo. A procedure is established based on the results of this experiment, and a preliminary NDE assessment of the large-scale specimens cast as part of TxDOT Project 0-5722 is performed.

2 REVIEW AND DISCUSSION OF TXDOT 0-5722

2.1 INTRODUCTION

This chapter describes the large-scale specimens that were constructed and destructively tested as part of TxDOT Project 0-5722. The specimens were under varying levels of deterioration due to ASR. The test results will be used in the next chapter to examine the effect of ASR on the bond behavior between the rebar and the concrete. Specifically, this chapter first reviews the design of the large-scale specimens, the deterioration environment, and the results from the load testing. Then, the chapter offers a critical analysis and interpretation of the results focusing on the physical reasons that could explain the testing results. The details about the construction materials and specimen construction can be found in Bracci et al. (2011).

2.2 EXPERIMENTAL DESIGN

2.2.1 Specimen Design

One of the objectives of TxDOT Project 0-5722 was to evaluate experimentally the behavior of large-scale specimens of bridge columns within a critical lap splice region considering different levels of ASR deterioration. The large-scale specimens were designed to use the common splice typically found at the connection between the column and foundation in the non-seismic regions.

Sixteen large-scale column specimens were constructed. The specimens have 2 ft × 4 ft (0.61 m × 1.2 2m) cross section with six #11 bars overlapped in the 9 ft (2.74 m) splice region. Figure 2-1 shows the dimensions and rebar layouts.

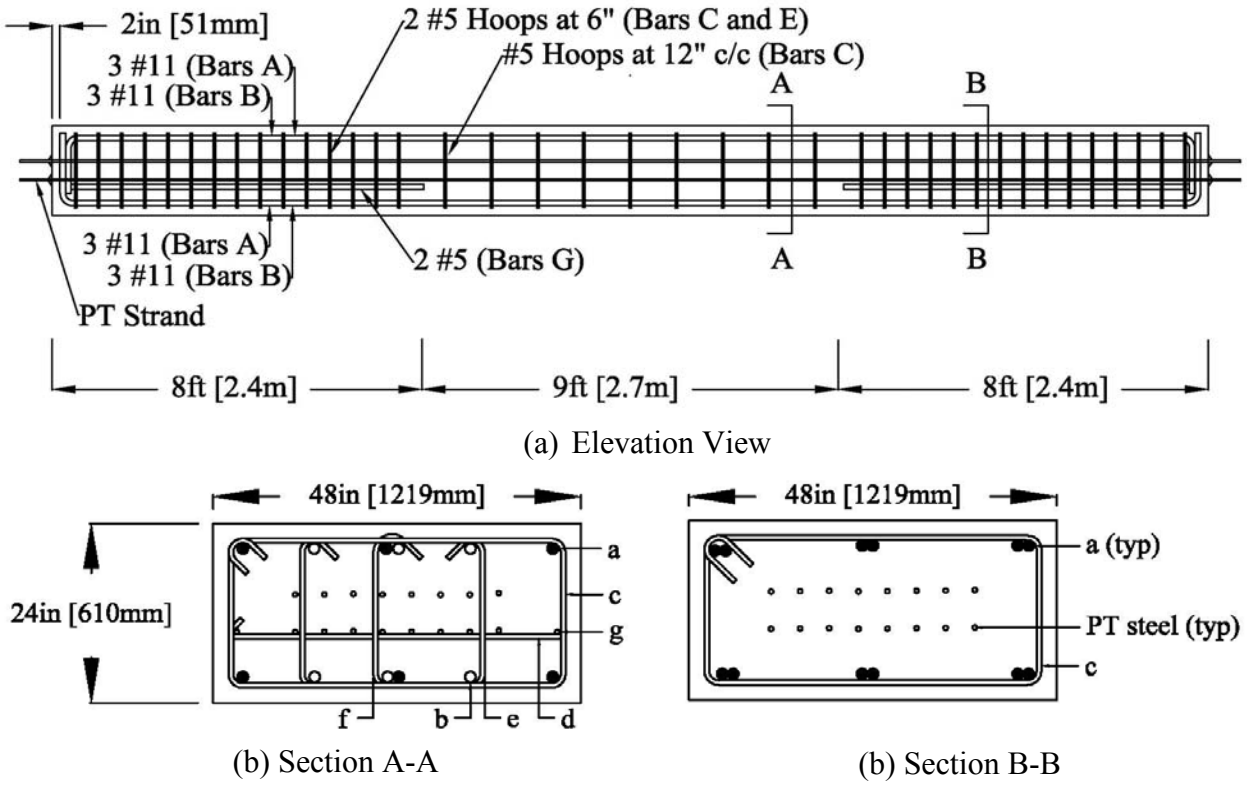

Figure 2-1. Large-Scale Geometry and Reinforcement Layout.

The splice length was overdesigned using $2.1l_d$, where l_d is the development length calculated based on ACI-318 (2008) and AASHTO LRFD Bridge Design Specifications (2007). Corresponding to $2.1l_d$, a 9 ft (2.74 m) splice length was provided, which is overdesigned by 54 percent. Thus, the test results can be used to check whether the deterioration due to ASR on the bond in the splice region overcomes the conservative design.

To simulate the axial compressive load present in actual bridge columns, a post-tensioning (PT) system consisting of 16 – 0.6 in. (15.24 mm) diameter, unbonded, steel strands was added. The strands were hydraulically jacked to 70 percent of their ultimate tensile stress, resulting in an initial compression load N_0 = 580.5kips (130.5 kN) on the specimens. This level of compression is about 10 percent of the column compressive capacity, which is commonly used as a service load in bridge design.

To measure the internal strains due to ASR expansion and applied load, several electronic strain sensors were installed in the column specimens. Figure 2-2 shows the location of the 10 strain gages (SG1-SG10) that were placed on the longitudinal rebars in the splice region. No

strain gages were installed on two control columns, C1 and C2, as no ASR is expected in these specimens.

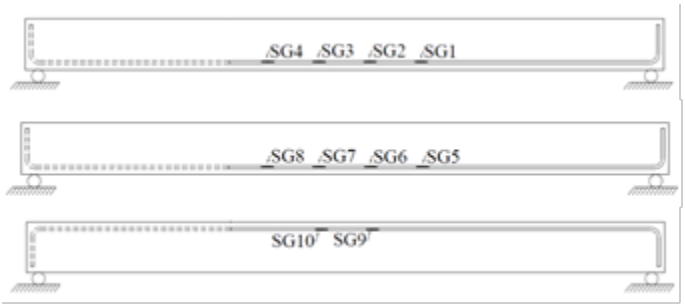

Figure 2-2. Longitudinal Strain Gage Locations.

2.2.2 Exposure Program

The previous study shows that the ASR progresses faster due to the moisture and warmer temperature (Multon et al. 2005, Folliard et al. 2006). Therefore, to accelerate the ASR formation, the specimens were exposed to atmospheric conditions in Texas and wetting for 15 minutes four times a day. Two specimens, C1 and C2, were used as the control specimens and they were stored indoors without being exposed to outside weather conditions or moisture to minimize ASR and/or DEF deterioration. The remaining 14 specimens were subject to accelerated wet-dry cycles to accelerate the development of ASR. Different exposure times were used to develop different levels of ASR deterioration. Up to date, eight specimens (including the two control specimens) were tested destructively at different levels of ASR damage (two columns for each level) to determine the reduction in capacity due to the ASR deterioration, if any. The remaining eight specimens continue to be exposed to deteriorating conditions to generate more severe damage possibly from DEF. As discussed in the concluding remark, the remaining specimens provide an opportunity to implement the technique developed as part of this project on more severely damaged specimens.

2.2.3 Four Point Load-Test Program

For the design of the bridge columns in non-seismic zones, the splice region is typically located directly above the foundation. Therefore, the peak overturning moments caused by the lateral loading occurs at the column-foundation interface, where the splice region is (Figure 2-3). To study the flexural capacity of the splice regions, a four-point load test was conducted under

displacement controlled monotonic loading as shown in Figure 2-4, where the actuators were placed at the ends of the splice region. For the experimental program, the two forces under the actuators were taken to be the same, creating a constant moment throughout the length of the splice region. By increasing the applied lateral load, cracking, yielding, and eventual failure can be observed in the weakest section of the columns, which is at the end of splices.

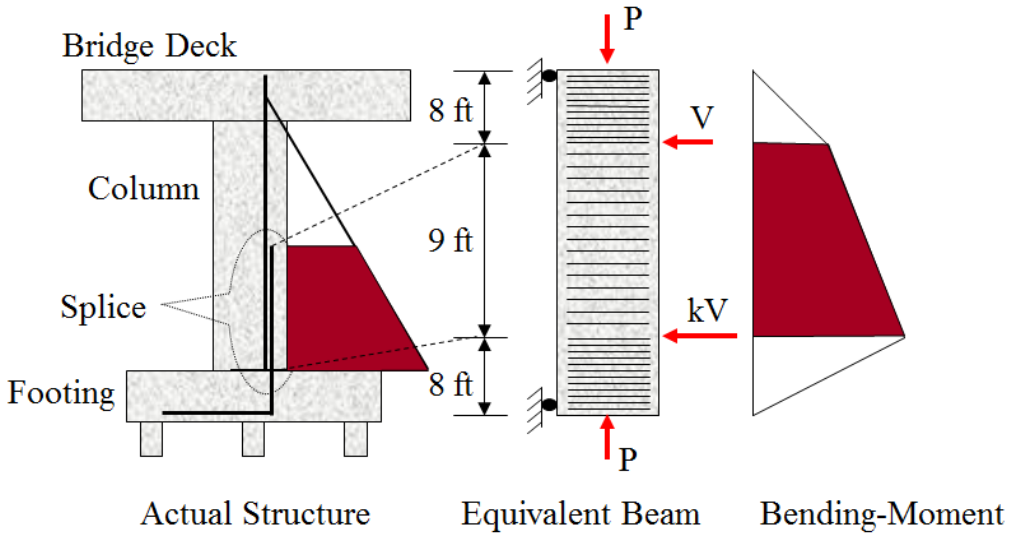

Figure 2-3. Bending Moment Diagram in Actual Columns.

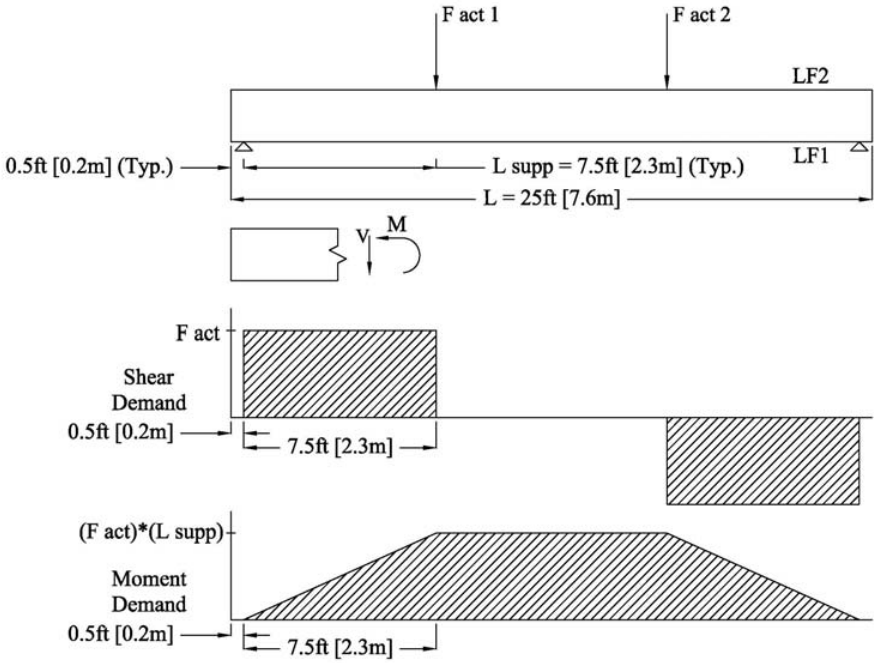

Figure 2-4. Four-Point Load Test.

2.3 EXPOSURE CONDITIONS

At the exposure site, the specimens were placed on their short side with about 3 ft (0.91 m) clear distance between the specimens. The clear space between the specimens allowed the specimens' faces to experience direct sunlight. The average annual temperature was 69°F (23°C), and the average precipitation was 1008 mm (39.7 in.). Additionally, each side of specimens was watered artificially through a sprinkler system, as shown in Figure 2-5.

To provide more uniform expansion throughout the specimens, the specimens were rotated twice: the first rotation was to place the short side that was on the bottom to the top; and the second rotation was to place one of the two large sides on the top. Table 2-1 gives the month and year of the specimen casting, initial exposure to the environmental conditions, 1st rotation, 2nd rotation, and final structural load testing.

Table 2-1. Key Dates for Eight Large Specimens and Degree of ASR.

Specimen #	Date					ASR stage
	Casting	Initial exposure	1st rotation	2nd rotation	Four-point load test	
C1 & C2	8/2008	N/A	N/A	N/A	2/2009	No damage
C3 & C4	6/2008	N/A	7/2008	7/2009	2/2010	Early stage
C5 & C6	1/2008 & 2/2008	5/2008	7/2008	7/2009	8/2010	Middle stage
C7 & C8	4/2008 & 5/2008	5/2008 & 7/2008	5/2008 & 7/2008	7/2009	7/2011	Later stage

The degree of ASR given the last column of the table is assessed as part of the work conducted as part of TxDOT Project 0-6491. The degree of ASR is assessed qualitatively based on the surface and internal expansion measurements and cracking throughout the specimen prior to the structural load testing and the petrographic analysis of concrete cores taken from specimens after the testing. For the petrographic analysis, three to seven cores were drilled near or though longitudinal and transverse reinforcement where there were large surface cracks. The reason of specifically choosing those locations was to exam if there was any ASR formation on the rebar-concrete interface that could result in deterioration in the bond and also to determine how deep the surface cracks propagated. The crack depth was a concern because deep crack could lead to other durability issues such as early corrosion of the reinforcement.

Figure 2-5. Sprinkler System between Two Specimens Load Testing Results.

As the results of the petrographic analysis, ASR gel, distressed aggregates, and micro cracking were present in the cores. ASR was found to be the primary cause of expansion in the cores. At the interface of the spliced rebar, a layer of ASR gel and was found. Ettringite was also found around the rebars, which indicated the possibility of debonding due to ASR deterioration. This behavior is depicted in Figure 2-6. Figure 2-6a shows a reinforcing bar surrounded by unaffected concrete. Figure 2-6b shows the defect at the interface of steel and concrete that is created as ASR gel begins to buildup. Figure 2-6c shows the initiation of a crack as the stress caused by the ASR gel exceeds the tensile strength of the concrete. Surface cracking was evident in all cores with some cracks being nearly 1 in. (25.4 mm) deep. For the purpose of the work conducted as part of TxDOT Project 0-6491, the deterioration is categorized into four levels, no damage (Specimens C1 and C2), early stage (Specimens C3 and C4), middle stage (Specimens C5 and C6), and later stage (Specimens C7 and C8).

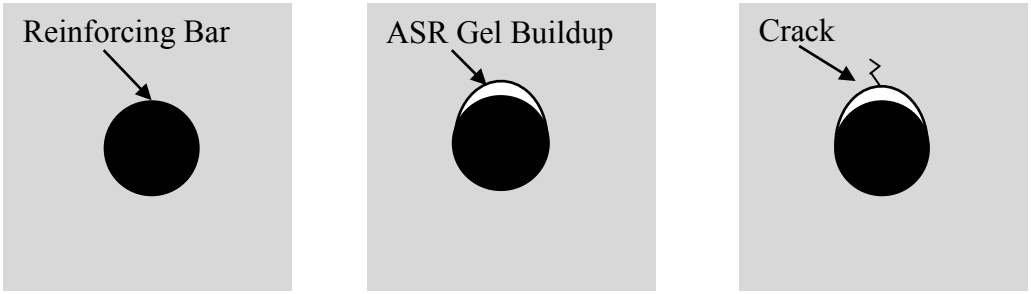

Figure 2-6. Depiction of the Formation of ASR Gel at the Interface between Steel Reinforcing Bars and Concrete.

Figure 2-7 shows the force-displacement relation obtained from the four-point load tests. For each specimen, there are two force-displacement curves: one for each loading point. Thus there are four curves for each ASR damage stage. The force was obtained from the actuator, and the deformation was measured by string pot measurements attached to the specimen under the loading point and the rigid laboratory strong floor. During the tests, the loading was stopped a few times to assess the condition of the specimen, which resulted in slight drops in load.

As part of the work conducted in TxDOT Project 0-6491, each force-displacement curve of test data is simplified into a tri-linear curve, as show in Figure 2-8, to have a clearer comparison of the column behavior. With this simplification, the force and displacement that correspond to the points of first cracking and first yielding can be clearly identified. All specimens have about the same initial stiffness until first cracking. The cracking point shifts to higher loads, the column post-cracking behavior becomes stiffer, and the yield point moves to lower displacements as ASR deterioration becomes more severe. The deteriorated specimens were about 25–35 percent stiffer and had a slight (5–15 percent) increase in yield strength than the two control specimens (C1 and C2) between first cracking and first yielding of the reinforcing steel. Furthermore, as the severity of ASR deterioration increases, the cracking point shifts to a higher load and displacement and the yield point is at a higher load and lower displacement.

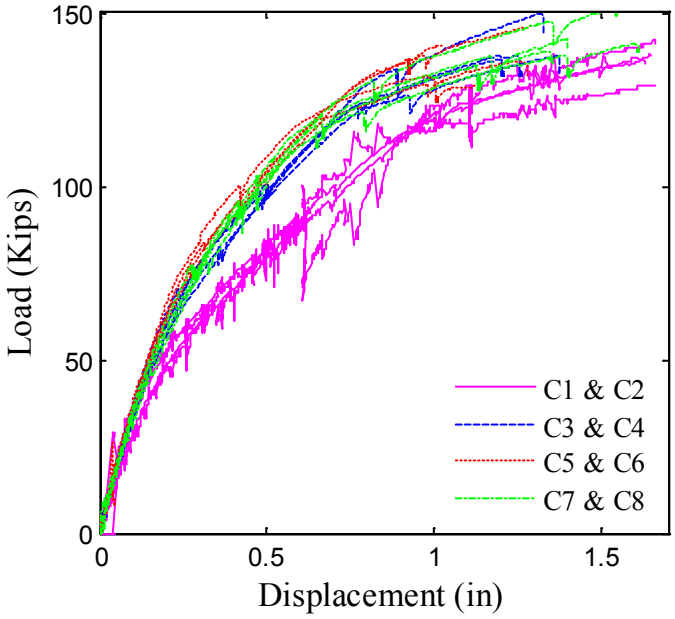

Figure 2-7. Force-Displacement Curve for the Four-Point Test at the Actuator Load Point (1 in. = 25 mm).

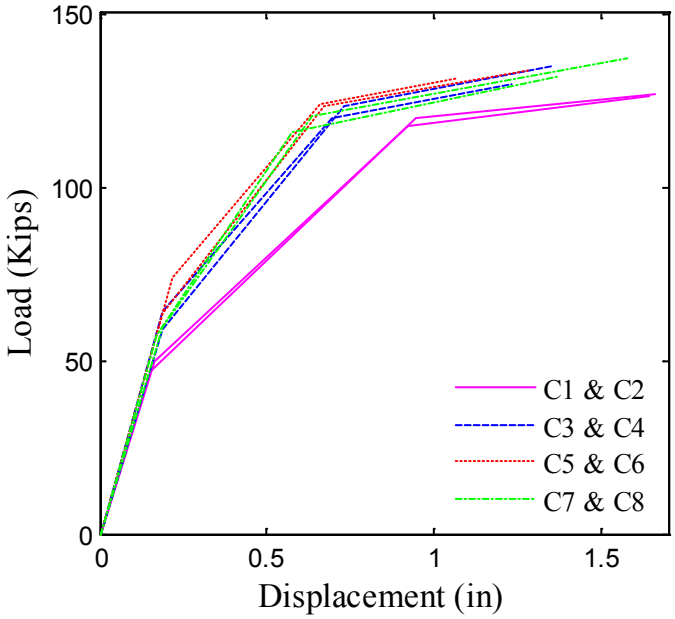

Figure 2-8. Simplified Tri-Linear Curves for Force-Displacement Curves (1 in. = 25 mm).

2.4 DISCUSSION OF RESULTS

Three factors may explain the different behavior between the control columns and deteriorated columns reported by TxDOT Project 0-5722:

1) The compressive strength is higher for the more deteriorated specimens (either because the strength increased with time due to the continued hydration of cement or because of slightly different concrete mixes).
2) Additional confining force and axial compressive load are generated as a result of the ASR expansion.
3) The behavior of the bond between the reinforcing steel and concrete changes due to ASR deterioration.

2.4.1 Concrete Ageing

To determine the compressive strength f_{cm} of the concrete in the column specimen at the time of the four-point load test, cylinder test samples with size 4 in. × 8 in. (102 mm × 204 mm) were made from the same batches of concrete used to construct the large scale specimens. For each column, three cylinder samples were made and placed with the column specimen during the same environmental conditions. All three cylinders were tested according to ASTM C39 (2001) in the same week as the load test for the corresponding large-scale specimen. Table 2-2 shows the test results for all the cylinders. It is found that the values of f_{cm} are larger for specimens exhibiting more damage.

Table 2-2. Cylinder Test Data of Compressive Strength for Column Specimens.

ASR stage	Specimen	Compressive strength, ksi (MPa)			
		Sample1	Sample 2	Sample 3	Average
No damage	C1	3.99 (27.49)	3.74 (25.79)	4.01 (28.25)	3.91 (26.96)
	C2	3.17 (21.89)	3.51 (24.19)	3.70 (25.51)	3.46 (23.56)
Early	C3	5.37 (37.03)	4.08 (28.14)	5.44 (37.53)	4.96 (34.20)
	C4	5.05 (34.84)	5.69 (39.23)	4.33 (29.85)	5.02 (34.61)
Middle	C5	5.28 (36.37)	5.01 (34.51)	5.62 (38.73)	5.30 (36.54)
	C6	5.08 (35.00)	6.61 (45.59)	3.90 (26.88)	5.20 (35.85)
Later	C7	6.10 (42.06)	6.21 (42.80)	5.83 (40.18)	6.05 (41.71)
	C8	5.25 (36.22)	5.45 (37.56)	5.03 (34.71)	5.24 (36.13)

2.4.2 Additional Axial and Confining Forces

When the PT strands are tensioned to the desired stress, a compressive force is generated that shortens the column specimen. In Figure 2-9, ε_0 indicates the initial strain resulting from the initial axial load N_0. When an expansion due to ASR occurs, an additional axial load, ΔN, is generated by the tensile strain, ε_s, which can be obtained from the readings of the strain gages, SG1 through SG10 (shown in Figure 2-3). Using the measurements of ε_s for each column specimen, the additional axial load is then calculated and the results are shown in Table 2-3. As expected, ΔN increases with time as the ASR expansion increases.

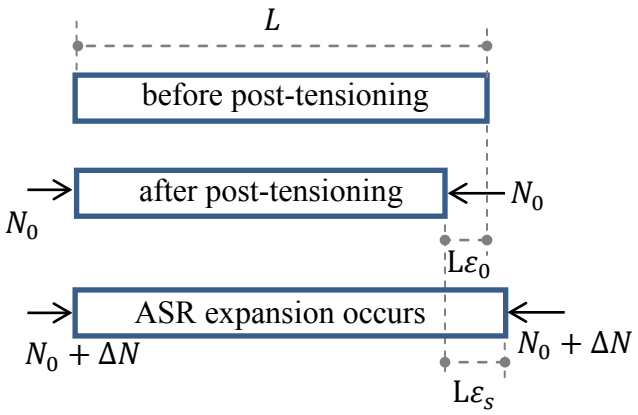

Figure 2-9. Additional Axial Load Generated by ASR Expansion.

The confining forces provided by the transverse reinforcement also change due to the ASR expansion. These confining forces could potentially increase the compressive strength of the confined concrete. However, a sensitivity analysis shows that the core concrete strength, which is influenced by the additional confining force, does not significantly contribute to the flexural stiffness.

Table 2-3. Additional Axial Load for Column Specimens due to ASR Expansion.

	ASR stage	Specimen	ΔN kips (kN)
Test 1	No Damage	C1	0
		C2	0
Test 2	Early Stage	C3	35.60 (145.01)
		C4	37.10 (165.03)
Test 3	Middle stage	C5	43.40 (193.05)
		C6	50.43 (224.32)
Test 4	Later stage	C7	47.38 (210.76)
		C8	54.03 (248.30)

2.4.3 Change in Bond Behavior

The third possible reason for different flexible behavior is a change in bond behavior due to ASR. However, assessing changes in the bond behavior is challenging, because bond behavior was not explicitly measured during the destructive testing conducted as part of TxDOT Project 0-5722. Therefore, a finite element (FE) model of the large-scale samples is developed to simulate the four-point testing and to assess the possible change in the bond behavior using the test data obtained from TxDOT Project 0-5722.

Figure 2-10 illustrates this process. For each specimen, a FE model is constructed and the four-point load test is simulated by conducting a static analysis. The FE model incorporates the information on the compressive strength and additional axial load provided earlier, and parameters in the bond model are used to match the force-displacement curves obtained from the destructive tests. The next chapter gives the details of FE model and the calibration process.

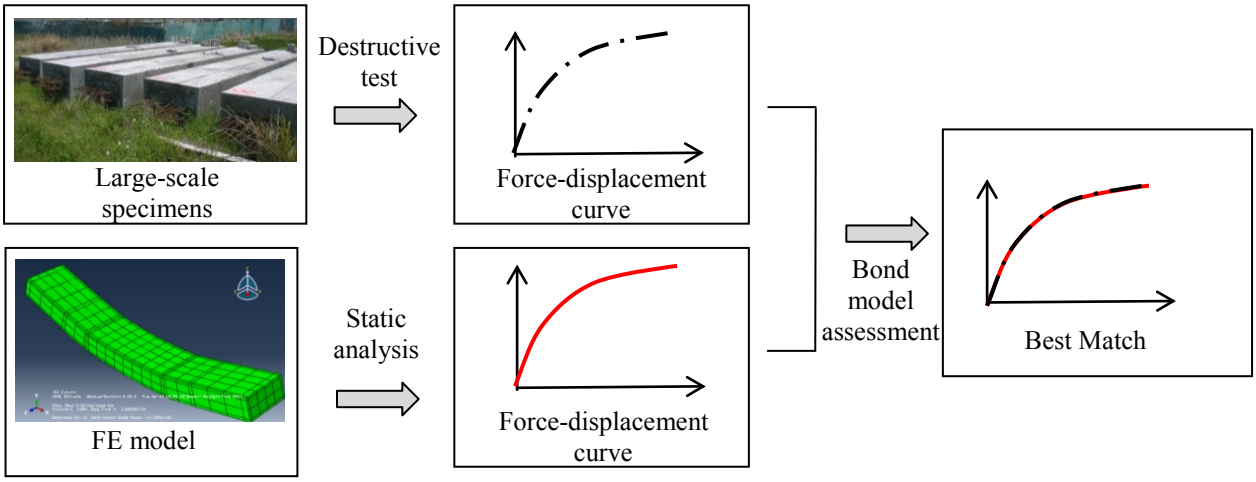

Figure 2-10. Process to Assess Changes in the Bond Behavior.

2.5 SUMMARY

Sixteen large-scale bridge column specimens were constructed and so far load tests were conducted on eight of them. The large-scale specimens were designed to use the common splice length found in the field at the connection between column and foundation. Among those eight specimens, two of them, C1 and C2, were the control specimens and did not experience ASR deterioration. The remaining six specimens, C3-C8, were subject to accelerated wet-dry cycles to accelerate the development of ASR.

The columns were tested destructively at different levels of ASR damage (two columns for each level) to determine the reduction in capacity due to ASR deterioration. As part of the work conducted as part of TxDOT Project 0-6491, the levels of deterioration were assessed qualitatively before the destructive testing based on the extent of concrete cracking as: no damage (C1 and C2), early stage (C3 and C4), middle/late stage (C5 and C6), and late stage (C7 and C8). Based on the experimental results, researchers found that the cracking point shifts to

higher loads, the post-cracking stiffness becomes greater, and the yield point moves to lower displacements as the ASR deterioration becomes more severe.

As part of TxDOT Project 0-6491, three factors were identified to possibly explain the different behavior between the control columns and deteriorated columns reported by TxDOT Project 0-5722: increase compressive strength, additional confining and change in bond behavior. To investigate these three factors, a finite element model needs to be developed. The next chapter gives further details about the development of the FE model and this investigation.

3 BOND-SLIP MODEL

3.1 INTRODUCTION

As the bond is critical to the development of reinforcing bars, any possible degradation in the bond behavior in the lap-splice region may affect the capacity of bridge columns. Studies evaluating structural capacity under ASR deterioration are limited, especially with respect to effects on the behavior of bond between the concrete and steel (Haddad and Numayr 2007; Swamy and Al-Asali 1989).

The goal of this chapter is to study the effect of ASR on the bond behavior in the lap-splice region using the experimental data obtained from the eight RC columns (C1-C8). As described in the previous chapter, a FE model of the RC columns is needed in order to use the test results given in terms of force-displacement curves. The FE model described in details in the next section explicitly models the bond-slip behavior.

The FE model will help investigate the three factors that may explain the different behavior between the control columns and deteriorated columns. In particular, by calibrating the bond-slip model while incorporating the changes in the compressive strength of concrete and the additional axial load, the effect of different stages of ASR on the bond can be obtained.

3.2 DESCRIPTION OF THE FINITE ELEMENT MODEL

For the FE model is developed using the commercial program Abaqus. Eight-node solid elements (C3D8) are used to model the concrete, and two node truss element (T2D2) are used to model the reinforcing steel bars. The FE model mesh, applied loading, and boundary conditions of the RC columns are shown in Figure 3-1. The properties are specified for both concrete and steel elements, and are described next.

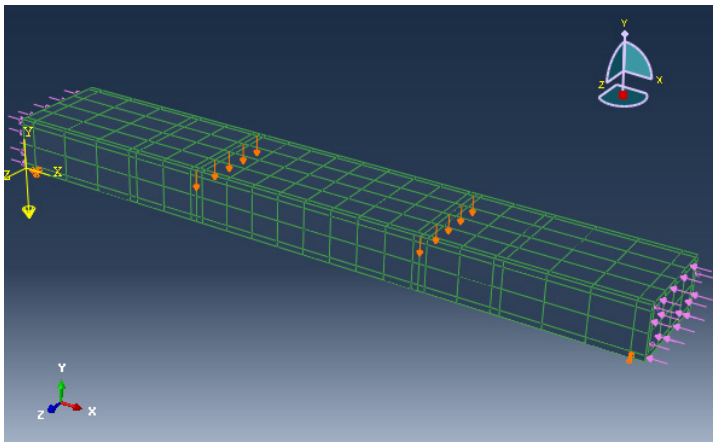

Figure 3-1. FE Model in Abaqus.

At the steel-concrete interface, the nodes of the concrete and the reinforcement share the same geometric location. Non-linear spring elements are used to connect each pair of nodes, explicitly modeling the bond-slip interface between concrete and reinforcement. The modeling assumes that the stiffness in the direction of the slip interface is rigid (Rots 1988) and only the stiffness along the slip interface is considered. The bond model used for the spring element is described in the next section.

The average of the compressive strengths obtained from the three cylinder samples (Table 3-2) are used as the value of f_{cm} in the FE model. Both an initial axial load N_0 and additional axial load ΔN generated by ASR-caused expansion need to be considered in the FE model. The total axial load $N = N_0 + \Delta N$ is simulated by adding compression pressure to the both ends of the column. All the specimens have the same axial load N_0 = 580.5 kips (130.5 kN) and ΔN is given in Table 2-3.

A static analysis is performed first under the axial load, N, and gravity. Then to simulate the four-point loading test conducted in Project TxDOT 0-5722, a displacement control method is used to obtain the force-displacement curve by incrementally increasing the displacement of the nodes at which the concentrated loads are applied.

The concrete is modeled using the concrete damaged plasticity model available in Abaqus by providing stress versus inelastic strain data. This concrete model is a continuum, plasticity-based, damage model and it assumes two failure mechanisms: tensile cracking and compressive crushing of the concrete material. The stress-strain relation is written as follows.

$$\frac{f_c}{f_c'} = \frac{n\left(\frac{\varepsilon_c}{\varepsilon_{co}}\right)}{n-1+\left(\frac{\varepsilon_c}{\varepsilon_{co}}\right)^n} \quad \text{(Eq. 3-1)}$$

$$\frac{f_t}{f_t'} = \frac{n\left(\frac{\varepsilon_t}{\varepsilon_{to}}\right)}{n-1+\left(\frac{\varepsilon_t}{\varepsilon_{to}}\right)^n} \quad \text{(Eq. 3-2)}$$

where f_c and ε_c = compressive stress and strain of concrete, respectively, $\varepsilon_{co} = 0.002$ = compressive strain corresponding to compressive strength, f_c', $n = E_c/(E_c - E_{\text{sec}})$ in which $E_c = 57000\sqrt{f_c'}$ (psi), and $E_{\text{sec}} = f_c'/\varepsilon_{co}$, $f_t' = 0.5\sqrt{f_c'}$ (MPa) = tensile strength of concrete, f_t and ε_t = tensile stress and strain of concrete, respectively, and $\varepsilon_{to} = \varepsilon_{to}\, f_t'/f_c'$. The average of the compressive strengths obtained from the three cylinder samples (Table 2-2) are used as the value of f_c' in the FE model. The rebar is modeled as having bilinear behavior with a Young's modulus of 29,000 ksi (200,000 MPa) and a yield stress of 70 ksi (483 MPa). The Poisson's and the strain-hardening ratios are taken as 0.2 and 1.5, respectively.

Incorporating the increase in the compressive strength into the FE model is not sufficient to explain the stiffness increase found in the experimental results. In addition, a sensitivity analysis shows that the core concrete strength, which is influenced by the additional confining force, does not significantly contribute to the flexural stiffness. Also, incorporating the additional axial load into the FE model is still not enough to model the stiffness increase shown in the experimental results. Therefore, the bond-slip behavior is explicitly modeled in the FE model to capture the effect of different stages of ASR on the force-displacement relationships of the tested specimens.

3.3 MODELING OF THE BOND-SLIP BEHAVIOR

The bond between the reinforcement and concrete is a complex behavior and it allows the stresses being transferred from the rebar to the surrounding concrete. The bond behavior determines the RC structure performance especially the nonlinear behavior. As described previously, spring elements are used to simulate the bond behavior between the rebar and the

concrete in the FE model. A bond slip model is adopted to describe the spring element properties. Thus, by examining the changes in the parameters in the bond-slip model, the bond behavior changes due to ASR deterioration can be studied.

3.3.1 Available Bond-Slip Models

Although the bond-slip behavior is quiet complex, researchers generally agree that the behavior consists of four stages. Figure 3-2 taken from CBE-FIP (2000) illustrates those four stages. During Stage I, concrete remain uncracked and mainly the chemical adhesion provides the bond. There is small rebar slip but localized stresses appear near the lug tips. In Stage II, the first cracking occurs and the bond due to chemical adhesion starts disappearing. Large bearing stresses forms at the lugs for the deformed bars and transverse microcracks occur at the tips of the lugs allowing the bar to slip. Based on the confinement level, the next stage can be Stage III, IVa, IVb, or IVc.

Stage III is in case of lighter transverse and confinement steel. In this case the bond ends as soon as the slitting cracks reach the outer surface of the member. Stage IVa is for plain bars. Stage IVb describes the bond behavior for bars with light but sufficient transverse reinforcement to assure a bond even after splitting of the concrete. In this case, even though the bond strength decreases after reaching a peak as slipping increases, the bond strength remains significant also at large slip values. Stage IVc shows the bond behavior of deformed bars with adequate transverse reinforcement, where even after the bond stress reaches its peak the bond stress remain large as slipping increases.

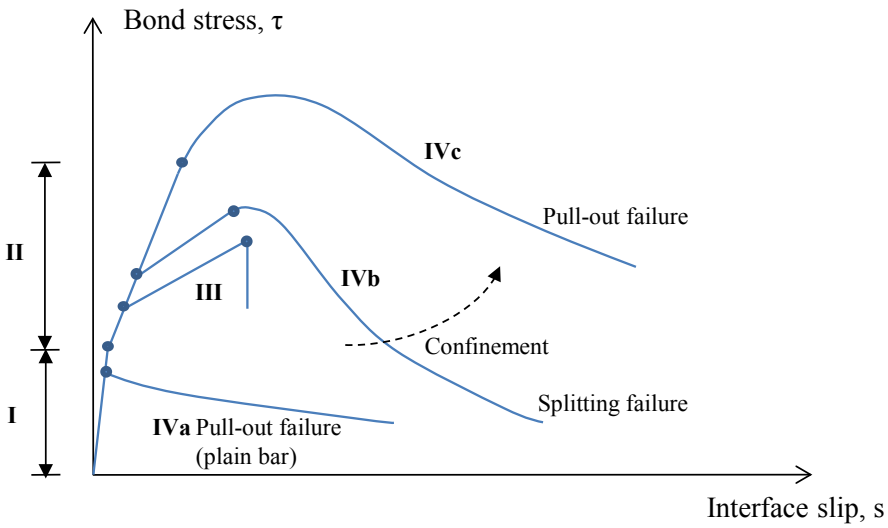

Figure 3-2. Illustration of Bond-Slip Behavior (CBE-FIP 2000).

Many researchers have proposed multi-segmental models to represent the bond-slip relation and calibrated the curves typically using pull-out experimental data (Nilson 1972, Guo and Shi 2003, and Tassios 1982). Figure 3-3 gives some typical bond-slip relations with three, five, and six segments.

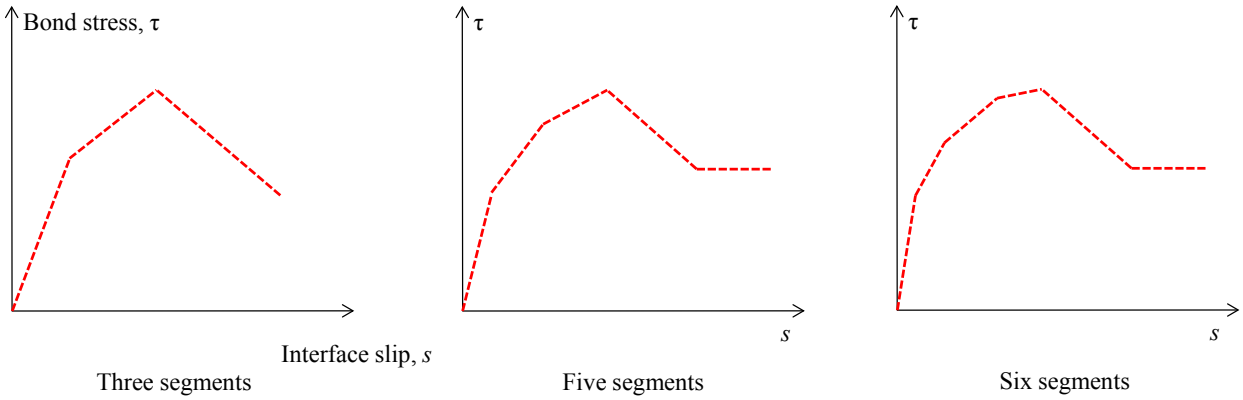

Figure 3-3. Simplified Bond-Slip Relations.

3.3.2 MC 90 Model

The MC90 bond model suggested by CEB-FIP (2000), is commonly adopted in research. This model divides the bond stress, τ, into four segments as a function of the interfacial slip, s, between the concrete and the reinforcement. Figure 3-4 describes the bond-slip behavior according to the MC90 model.

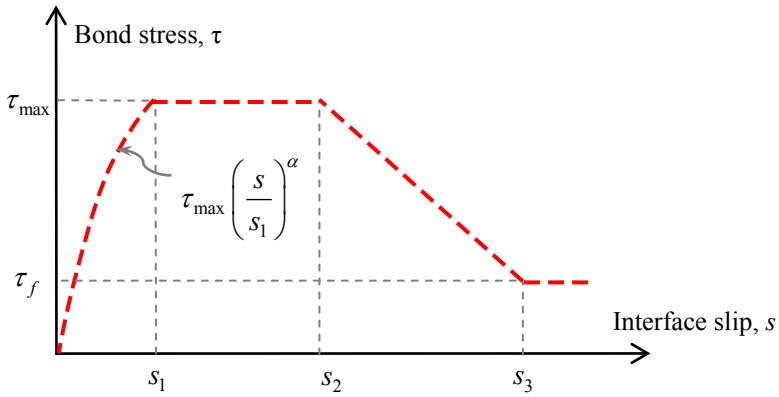

Figure 3-4. Bond-Slip Behavior in MC 90 Model.

The mathematic expression of the model is:

$$\tau = \begin{cases} \tau_{max}\left(\frac{s}{s_2}\right)^{\alpha} & s < s_1 \\ \tau_{max} & s_1 \le s < s_2 \\ \tau_{max} - \frac{\tau_{max} - \tau_f}{s_3 - s_2}(s - s_2) & s_2 \le s < s_3 \\ \tau_f & s_3 \le s \end{cases} \quad \text{(Eq. 3-3)}$$

where $\tau_{max} = \kappa\sqrt{f_{cm}}$ (MPa) = maximum bond stress or bond strength, in which κ = constant, $\tau_f = 0.4\tau_{max}$ = bond stress at failure, α, s_1, s_2, and s_3 = constants that define the shape of the bond-slip behavior. The values of α, κ, s_1, s_2, and s_3 depend on whether the concrete is unconfined or confined, and on the bond conditions. Table 3-1 gives the values of the parameter of the MC90 model based on confinement and bond conditions.

Table 3-1. Parameter Values for MC90 Model.

Parameters	Unconfined concrete		Confined concrete	
	Good bond conditions	All other bond conditions	Good bond conditions	All other bond conditions
s_1	0.6 mm (0.024 in.)	0.6 mm (0.024 in.)	1.0 mm (0.039 in.)	1.0 mm (0.039 in.)
s_2	0.6 mm (0.024 in.)	0.6 mm (0.024 in.)	3.0 mm (0.118 in.)	3.0 mm (0.118 in.)
s_3	1.0 mm (0.039 in.)	2.5 mm (0.098 in.)	Clear rib spacing	Clear rib spacing
α	0.4	0.4	0.4	0.4
κ	2.0	1.0	2.5	1.25
τ_f	0.15 τ_{max}	0.15 τ_{max}	0.4 τ_{max}	0.4 τ_{max}

Based on the MC 90 model, another bond model was proposed by Powanusorn and Bracci (2006), which was shown to give better predictions for the performance of RC members prone to shear deformations. The constitutive relationship for the bond stress-slip is as follows:

$$\tau = \begin{cases} \tau_{max}\left(\dfrac{s}{s_2}\right) & s < s_2 \\ \tau_{max} - \dfrac{\tau_{max} - \tau_f}{s_3 - s_2}\left(s - s_2\right) & s_2 \le s < s_3 \\ \tau_f & s_3 \le s \end{cases} \qquad \text{(Eq. 3-4)}$$

where $s_2 = 3$ mm, and $s_3 = 10.5$ mm. Eq. 3-4 is a special case of Eq. 3-3 where $s_1 = s_2$.

Even though the model proposed by Powanusorn and Bracci (2006) was developed for RC members prone to shear deformation like specimens tested as part of TxDOT Project 0-5722, the potential effect of ASR may change the bond behavior because, as shown in Table 3.1, the parameters a bond model depend on the confinement and bond conditions. Therefore to capture the effects of ASR, as part of TxDOT Project 0-6491, the model parameters $\mathbf{x} = \{k, \alpha, s_1, s_2, s_3\}$ in the MC 90 model are calibrated using the force-displacement results obtained from destructive testing.

3.3.3 Modeling the Bond-Slip Behavior in the FE Model

Abaqus provides various modules that can be potentially used to simulate the contact between concrete and rebars, such as constraints, contact elements, and connector elements.

Spring element as one of the connector elements is chosen in this study due to its simplicity. The spring element behavior is defined by force-displacement relation, which can be derived from the bond-slip relation and the node distance. The nonlinear behavior is defined by supplying pairs of force-relative displacement values. As the nodes of the concrete and the nodes of the reinforcement share the same geometric location, the displacement in the spring elements indicates the slip that occurs between the concrete and the rebar.

3.4 DETERMINATION OF BOND-SLIP MODEL PARAMETERS

A statistical analysis is used to determine the model parameters, $\mathbf{x}$, that provide the best fit between the results from the FE analyses and the test data. Four sets of model parameters are assessed one for each of the four stages of ASR: no damage (Specimens C1 and C2), early stage (Specimens C3 and C4), middle stage (Specimens C5 and C6), and later stage (Specimens C7 and C8). The differences of **x** values for these four sets reflect the different effects that different stages of ASR have on the bond behavior. Using the model formulation shown in Eq. 3-3, Table 3-2 lists the mean and standard deviation (St. Dev.) of the model parameters.

Table 3-2. Model Parameters in the Bond Model.

ASR stage	Specimen	α		s_1 (mm)		κ	
		Mean	St. Dev.	Mean	St. Dev.	Mean	St. Dev.
No damage	C1 & C2	2.65	0.14	1.35	0.08	0.75	0.12
Early stage	C3 & C4	1.10	0.14	0.81	0.12	0.96	0.13
Middle stage	C5 & C6	0.65	0.13	0.97	0.13	1.31	0.15
Later stage	C7 & C8	2.21	0.37	0.91	0.21	0.96	0.21

Note: For all four models $s_2 = \max[s_1, 3 \text{ mm } (0.12 \text{ in.})]$, and $s_3 = 10.5 \text{ mm } (0.41 \text{ in.})$.

Figure 3-5, Figure 3-6, Figure 3-7, and Figure 3-8 show the match between the force-displacement results obtained from the FE analyses using mean values of **x** and those obtained experimentally. The figures clearly show that the changes in the force displacement relation in deteriorated specimens can be explained by considering changes in the bond behavior due to ASR damage. In particular, the deteriorated columns have a larger post-cracking stiffness as

shown in Figure 2-7 and Figure 2-8. Increasing the initial slope of the bond-slip relation as a result of decreasing s_1 and α captures this phenomenon.

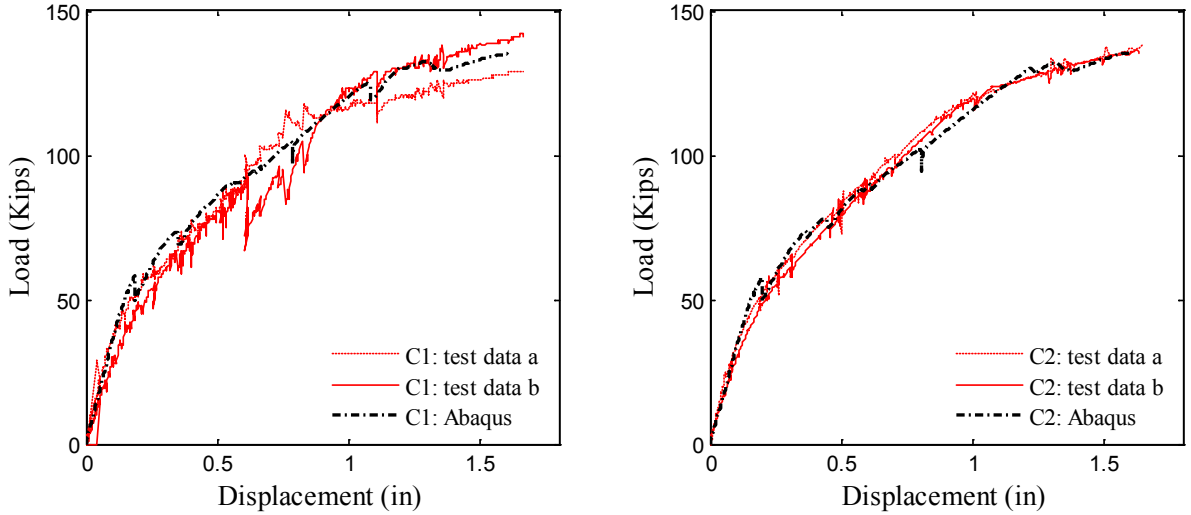

Figure 3-5. Comparison between Responses from FE Analyses and Testing for No ASR Damage (1 in. = 25 mm).

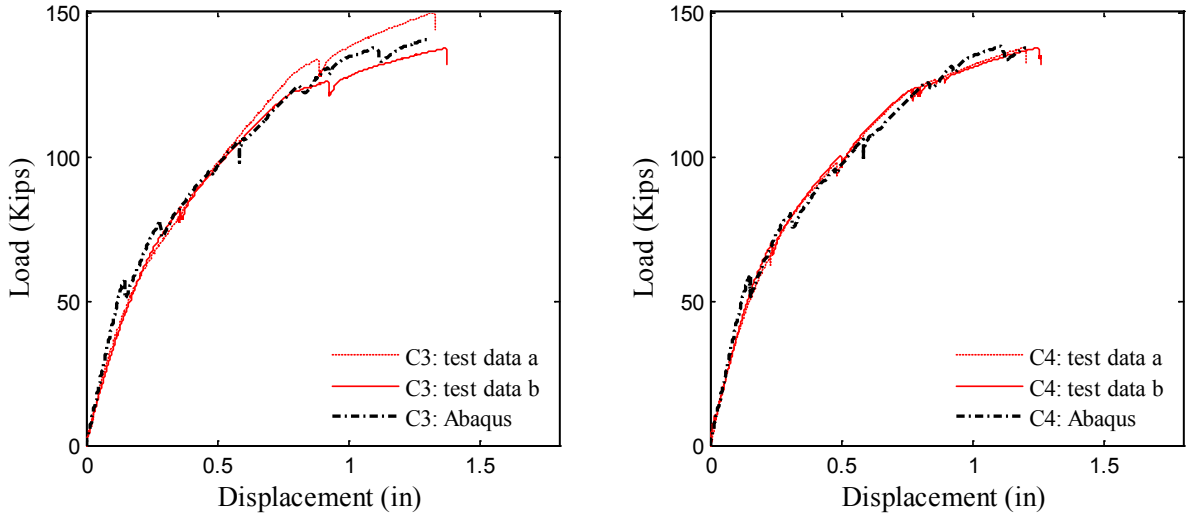

Figure 3-6. Comparison between Responses from FE Analyses and Testing for Early Stage ASR (1 in. = 25 mm).

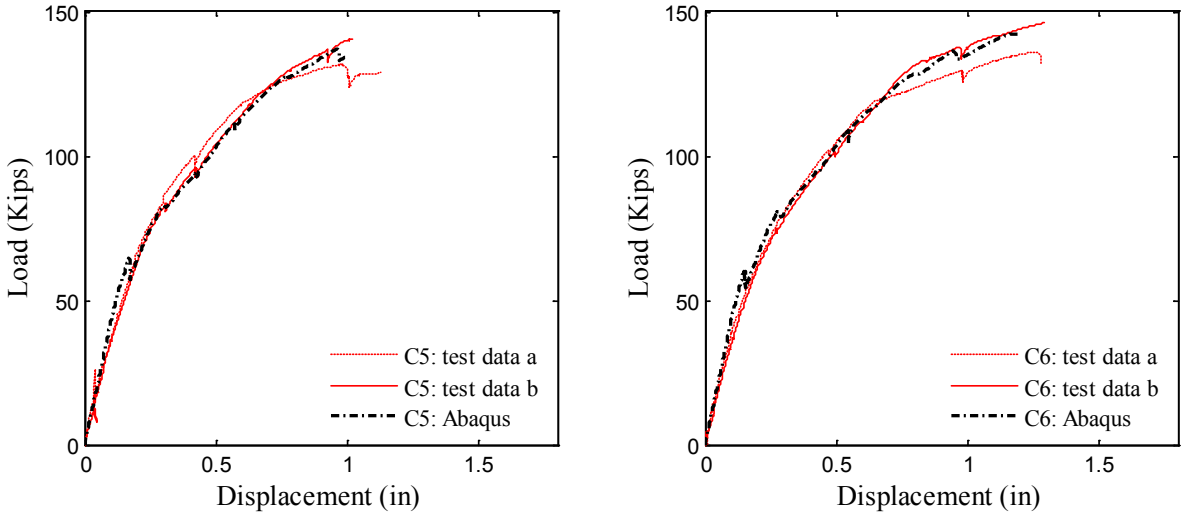

Figure 3-7. Comparison between Responses from FE Analyses and Testing for Middle Stage ASR (1 in. = 25 mm).

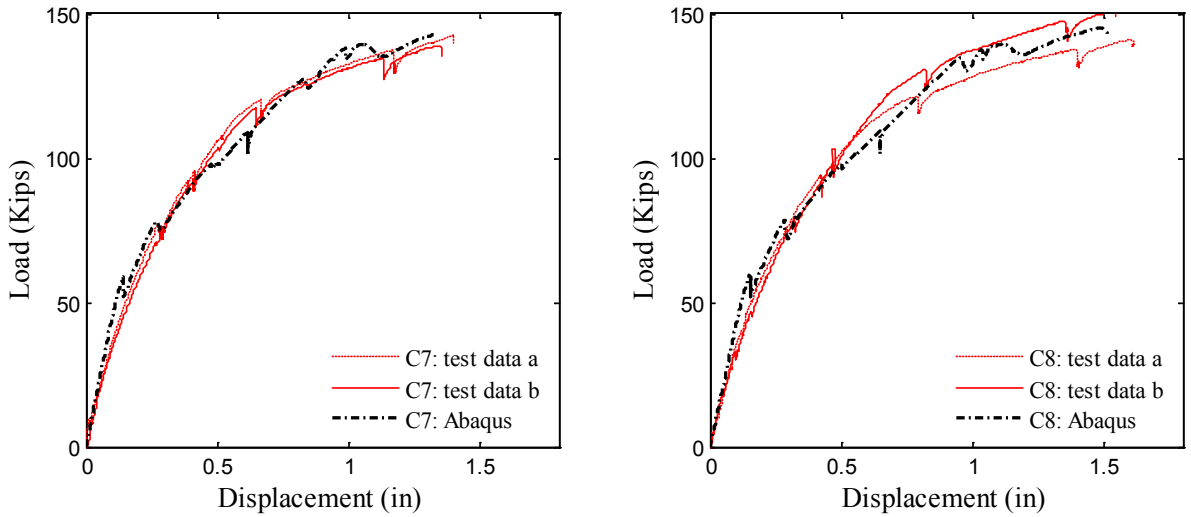

Figure 3-8. Comparison between Responses from FE Analyses and Testing for Later Stage ASR (1 in. = 25 mm).

Figure 3-9 illustrates the bond-slip relations obtained for the four ASR stages. The bond stiffness tends to increase for the specimens exhibiting more ASR deterioration while the bond strength (related to κ) drops for the later-stage columns. Physically, the formation of ASR gel results in additional confining force on the steel. However, as ASR deterioration reaches a certain level the additional confinement decreases due to the excessive cracking of the concrete.

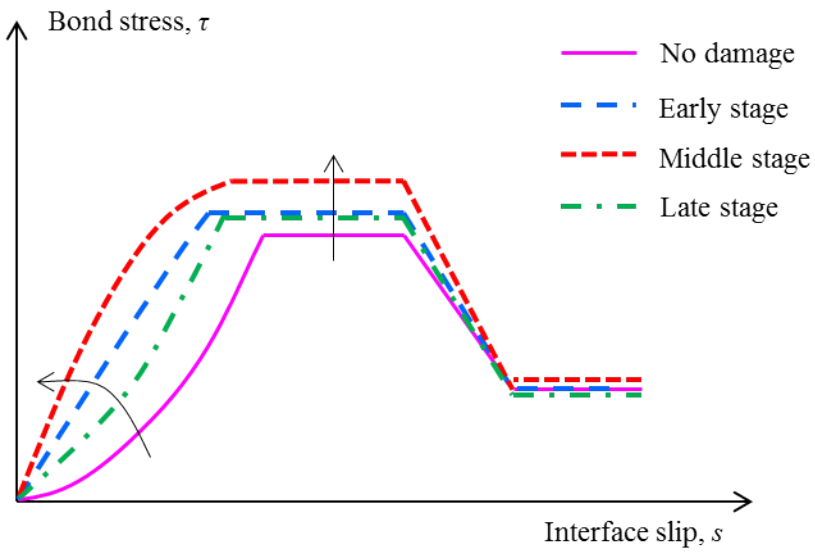

Figure 3-9. Bond-Slip Behaviors for Different Stages of ASR.

3.5 SUMMARY

As part of observation from TxDOT Project 0-5722, it is found that the post-cracking stiffness increases for specimens exhibiting later-stage ASR deterioration. Three factors were identified to possibly explain the different behavior between the control columns and deteriorated columns reported by TxDOT Project 0-5722: increase compressive strength, additional confining, and change in bond behavior. This chapter investigates these three factors by developing a FE model that matched the experimental results.

The compressive strength increases for the older, more deteriorated specimens due to the continued hydration of cement. The actual compressive strength was determined from standard cylinder testing. However, incorporating the increase in the compressive strength into the FE model is not sufficient to explain the stiffness increase found in the experimental results.

Additional confining force and axial compressive load are generated as a result of the ASR expansion. However, a sensitivity analysis shows that the core concrete strength, which is influenced by the additional confining force, does not significantly contribute to the flexural stiffness. Also, the additional axial load was calculated using measurement of the tensile strains in the strands obtained from electronic strain sensors, and incorporating the additional axial load into the FE model is still not enough to reflect the stiffness increase shown in the experimental results.

A change in bond behavior between the steel and concrete occurs due to ASR deterioration. The FE model is used to assess the parameters of the bond-slip model under different levels of ASR deterioration while incorporating the changes in the concrete compressive strength and the additional axial load. In particular, four models have been developed and each model corresponds to one of four different levels of ASR deterioration in RC columns. The models were calibrated using force-displacement data obtained from four-point load testing of eight large-scale bridge columns subject to different levels of ASR deterioration. Additional specimens with higher level of ASR deterioration are available and will be tested in the future to better understand the bond behavior of ASR-damaged columns. The results show that the changes in the force displacement relation in deteriorated specimens can be explained by considering changes in the bond behavior due to ASR damage. Specifically, it is found that:

1. The bond stiffness initially increases with increasing levels of ASR damage. Likely, the bond behavior improves due to the expansion-induced confinement caused by ASR.
2. However, once ASR deterioration reaches a certain level, the bond strength decreases due to the excessive ASR cracking.

The remaining question is then "what is the bond deterioration for a structure in the field?" If the bond deterioration resulting from ASR is the same or less then for the large scale samples then likely there is not significant change in the structural performance. NDE technologies can help answer this question. The next chapter describes four different NDE technologies considered to assess the steel-concrete bond in ASR affected structures.

4 SELECTION OF NDE TECHNIQUES

4.1 INTRODUCTION

In order to efficiently select a NDE method for assessing bond in ASR/DEF affected structures, it is important to begin by pointing out that all methods for NDE of RC structures face the same set of inherent challenges given by the materials under examination. Concrete is a complex aggregation of several fundamentally different ingredients. The heterogeneous nature of concrete sometimes leads to the unfavorable attenuation of propagating waves that are monitored by many NDE techniques. Additionally, the construction practices involved in constructing RC structures can lead to a variation in material properties and the placement of reinforcement within the same member. These challenges are further complicated by RC deterioration mechanisms that lead to complex defects and cracking patterns that are, at least to some extent, random. For any NDE method to be considered effective, it must sufficiently account for all of these factors in the evaluation process.

4.2 REVIEW AND SELECTION OF POTENTIAL NDE METHODS

The examination and selection of techniques with potential to assess the steel-concrete interface in ASR/DEF affected structures begins with defect and crack assessment techniques that have been used in RC applications. In this sense, only techniques that have progressed in their development given the inherent challenges of concrete are considered. Three types of NDE are considered for this application. All of these techniques rely on the propagation and sensing of mechanical stress waves within a concrete member, though they all do so using distinctly different methods for generating, recording, and analyzing the local response. Concrete imaging techniques, ultrasonic guided wave monitoring, and the impact-echo method have all been considered as possible methods for assessing the steel-concrete interface, and a review of these methods follows.

4.2.1 Concrete Imaging

Imaging techniques are those which reconstruct the measurements physical quantities to create 2- and 3-D images of the internal portions of the member under examination. One of the most prevalent uses of imaging technologies occurs in the field of medicine, where human tissue

is included in the set of fluid rich media that can be accurately evaluated using modern ultrasonic imaging techniques.

Using state-of-the art equipment, a set of small-scale cementitious samples was examined to determine whether this technique was suitable for assessing the steel-concrete interface. The results of this study showed that the high excitation frequencies are not effective in cementitious media, resulting in poor resolution images that offer no information about the state of the steel-concrete interface. This conclusion holds when the cover depth of reinforcing steel is reduced to as low as 0.4 in. (10 mm), a dimension that is well below codified requirements for cover depth in RC structures.

X-ray tomography, another technique common to medical practice, was also used to examine the same set of small-scale samples. Though this study yielded good results, the technique requires that small-scale samples be sent to a laboratory setting due to the large size of testing equipment. This technique is classified as unsuitable due to the inability to directly examine structures in the field.

The most promising technique for imaging concrete structures is the shear-wave tomography technique. State-of-the-art systems that employ this technique use a pitch-catch configuration array of transmitting and receiving transducers to both excite and record stress-wave reflections as shown in Figure 4-1. The synthetic aperture focusing technique (SAFT) is used to create two- and three-dimensional images of the interior of the structure. Application of this technique to assessing the steel-concrete interface has not been reported, and commercially available systems using this technique advertise a minimum testing depth of approximately 2 in. (MIRA 2012). Because this threshold exists within the range of codified cover-depth thresholds, this technique was not pursued during the course of this project, i.e., not all cover depths can be assessed with this method.

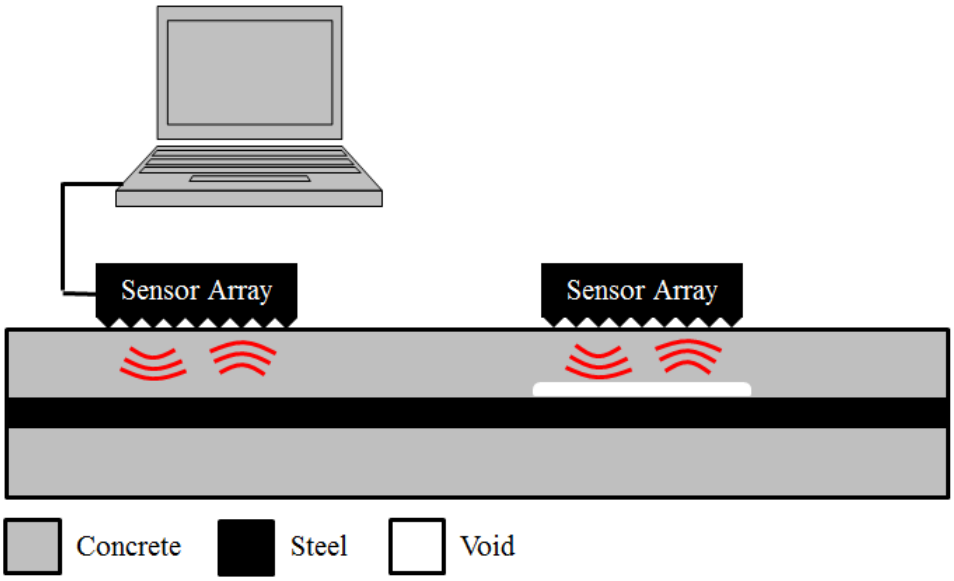

Figure 4-1. Schematic of Shear-Wave Tomography Technique.

4.2.2 Ultrasonic Guided Wave Monitoring

Ultrasonic guided wave monitoring is a set of techniques in which excitation is applied to an exposed reinforcing bar creating stress waves that propagate primarily along the longitudinal axis of the reinforcement. Several different approaches to measuring the response have been researched, including measurements at the opposite end of the reinforcing bar and on the concrete surrounding the bar under examination (Na et al. 2002) as shown in Figure 4-2. Regardless of where the response is measured, the goal of these techniques is to assess bond state along the length of a reinforcing bar by performing a single test.

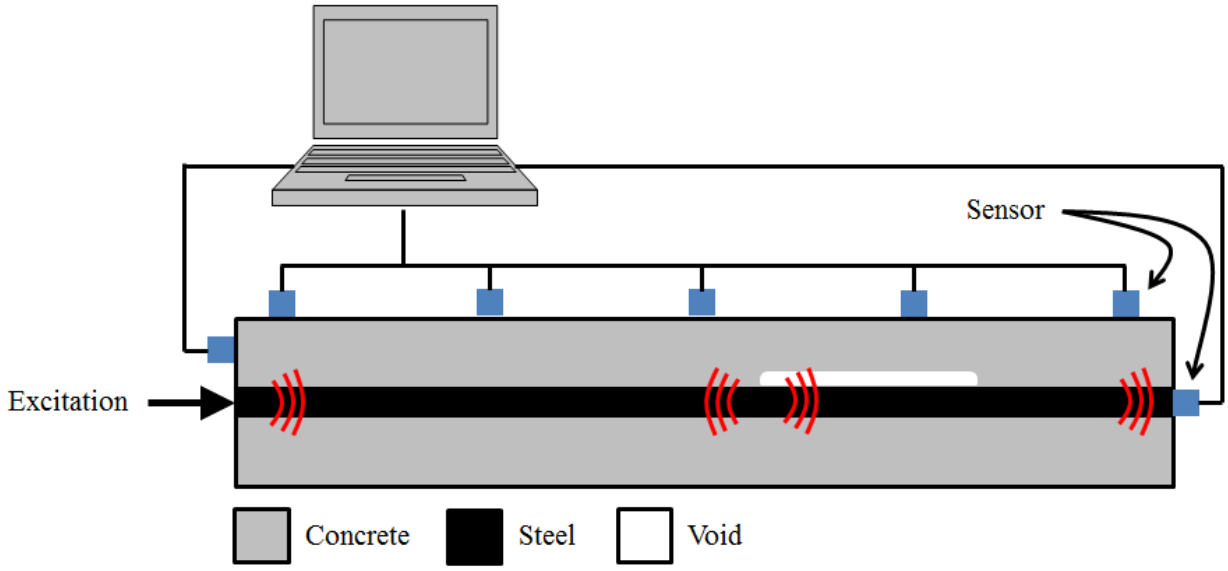

Figure 4-2. Schematic of Ultrasonic Guided Wave Monitoring with Different Sensing Configurations.

Multiple testing configurations that may be classified as ultrasonic guided wave monitoring were explored in connection with this project. When applied to detect debonding in a set of small-scale samples with voids deliberately cast at the steel-concrete interface and reinforcement bar ends exposed, these techniques yielded promising results (Han et al. 2012). These results are not included in this report, as no plan for transitioning these concepts to the testing of field structures has yet been developed. This lack of field applicability results from the key disadvantage of these techniques, in that they require at least one end of steel reinforcement to be exposed. As a consequence of corrosion protection, this situation does not typically occur in RC structures, and deliberately exposing rebar to perform the test could create structural problems relating to reinforcement discontinuity, effectively negating the nondestructive nature of the test. In their current state of development, these techniques are not examined in this project.

4.2.3 Impact-Echo

The impact-echo method is a technique for assessing RC structures that uses the properties of impact-generated stress waves to detect flaws and characterize geometry. It has been used successfully in a wide variety of applications, including the detection of voids at the interface between concrete and reinforcing steel. A controlled short-duration impact results in

the propagation and subsequent reflection of stress waves within a concrete member. As these waves reflect from internal interfaces, they cause periodic out of plane surface displacements that are recorded by a displacement sensor as shown in Figure 4-3, and analyzed using digital signal processing techniques (Sansalone and Streett 1997). Impact-echo testing can be performed at equidistant intervals along the surface of a RC member, and the results can be analyzed in different domains to make determinations about the presence of voids and geometry of the member (Algernon and Wiggenhauser 2006).

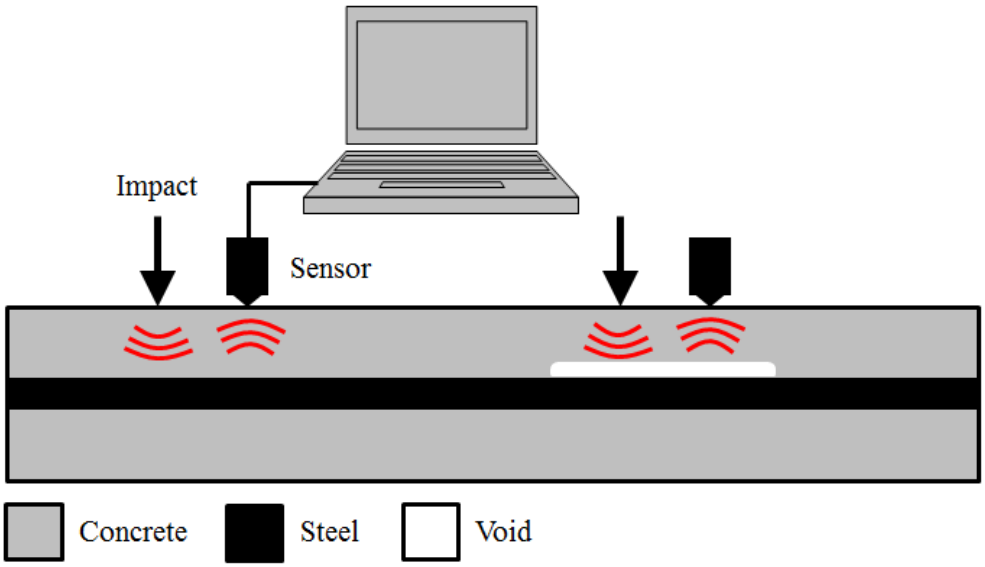

Figure 4-3. Schematic of Impact-Echo Method.

Impact-echo has been used to examine structures with suspected steel-concrete bond damage resulting from early-age vibration of the structure. In 1999, the 921 Chi-Chi Earthquake damaged thousands of structures in Taiwan. In recently constructed RC structures, the ground motion of the earthquake caused steel reinforcement to vibrate, creating circular voids in the fresh concrete surrounding the bar. Impact-echo was employed to detect these voids, and small-scale experimentation was used to connect the results of impact-echo testing to loss of bond strength between reinforcing steel and concrete (Hsu et al. 2008).

Due to its use in a similar application, in addition to being well-studied, readily available, and relatively inexpensive, impact-echo is chosen as the potential candidate for detecting possible damage at the steel-concrete interface in ASR/DEF affected structures. The remainder of this chapter presents a review of available literature on the impact-echo method, and

subsequent chapters present the results of experimental programs that are designed to assess the effectiveness of the method in detecting ASR/DEF.

4.3 IMPACT-ECHO LITERATURE REVIEW

This discussion of impact-echo will center on reviews of each of the key components that comprise the method. A review of the physical phenomenon introduces the basic ideas of stress wave propagation in solid media. This phenomenon is complex, and therefore simplifying assumptions can be made, leading to the fundamental equations of the impact-echo method. Once an understanding of the underlying phenomenon is reached, a review of the data collection techniques is presented to establish the set of limitations under which the stress wave reflections can be recorded. These limitations result from the current state of sensing technologies and the nature of digital data collection, or sampling. The recorded waveform can then be analyzed using a variety of representations and additional digital signal processing (DSP) techniques. The goal of additional DSP is to offset some of the disadvantageous characteristics of stress wave propagation and digital data collection that may make flaw detection difficult. While individual tests can reveal important information, adapting impact-echo into a scanning technique gives a broader perspective on the state of the structure under investigation. When this process is complete, the results can be used to make determinations about the state of the interface between steel reinforcement and concrete in RC structures.

4.3.1 Physical Phenomenon

The physical phenomenon that is fundamental to the impact-echo method consists of both the impact and response of a concrete member. The response, which is measured, processed, and interpreted in the impact-echo method, is dependent on the characteristics of the impact and the material properties and geometry of the member under examination. The characteristics of the impact are important because they are the portion of the response input that is controlled by the investigator. The impact can be generated using a variety of methods, depending on the assembly of the system used to perform the test. The goal of the impact is to apply a forcing function that can be modeled as a point force on the testing surface with a time history proportional to a half-cycle sine curve with force amplitude A and period $2t_d$, where t_d is the impact duration, as shown in Figure 4-4.

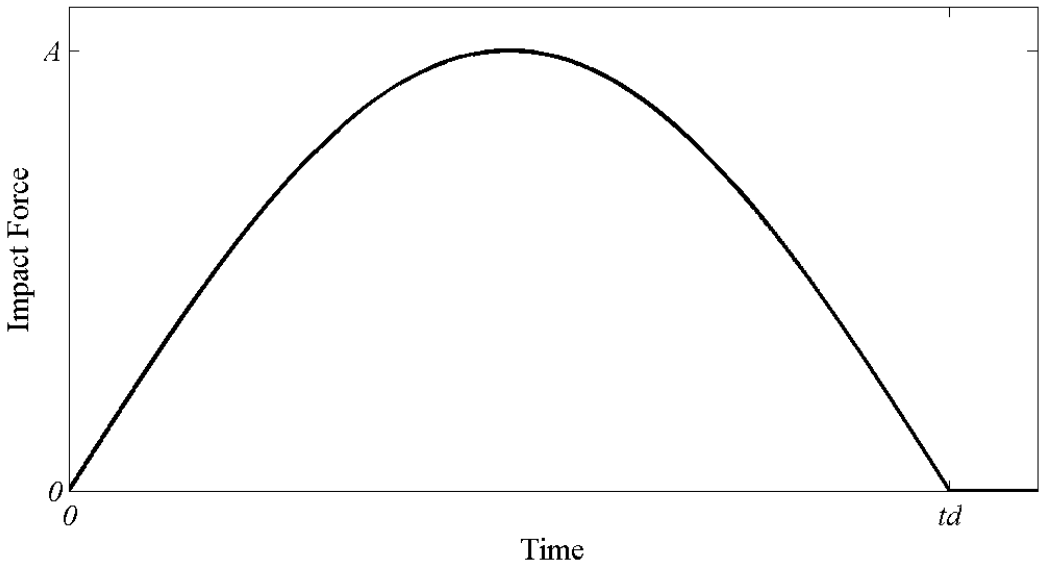

Figure 4-4. Impact Forcing Function (Reproduced from Sansalone and Streett 1997).

The parameter t_d is critical to ensuring stress wave reflection from shallow interfaces, that, due to their shorter periods (and higher frequencies) of reflection, require higher frequency excitations to be observed. The maximum usable frequency f_{max} is determined using (Sansalone and Streett 1997):

$$f_{max} = \frac{1.25}{t_d} \qquad \text{(Eq. 4-1)}$$

In most commercial systems, impact is achieved using either an impactor consisting of a steel ball attached to a spring rod or a spring loaded impactor encased in the same housing as the displacement sensor. In either case, adjusting t_d may be achieved through system specific procedures to control the range of usable frequencies in the response. In the digital signal processing that follows the recording of the response, the shape of the impact forcing function is used to normalize the response so that multiple tests can be properly averaged and compared.

The response of concrete to a point impact consists of three wave types that are distinguished by the speed of wave propagation and the direction of particle motion on the wavefront. This particle motion is sufficiently small to treat concrete as an elastic material. Primary waves (P-waves) travel on a spherical wavefront within an elastic body and are distinguished by particle motion perpendicular to the direction of propagation. This motion causes either compressive or tensile stresses on the wavefront. Secondary waves or shear waves (S-waves) also travel on a spherical wavefront, but with motion parallel to the direction of wavefront propagation.

Rayleigh waves (R-waves) are surface waves that travel on a circular wavefront emanating from the impact location and are characterized by relatively large out-of-plane displacements on the wavefront. The shape of the R-wave can be used to approximate the shape of the forcing function in Figure 4-4, and subsequently t_d and A (Cheng and Yu 2000). The P-wave speed, C_p, in an elastic medium is determined as a function of elastic modulus, E, Poisson's ratio, v, and material density, ρ, using (Krautkrämer and Krautkrämer 1990):

$$C_p = \sqrt{\frac{E(1-v)}{\rho(1+v)(1-2v)}} \quad \text{(Eq. 4-2)}$$

The S-wave speed, C_s, and the R-wave Speed, C_r, are also functions of E, v, and ρ. The relative speeds of the three wave types are only a function of v, with C_p and C_r always the fastest and slowest, respectively.

These wave types reflect from internal interfaces and external boundaries of the impacted member. The amplitude of the S-wave relative to the P-wave is minimized beneath the impact, such that, if the distance between the impact and the measurement location is minimized, the contributions of reflecting S-waves can be neglected in the interpretation process. The characteristics of the P-wave reflection are important because they affect the period of reflection as detected by the displacement sensor, and subsequently, the frequency of wave reflection which is used to interpret the impact-echo results. These characteristics are determined by the material properties of the two materials that define the interface. Specifically, the material property of interest in this situation is the acoustic impedance Z. When a stress wave traveling through a material with specific acoustic impedance Z_1 arrives at the interface with a second material with acoustic impedance Z_2, the reflection coefficient R_N for normal incidence is given by (Krautkrämer and Krautkrämer 1990):

$$R_N = \frac{Z_2 - Z_1}{Z_2 + Z_1} \quad \text{(Eq. 4-3)}$$

When Z_2 is greater than Z_1, R is positive, meaning that the stresses at the wavefront of the reflecting wave have the same sign as the incident wave. In this case, an incident P-wave with tensile stress at the wavefront, known as a tension wave, will reflect from the interface of materials 1 and 2 as a tension wave. Conversely, an incident P-wave wave with compressive stress at the wavefront, known as a compression wave, will reflect from the interface as a compression wave. When Z_2 is less than Z_1, R is negative, meaning that the stresses at the

wavefront of the reflecting wave have the opposite sign of the incident wave. In this case, an incident tension wave reflects as a compression wave, and vice versa (Carino 2001).

The importance of the sign of R can be seen by a closer examination of the two cases in which Z_2 is less than Z_1 and Z_2 is greater than Z_1. For case 1 ($Z_2 < Z_1$), impact imparts a compression wave into the concrete body. Figure 4-5a depicts the path of the incident wave as it travels through a distance D from the point of impact to the interface of the two materials. Upon reaching the interface, a portion of the wave is reflected within material 1 and returns to the impacted surface as a tension wave. This return of the wave to the impacted surface causes is denoted the 2P return, as the P-wave has now traveled a distance $2D$. In general, the return of a tension wave causes a local out of plane contraction of the material that can be measured using a displacement sensor. As the air at the interface of the concrete and the impacted surface has acoustic impedance much less than that of concrete, the wave reflects as a tension wave. The pattern repeats itself, creating the 4P, 6P… reflections until the wave is completely attenuated. The frequency of the reflection can then be determined as the speed of the P-wave divided by the distance traveled in one reflection period (Sansalone and Streett 1997):

$$f = \frac{C_p}{2D} \qquad \text{(Eq. 4-4)}$$

This simple relation is of importance to the impact-echo method. Impact-echo can be used to determine the reflection frequency of stress waves by measuring the displacements associated with the repeated return of tension waves. As shown in Eq. 4-4, this can then be used to determine the depth of an air filled void D_v, assuming that C_p is known (Sansalone and Streett 1997).

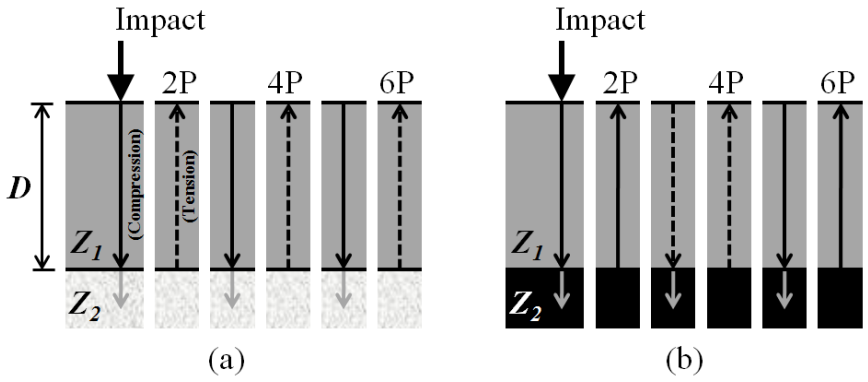

Figure 4-5. Normal Reflection of Impact-Generated Incident P-Wave when (a) $Z_2 < Z_1$ and (b) $Z_2 > Z_1$.

For case 2 (Z2 > Z1), the incident compression wave does not undergo a phase change at the interface of materials 1 and 2 and reflects back toward the impacted surface as a compression wave, as depicted in Figure 4-5a. As the wave reaches the interface with the impacted surface, the acoustic impedance change causes a phase change and a tension wave returns toward the interface of materials 1 and 2. As with the incident impact generated compression wave, this tension wave does not undergo a phase shift and returns to the impacted surface as a tension wave. This means that the tension wave returns to the surface at 4P after traveling a total distance 4*D* during the period of reflection. For case 2, the return frequency of the tension wave is given by (Sansalone and Streett 1997):

$$f = \frac{C_p}{4D} \qquad \text{(Eq. 4-5)}$$

The interface described in case 2 is typical of the interface between concrete and reinforcing steel, as the acoustic impedance of steel is much greater than that of concrete (Sansalone and Steett 1997). From Eq. 4-4 and Eq. 4-5, it can be seen that there is a fundamental difference in the frequency of return of stress waves from bonded and debonded steel in a RC structure. This is the concept that makes impact-echo a favorable technique for detecting loss of bond in ASR/DEF structures.

The propagation of stress waves within concrete is of a transient nature, meaning that the amplitude of the response is lessened with time due to divergence and attenuation. Divergence is the spreading of the wavefront that increases with the distance traveled by a particular stress wave. Attenuation is the result of absorption and scattering of stress waves at defects within a concrete member (Sansalone and Streett 1997). The overall effect of divergence and attenuation is a weakening of the amplitude at each return of the P-wave to the impacted surface, indicating that there is a limited range of time within the signal in which the P-wave reflections are of sufficient amplitude to yield information about the location under examination.

4.3.2 Observing Stress Wave Propagation

Before interpreting the results of stress wave propagation, it is important to understand how the ability to observe stress wave propagation in concrete is limited or enhanced by the capabilities of current technologies. As is the case with all physical phenomena, the ability to record the impact response is limited by the resolving power of the instrument used to make the measurement and the necessarily discrete nature of the recorded data. When observing the stress

wave propagation as a displacement record with respect to time, the geometric complexities of the specimen under investigation often give rise to multiple reflection components that make signals of this form difficult to interpret. The Fourier representation of time-displacement signals as amplitude-frequency signals is introduced to enhance accuracy with which complex responses may be interpreted. Upon observing impact-echo phenomena in this manner, it can be seen that some of the models for describing stress wave propagation in concrete are overly simplistic, and to avoid the necessity for more complex mechanical models, correction factors are introduced to existing descriptions.

The use of a wide variety of displacement sensors has been reported for impact-echo testing. The most common displacement sensor attached to commercial packages is a piezoelectric displacement transducer, though accelerometers (Popovics 1997) and microphones (Zhu and Popovics 2007) have been shown to produce good results. For any selection, it is important to understand that, due to its dynamic properties, the response of the specific sensor may vary at different frequencies. However, the response of a sensor typically contains a range of frequencies over which the response is flat, meaning that, within this range, the relative amplitudes of stimuli with varying frequency are approximately preserved (Shieh et al. 2001). The range of frequencies that should be consistently measured by the sensor in impact-echo testing is typically 1 kHz to 30 kHz (Popovics 1997), with the upper limit being as high as 80 kHz (Sansalone and Streett 1997). In the specific application of impact-echo to detecting voids around reinforcing bars, frequencies of interest typically do not exceed values near 50 kHz (Cheng and Sansalone 1993), giving a practical upper limit for the frequency range of the sensor. Once the selection is made, the sensor is placed a distance r from the location of the impact. This distance should be no further than the distance r_{max}, which is a function of the depth, D_{min}, to the interface nearest the impacted surface. The value of r_{max} is given by (Sansalone and Streett 1997):

$$r < r_{max} = 0.4D_{min} \quad \text{(Eq. 4-6)}$$

This restriction is imposed to minimize the contribution of S-wave reflections to the response record, ensuring that the contribution from the P-wave reflections is maximized (Sansalone and Streett 1997). Depending on the configuration of the impact-echo system, r is either a set parameter or a testing variable that can only be approximately determined. After impact, the sensor converts the out-of-plane surface displacements to voltages. Because this is done

proportionally, the time-voltage signal is commonly and henceforth referred to as the time-displacement signal. For the purpose of performing advanced processing and saving test records, the analog time-displacement signal is digitized by an analog-to-digital (A/D) data acquisition system (Sansalone and Streett 1997). This conversion of the signal from continuous to discrete involves both sampling and quantizing the signal. Sampling refers to the measurement of a continuous signal at an equal sampling interval, Δt, in the time domain. A finite number, N, of samples are measured. Just as a continuous signal is represented by discrete-time values, it must also be represented by discrete-voltage values. Quantization is the process by which continuous values are rounded to the nearest value that can be represented by the A/D system. Linear quantization is achieved when the representable values, or quantization levels, are evenly spaced by the minimum voltage resolution, ΔV. A/D systems only provide a finite number of quantization levels, N_Q (Owen 2007).

Prior to performing impact-echo testing, appropriate values should be chosen for the parameters t_d, r, Δt, N, and ΔV. After approximating the frequency content of interest in order to select a sensor, Eq. 4-1 and Eq. 4-6 can be used to determine appropriate values for t_d and r, respectively. A good value for Δt ensures that a sufficient number of samples is taken during reflection period associated with the highest frequency of interest, f_{high}, such that the sampling procedure accurately captures P-waves reflecting at f_{high}. Experience shows that this relation is given by (Sansalone and Streett 1997):

$$\Delta t < \frac{1}{10 f_{high}} \qquad \text{(Eq. 4-7)}$$

Selection of N is subject to constraints that ensure efficiency in the processing of signals. Specifically, N should be a power of two, and though it may be as large as the data storage system will allow, a maximum value of 2048 is typically large enough to capture a sufficient portion of the response. The quantization parameter ΔV should be selected as small as possible such that the product of ΔV and N_Q is greater than the maximum voltage output from the sensor (Sansalone and Streett 1997). The maximum voltage is a complex function of the material properties, specimen geometry, impact characteristics, and sensor sensitivity. There is no available function to predict the maximum voltage, so selecting ΔV is often a process of trial and error.

Figure 4-6 shows a typical impact-echo signal that was captured using a Δt of 1 μs, N of 2048, ΔV of 0.01 V, and an r of approximately 1 in. (25 mm). The first important characteristic

of the impact-echo signal is the large displacement occurring at between approximately 150 μs and 200 μs. This displacement is attributed to the propagation of the R-wave past the displacement sensor. Following the R-wave is a myriad of displacements caused by multiple wave types reflecting from multiple interfaces and external boundaries. The decay in the strength to the signal in this interval is the result of divergence and attenuation of the stress waves, meaning that the signal-to-noise ratio in this interval decreases with time. In simple cases where the boundaries of the member are far from the impact point and only one reflecting interface is present in the member (i.e., slabs with large lateral dimensions), time-domain signals may be interpreted to make determinations about the depth of the member. Time-domain interpretation is also used in the detection of voided sections of grouted post-tensioning ducts (Schubert 2006). In general, however, this approach to the interpretation of impact-echo data is ineffective due to the multiple reflection frequencies that result from complex geometries and cracking patterns. For this reason, a mathematical tool is needed to convert the time-displacement signal into an equivalent frequency-amplitude signal.

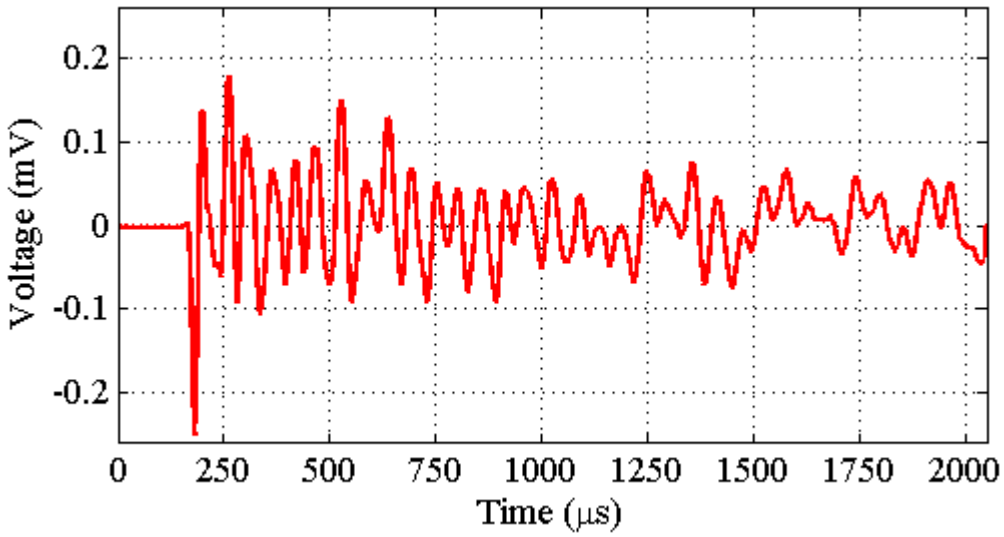

Figure 4-6. Typical Impact-Echo Signal.

The Fast Fourier Transform (FFT) is the preferred tool for revealing the frequency content of the time-displacement signal. In short, the FFT is a mathematical tool that is used to represent a signal as the sum of sine waves with varying frequencies and amplitude. The FFT can be implemented in all pre-assembled commercial systems and post-processing programs. The details of its implementation are omitted here. Figure 4-7 shows the magnitude of the FFT

for the typical impact-echo signal shown in Figure 4-6 and demonstrates how the signal can be represented in the frequency domain. The resolution Δf in the frequency domain is a function of the sampling parameters N and Δt given by (Sansalone and Streett 1997):

$$\Delta f = \frac{1}{N\Delta t} \quad \text{(Eq. 4-8)}$$

The largest amplitude value of 0.0376 mV occurs at 18.1 kHz, making this dominant frequency in the signal. Barring irregularities such as external harmonic noise, large shallow delaminations, or large sample depth, the frequency corresponding to the largest amplitude value is attributed to wave reflections from the external boundary at the full depth of the member. Recall that divergence and attenuation cause the signal to decay with time, and therefore the amplitude of reflecting waves shown by the FFT at any frequency is only an average over the duration of the signal.

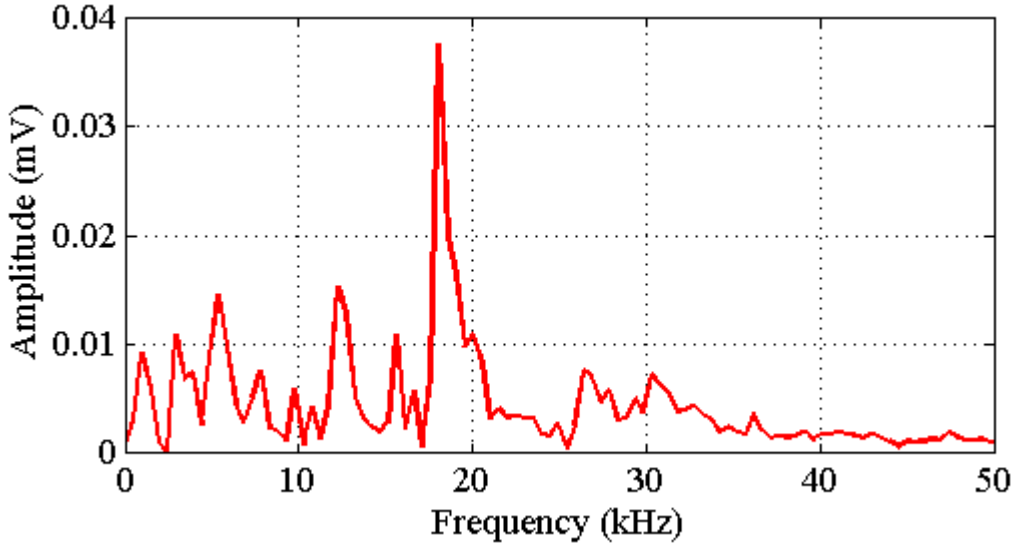

Figure 4-7. FFT of Typical Impact-Echo Signal.

Attention is now directed to the remainder of the relative maxima in the frequency spectrum. These peaks represent the frequency content of P-, S-, and R-wave reflections from internal interfaces and external boundaries, in addition to random noise. The concerning effect of S- and R-wave reflections from external boundaries, termed geometry effects, is that they interfere with the identification of P-wave reflections from interfaces other than the external boundary at the full member depth, effectively creating noise in the frequency spectrum (Schubert 2006). There are two approaches to overcoming this source of noise and increasing the accuracy with which the P-wave reflections can be identified. The first is to perform

multiple impact-echo tests at equal intervals along the length of sample, a procedure known as impact-echo scanning (Olson et al. 2011). The second is to apply additional digital signal processing (DSP) and filtering to the impact-echo signal in post-processing.

4.3.3 Impact-Echo Scanning

Impact-echo scanning has been used successfully in a variety of RC inspection applications. The process can be made more efficient through the use of commercial impact-echo scanners that allow for rapid testing of large areas, but traditional single-point configurations can be used to produce the same results, often with more flexibility over testing parameters. Correctly comparing results from adjacent impact-echo tests requires correction for variation in the force and duration of impact from one test to another. The impactors used in some commercial systems produce inconsistent impact characteristics from one test to the next. Spring-loaded impactors may produce impacts with more consistent characteristics. In either case, measuring amplitude using voltage does not provide any useful meaning of this quantity. Normalizing the amplitude values in the frequency spectrum both corrects for impact variation and provides physical meaning to the amplitude values. Additionally, normalization of amplitudes allows for impact-corrected statistical comparison of tests performed at the same location.

Normalization can be carried out using one of two methods. The simplest method for performing the normalization is known as the maximum value normalization (MVN, Malhotra and Carino 2004), in which the normalized frequency signal, $F_N(\eta)$, is calculated using the maximum amplitude value of the original frequency signal, $F(\eta)$ according to:

$$F_N(\eta) = \frac{F(\eta)}{max\left[F(\eta), \eta = 0, 1, \ldots, \frac{N}{2} - 1\right]} \quad \text{(Eq. 4-9)}$$

where η is the frequency index. The amplitude values are then presented proportionally with respect to the amplitude of the dominant frequency. Figure 4-8 shows the FFT of the typical impact-echo signal shown in Figure 4-7 after the application of MVN. In this manner, the amplitude of the dominant frequency is equal to 1 for all tests, allowing for comparison of collocated and adjacently performed tests. To gain a better perspective on the effect of using this technique, a comparison of the frequency signals from collocated impact-echo tests is made. Figure 4-9 shows the frequency signals of 10 collocated impact-echo tests without any attempt to normalize the signals. Though these signals are roughly equal in relative profile, it is clear that

there is some variance in the amplitude values. This is due to the variation in the impact force. Figure 4-10 shows these same signals after application of MVN. In this case, the normalization to the frequency signals reduces the variance in amplitudes at frequencies lower than approximately 26 kHz. Above this value, the relative variance in the amplitude values is reduced from the original signal, but to a lesser extent than in the lower frequency range. This technique is sufficient if the only frequency of interest is the dominant frequency.

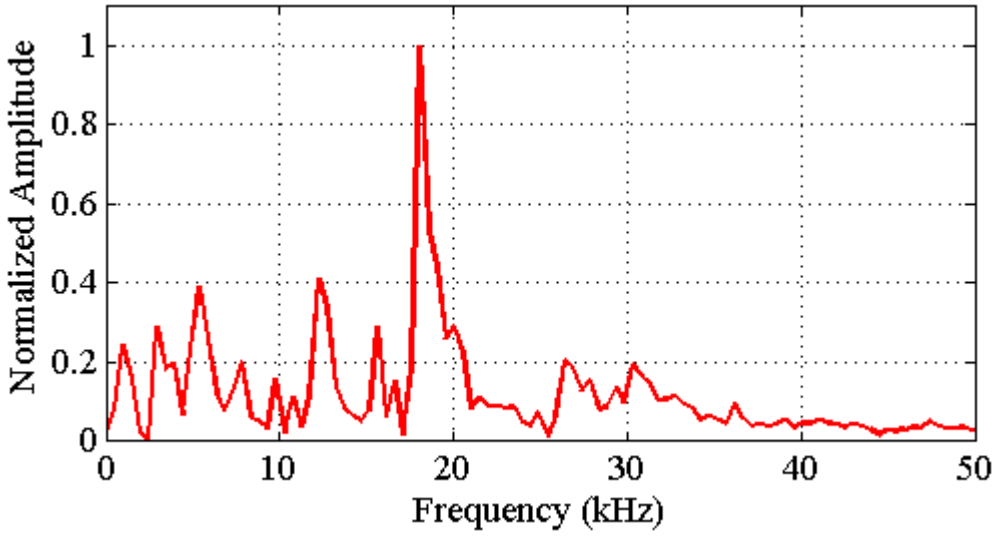

Figure 4-8. FFT of Typical Impact-Echo Signal with Maximum Value Normalization.

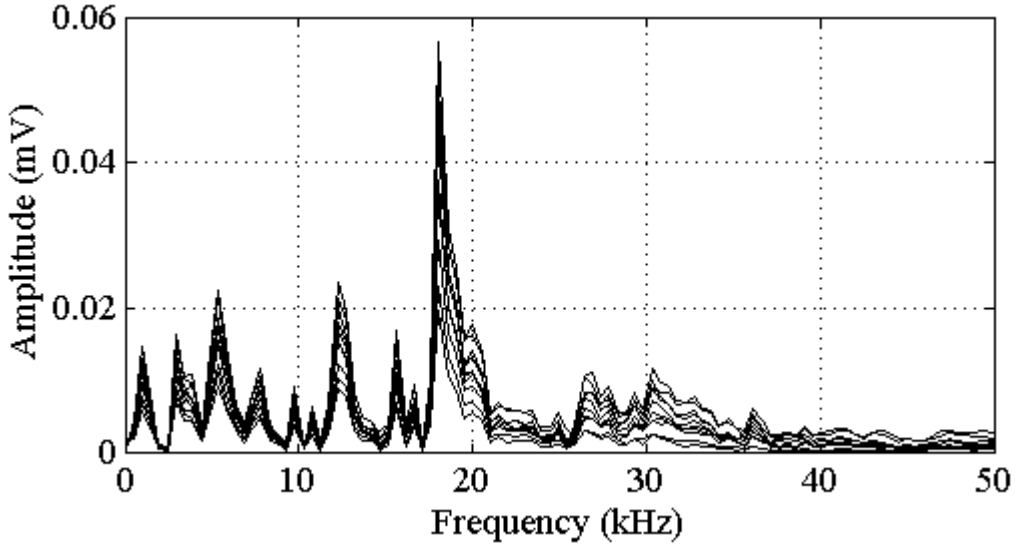

Figure 4-9. Comparison of Frequency Signals from 10 Collocated Impact-Echo Tests.

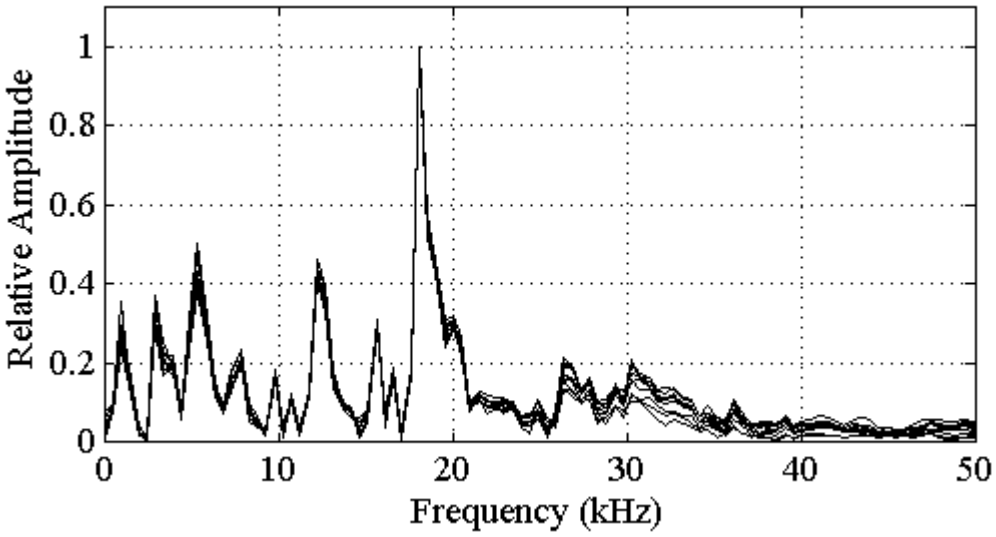

Figure 4-10. Comparison of MVN Frequency Signals from 10 Collocated Impact-Echo Tests.

If there are other frequencies of interest, inconsistent impact characteristics cause inconsistent frequency content, and maximum value normalization makes no attempt to correct for this factor. This is the case when using impact-echo to examine the steel-concrete interface, where frequency of reflections from the steel-concrete interface is not consistently coincident with the dominant frequency content. In this case, we can employ the procedure for calculating the simulated transfer function (STF) that approximates the frequency content of the impact using the shape of the R-wave in the time-displacement signal. This procedure requires that the R-wave be isolated from the time-displacement signal. Figure 4-11 shows the isolated R-wave of the typical impact-echo signal shown in Figure 4-6. On examining the R-wave, t_d can be estimated as the time between the arrival and departure of the R-wave. In this case, t_d is estimated to be 30 μs and using Eq. 4-1, f_{max} is estimated to be 41.7 kHz. The frequency content of the isolated R-wave can be determined using the FFT. Figure 4-12 shows the frequency content of the isolated R-wave in Figure 4-11. It is clear that not all frequencies are evenly excited by impact, providing further justification of the need for normalization.

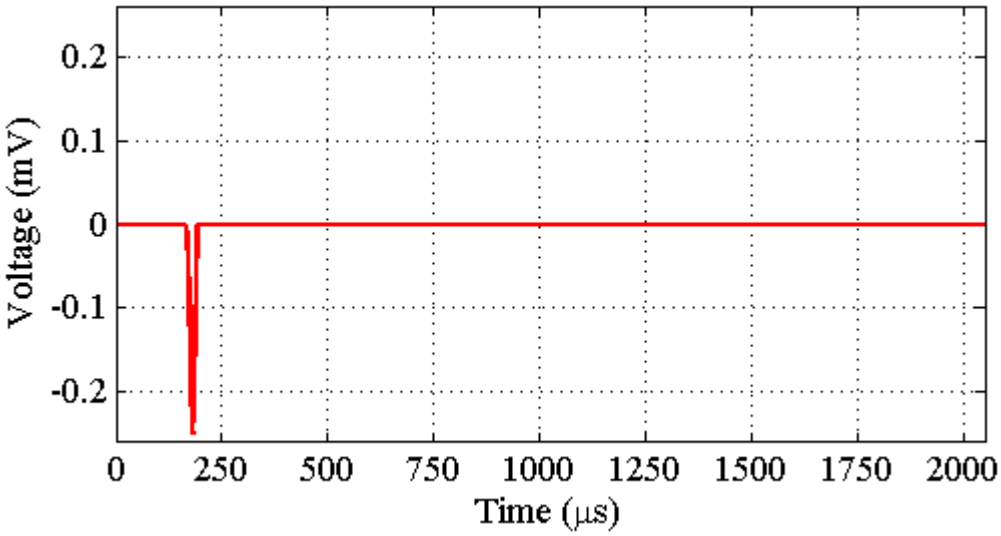

Figure 4-11. R-Wave Isolated from Typical Impact-Echo Signal.

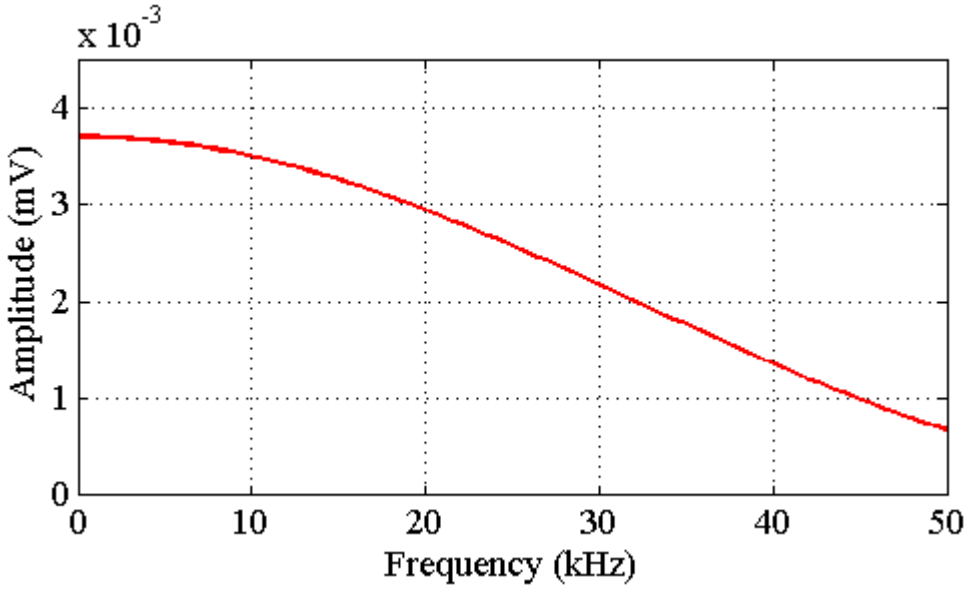

Figure 4-12. FFT of Isolated R-Wave.

The procedure for calculating the STF can be used to calculate $F_N(\eta)$ as a function of the R-wave frequency signal, $R(\eta)$, a factor F_n (Cheng et al. 2007), and $F(\eta)$ according to (Cheng and Yu 2000):

$$F_N(\eta) = \frac{F(\eta)}{F_n R(\eta)} \qquad \text{(Eq. 4-10)}$$

Figure 4-13 shows the frequency signal of the typical impact-echo signal of Figure 4-6 following the calculation of the STF. Two key differences can be observed between the frequency signals produced by the two normalization techniques. The first is that the ordinate in the STF has a

specific physical meaning. The transfer factor can be interpreted as the factor by which the amplitude at a specific excitation frequency is altered in the response. In other words, the transfer function is the response of the structure to a point excitation with amplitude equal to 1 at all frequencies below f_{max}. The transfer factor is commonly, and henceforth, referred to as the transfer amplitude to maintain the connection with traditional FFT signal processing. A value of greater than one for the transfer amplitude indicates that the excitation amplitude will be amplified in the response. To illustrate the second difference between the two normalization techniques, the amplitude profiles of the STF and MVN signals can be compared by applying the MVN to the STF signal. Figure 4-14 shows both the STF and MVN frequency signals from the typical impact echo signal shown in Figure 4-6. The profiles are roughly the same up to approximately 26 kHz, above which the relative amplitude of the STF is consistently larger than that of the MVN.

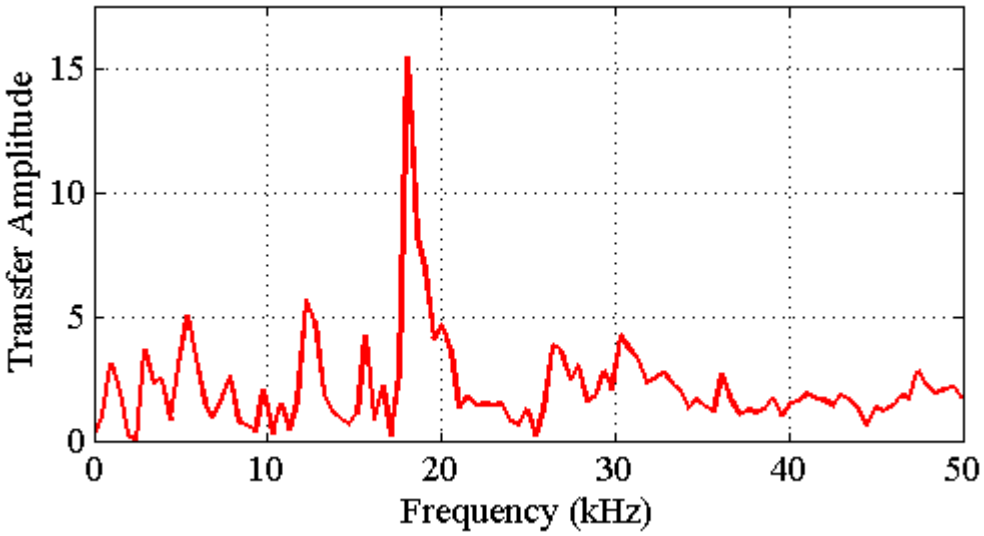

Figure 4-13. STF of Typical Impact-Echo Test.

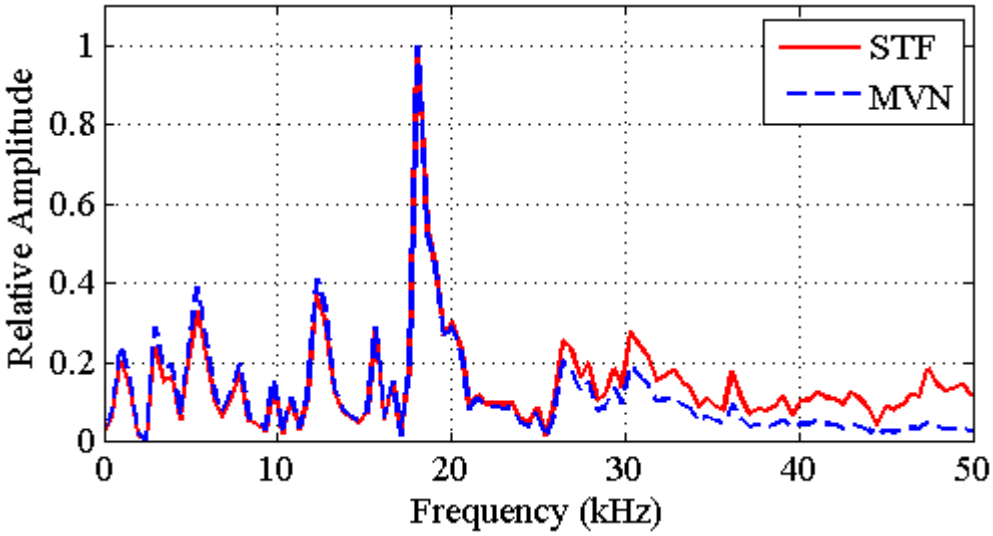

Figure 4-14. Relative Profile Comparison of STF and MVN for Typical Impact-Echo Signal.

The normalization capabilities of the STF can be further illustrated using a comparison of the frequency signals from collocated impact-echo tests. Figure 4-15 shows the STF frequency signals of the 10 collocated impact-echo tests from Figure 4-9. In this case, the variance in transfer amplitude is reduced at all frequencies below approximately 41 kHz, which is, not coincidently, very close to f_{max}. As the STF consistently normalizes amplitudes over the entire range of usable frequencies, it is the preferred normalization technique for impact-echo scanning to assess the state of the steel-concrete interface and bond in RC structures.

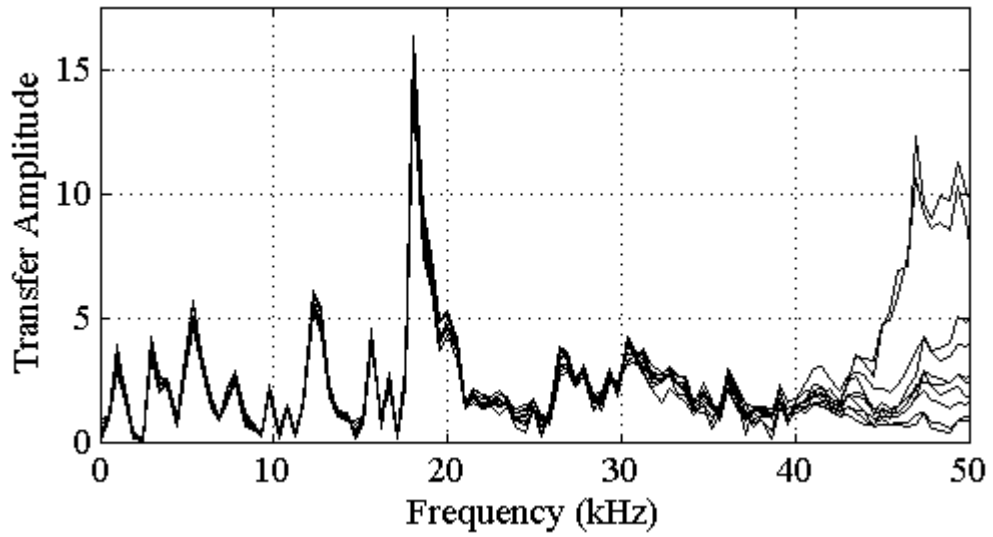

Figure 4-15. Comparison of STF Frequency Signals from 10 Collocated Impact-Echo Tests.

Once normalized, the results of adjacent tests can be shown using a color map to plot transfer amplitude as a function of test location and frequency. Figure 4-16 shows the results of an example impact-echo scan where tests are performed along an equally spaced interval, Δx, of 1 in. (25 mm). In this representation, the amplitude of the dominant frequency at 18.1 kHz is seen as a dark, horizontal line. A defect located between 12 in. (305 mm) and 20 in. (508 mm) causes an interruption in the line at the dominant frequency. Other frequencies with consistent amplitude across the spectrum are evident, but not as clear as the line at the dominant frequency.

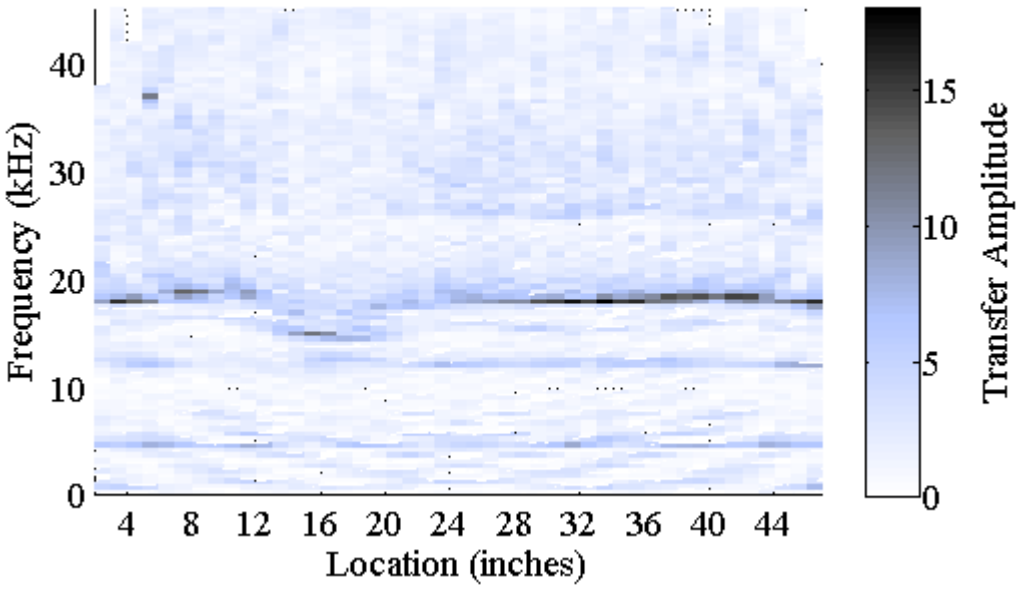

Figure 4-16. Typical Impact-Echo Scan Results (1 in. = 25 mm).

Interpreting an impact-echo scan can be done by comparing the resulting color map to a predicted baseline created using modified versions of Eq. 4-4 and Eq. 4-5. In both cases, these modifications are made in the form a correction factor that accounts for complex mechanical behavior not included in the simple models. Specifically, the modified version of Eq 4-4 is given by (Sansalone and Streett 1997):

$$f = \frac{\beta C_p}{2D} \qquad \text{(Eq. 4-11)}$$

where β is an empirically derived correction factor that is a function of cross-sectional geometry. In plate-like structures, β is assigned a value 0.96. In rectangular members, impact excites multiple cross-sectional modes vibrating at different frequencies. The different frequencies can be predicted using multiple values of β, all of which are determined as a function of the cross-

sectional aspect ratio (Sansalone and Streett 1997). The modified version of Eq. 4-5 for steel reinforcing bars is given by (Sansalone and Streett 1997):

$$f = \frac{\zeta C_p}{4D} \quad \text{(Eq. 4-12)}$$

where ζ is an empirically derived correction factor that is a function of bar diameter, d, and cover depth c, given by (Sansalone and Streett 1997):

$$\zeta = -0.6\frac{d}{c} + 1.5 \quad \text{(Eq. 4-13)}$$

The parameters D, d, and c are all geometric parameters and can be determined from construction drawings or measured using methods for obtaining in situ values. For example, an eddy-current rebar cover meter can be used to determine values for d and c. The parameter C_p is a material characteristic that can be measured using either ultrasonic pulse velocity (Zhu and Popovics 2007) or the impact-echo two-sensor configuration (ASTM C 1383, Popovics et al. 1998). The set of predicted frequencies can then be used as an approximate baseline corresponding to the response of the structure in an undamaged state. Defects can be identified in the color map by departures from the predicted baseline or the presence of high amplitudes at frequencies that are not included in the baseline set. Specifically, these frequencies correspond to reflections from the void interface, and D_v may then be calculated using Eq. 4-11. Through this procedure, voids can be located and characterized given that sufficient frequency content is generated by the impact and the sensor is capable of measuring the frequency range of interest.

4.3.4 Signal Processing

There are several identifiable characteristics of the impact-generated time-displacement signal that reduce the accuracy with which impact-echo results can be interpreted. To enhance the identification of frequency content that carries information about reflecting P-waves within a structure, additional DSP can be performed to remove content that may be considered noise. These techniques may be carried out on either the time-displacement signal or the frequency-amplitude signal representation. Time-displacement techniques consist of R-wave removal (Sansalone and Streett 1997), signal shortening, and windowing (Kahan 1993). Frequency-amplitude techniques are the autocorrelation function (Algernon and Wiggenhauser 2006) and bandwidth procedure (Algernon 2008). Examining the effects of these techniques on the frequency signal by looking at the frequency spectrum resulting from a single test can be difficult, as these techniques reveal processed signals with very minute differences from the

unprocessed signal. These effects are most noticeable when examining how they alter the results of an entire impact-echo scan. Comparison of the effects of these techniques will be made in subsequent chapters.

In the time domain, the R-wave is identified as the first relatively large negative displacement in the signal. As the FFT reveals the average frequency content over the duration of the signal, the frequency content of the R-wave displacement can mask other frequencies of interest in the frequency signal. As the first propagation of the R-wave past the displacement sensor is easily identifiable in the time-displacement signal, it can be removed prior to performing the FFT, thereby removing its contribution to the frequency signal (Sansalone and Streett 1997). The R-wave removal procedure can be implemented by identifying the value of the index, τ_2, of second zero-crossing after the arrival of the R-wave in the time-displacement signal, $u(\tau)$, where τ is the frequency index. The processed signal is then given by:

$$u_p(\tau) = \begin{cases} 0, & \tau \leq \tau_2 \\ u(\tau), & \tau > \tau_2 \end{cases} \quad \text{(Eq. 4-14)}$$

Figure 4-17 shows the typical impact-echo signal of Figure 4-6 after the R-wave has been removed.

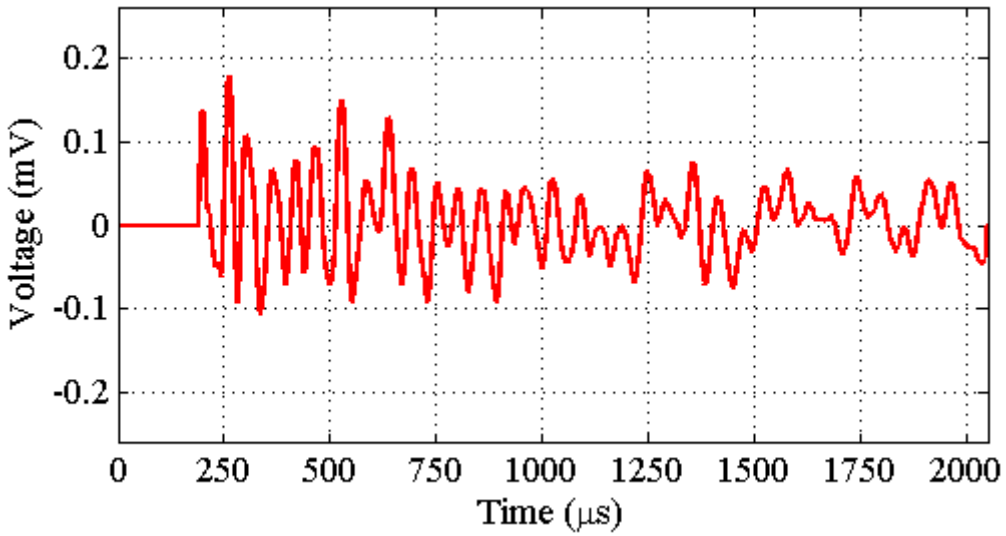

Figure 4-17. Typical Impact-Echo Signal with R-Wave Removed.

As mentioned earlier, divergence and attenuation cause a time-dependent reduction in the signal-to-noise ratio in the time-displacement signal, meaning that earlier portions of the signal contain more useful information regarding the reflection of P-waves within the structure under

examination. With the goal of countering the concerns resulting from divergence and attenuation, signal shortening and windowing seek to isolate earlier portions of signal. Prior to performing the FFT, signal shortening simply shortens a signal of length *N* by a shortening factor SF, such that the length of the processed signal remains a power of 2, according to:

$$u_p(\tau) = u(\tau),\ \tau = \tau_2, \tau_2 + 1, \ldots, \tau_2 + SF \cdot N \qquad \text{(Eq. 4-15)}$$

Taking the first index from τ_2 performs the R-wave removal procedure as part of the signal shortening procedure. As a consequence of shortening the signal, Δf is increased according to Eq. 4-8, meaning that a reduction in clarity in the frequency domain is the main consequence of employing this technique. Figure 4-18 shows the typical impact-echo signal of Figure 4-6 after it has been shortened by a factor of ½.

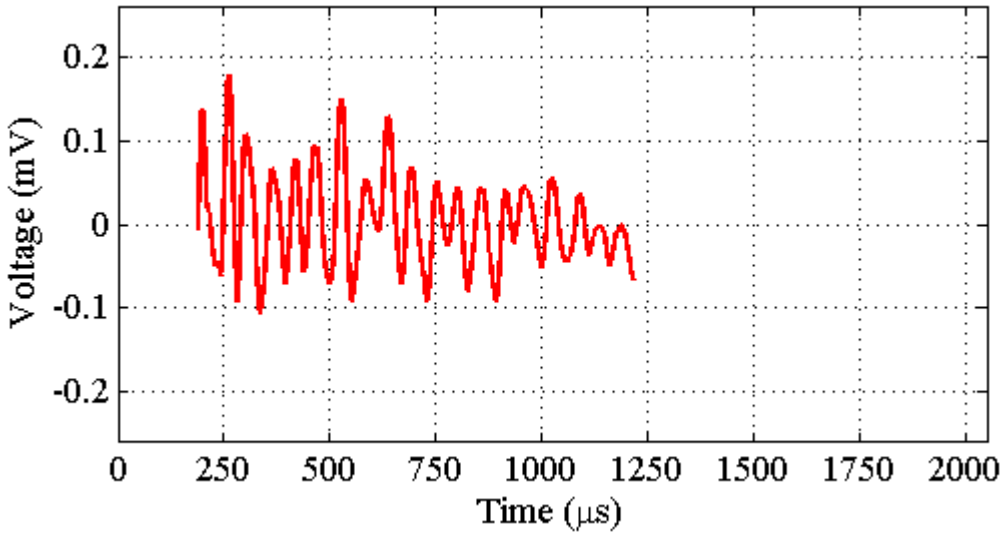

Figure 4-18. Typical Impact-Echo Signal after Signal Shortening.

Windowing procedures take a similar approach without decreasing Δf. In procedures of this type, a windowing function $g(\tau)$ (Kahan 1993) is used to weight the time displacement signal so that the portion with a higher signal-to-noise ratio is emphasized. The processed signal is calculated according to:

$$u_p(\tau) = u(\tau)g(\tau) \qquad \text{(Eq. 4-16)}$$

Figure 4-19 shows the typical impact-echo signal of Figure 4-6 after a windowing function has been applied.

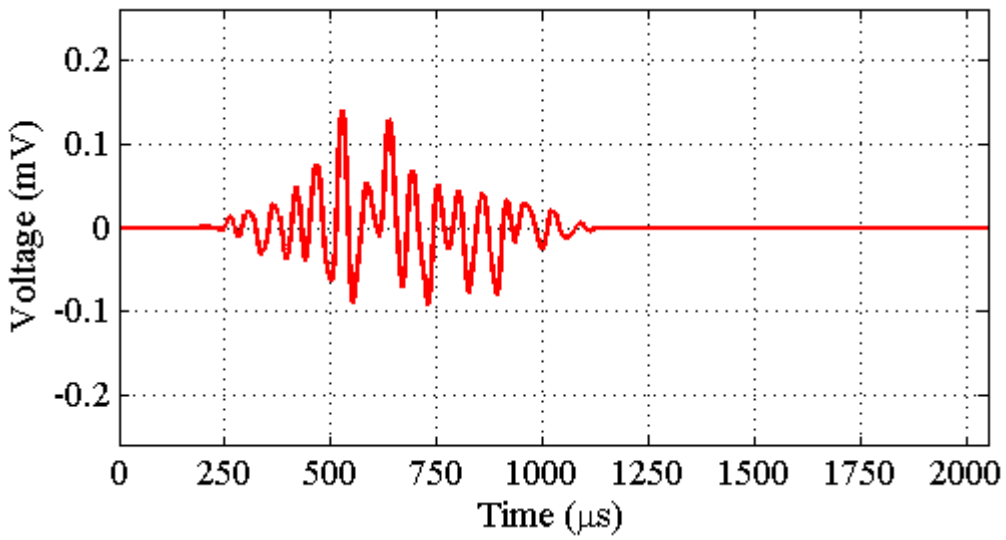

Figure 4-19. Typical Impact-Echo Signal after Windowing.

The P-wave reflection components of the time-displacement signal are strongly harmonic, while the contributions of geometry effects typically are not. This difference highlights the usefulness of the autocorrelation function, a signal processing tool that emphasizes the harmonic components of a signal to which it is applied. Autocorrelation achieves this emphasis by searching for repeating patterns within the signal, giving it the ability to find periodic signals in the presence of noise (Algernon and Wiggenhauser 2006). The autocorrelation function can be applied to create the processed frequency signal $F_p(\eta)$ according to (Bracewell 2000):

$$F_p(\eta) = N|F(\eta)|^2 \qquad \text{(Eq. 4-17)}$$

Attenuation and divergence have a greater effect on higher frequency components and therefore higher frequency reflections exist with shorter duration in the time-displacement signal. These higher frequency reflections are said to have larger bandwidth relative to lower frequency reflections. In the frequency spectrum, higher bandwidth components can be masked by noise as a result of the FFT representing the average frequency content over the duration of the signal. The relative bandwidth of specific frequency content, $B(\eta)$, can be indicated by the distance between the relative minima that bound each peak in the frequency spectrum. Calculating $F_p(\eta)$ using the bandwidth procedure is done by using the bandwidth weighting function $B(\eta)$ according to (Algernon 2008):

$$F_p(\eta) = |F(\eta)|B(\eta) \qquad \text{(Eq. 4-18)}$$

The use of these techniques can lead to different results in different applications of impact-echo. Selection of useful techniques should be done once the frequency content of interest is known. For this reason, an assessment of these techniques is carried out in the context of the laboratory experiments presented in Chapter 5.

4.4 SUMMARY

Multiple methods for NDE of RC structures have been investigated for their ability to assess the interface between concrete and reinforcing steel in ASR/DEF affected structures. An exploration of available techniques was centered on established techniques for assessing RC structures, and the selection of a viable method was made on the basis of reported use in similar applications, commercial availability, and field applicability. The technique with the most potential for assessing the steel-concrete interface was determined to be the impact-echo method. A review of the theories comprising the impact-echo method was presented, including stress-wave propagation in concrete, observation of this physical phenomenon, adaptation of impact-echo into a scanning technique, and post-processing techniques to improve the accuracy with which impact-echo results can be interpreted. This chapter presented background information for the understanding of the impact-echo laboratory experimental program and application of impact-echo to large-scale samples exhibiting ASR damage presented in subsequent chapters.

5 IMPACT-ECHO: LABORATORY EXPERIMENTAL PROGRAM

5.1 INTRODUCTION

Though a large base of research exists regarding the impact-echo method, a limited amount of research is reported on the specific application of impact-echo for assessing the integrity of steel-concrete interface in RC structures. The available research in this area indicates that impact-echo may be a viable technique for performing this assessment, but no effort has been made to assess the limitations of the technique, and the procedural details for collecting and analyzing data on a large scale are absent. The efforts presented in Chapters 5 and 6 seek to combine the concepts presented in Section 4.3 to establish the limitations and procedural details for the evaluation of the steel-concrete interface in ASR/DEF affected structures. Prior to examining large-scale specimens affected by ASR/DEF, the technique is assessed under controlled conditions to establish the bounds for detection of defects around steel reinforcement in field applications. For this purpose, a commercially available impact-echo system is used to examine a set of small-scale samples in a laboratory setting. The goal of this small-scale experiment is to determine which defect-size characteristics significantly affect the accuracy of defect detection, and to establish the bounds of these characteristics in which a defect may be detected. Additionally, procedures for collecting and processing data are sought so that the accuracy of detection is maximized.

5.2 EXPERIMENTAL DESIGN

As presented in Section 2.3, core samples taken from large-scale exposure specimens diagnosed with ASR showed a buildup of ASR gel at the steel-concrete interface. The goal of assessing this interface using impact-echo is to locate and characterize the potential debonding of steel caused by these gel formations, so that this knowledge can be used to better predict structural performance. With this goal in mind, the samples in this study contain defects of simple geometry and various sizes that presumably mimic the formation of ASR gel at the steel-concrete interface in the large-scale exposure samples.

5.2.1 Sample Geometry

The samples used in this laboratory experiment are prismatic concrete members that are 48 in. (1219 mm) long, 10 in. (254 mm) wide, and 5 in. (127 mm) deep. Reinforcing bars (#8, #25M) with an average measured diameter of 0.94 in. (24 mm) are placed such that the cover depth is 2 in. (51 mm) from the top [10 in. (254 mm) by 48 in. (1219 mm)] face. The lateral distance, b_b, from the side [5 in. (127 mm) by 48 in. (1219 mm)] face to the surface of the reinforcing bar varies within the experiment. Samples contain either one or two reinforcing bars, the latter containing adjacent reinforcement, mimicking a lap-splice region. The defects consist of adhesive materials that are evenly applied around the perimeter surface of a reinforcing bar. The geometry of the defects can be completely characterized with two experimental variables: the radial thickness, T_d, the distance from the surface of the rebar to the surface of the defect and the length, L_d, of the defect along the reinforcing bar. The values selected for cover depth and reinforcing bar diameter indicate that the samples are full-scale in these dimensions, as these values mirror those of the field structures. The behavior of P-waves reflecting from the interfaces associated with these dimensions should then reflect their behavior in full-scale structures. Thus, the samples examined in this experiment are only considered small-scale in their cross-sectional dimensions. Figure 5-1 shows the geometry of samples containing one reinforcing bar. Figure 5-2 shows the geometry of samples containing two reinforcing bars.

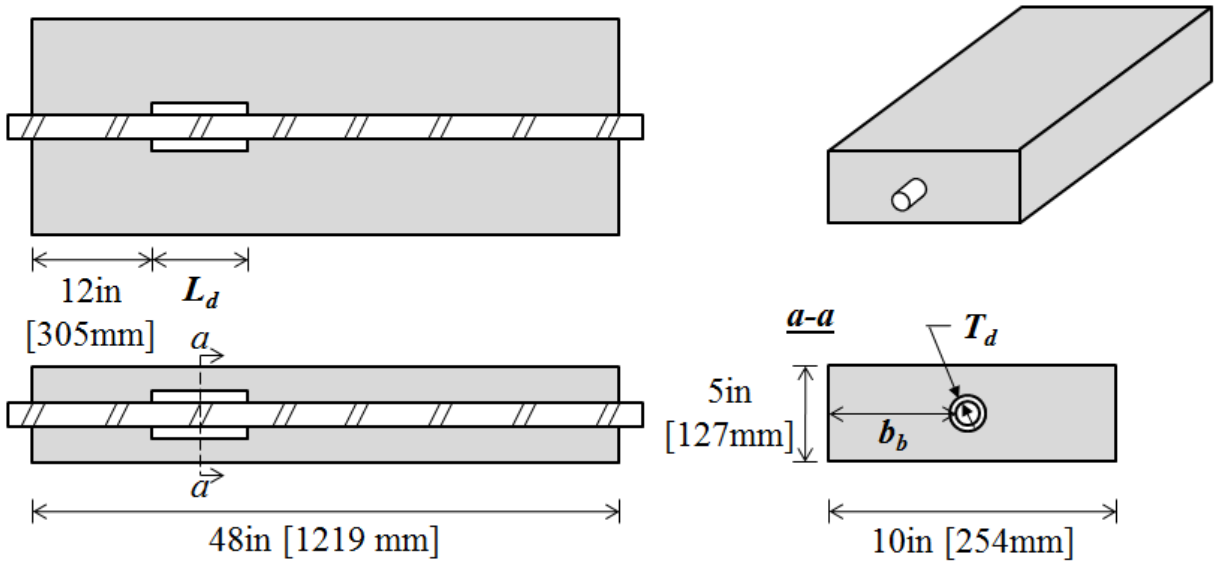

Figure 5-1. Geometry of Samples Containing One Reinforcing Bar.

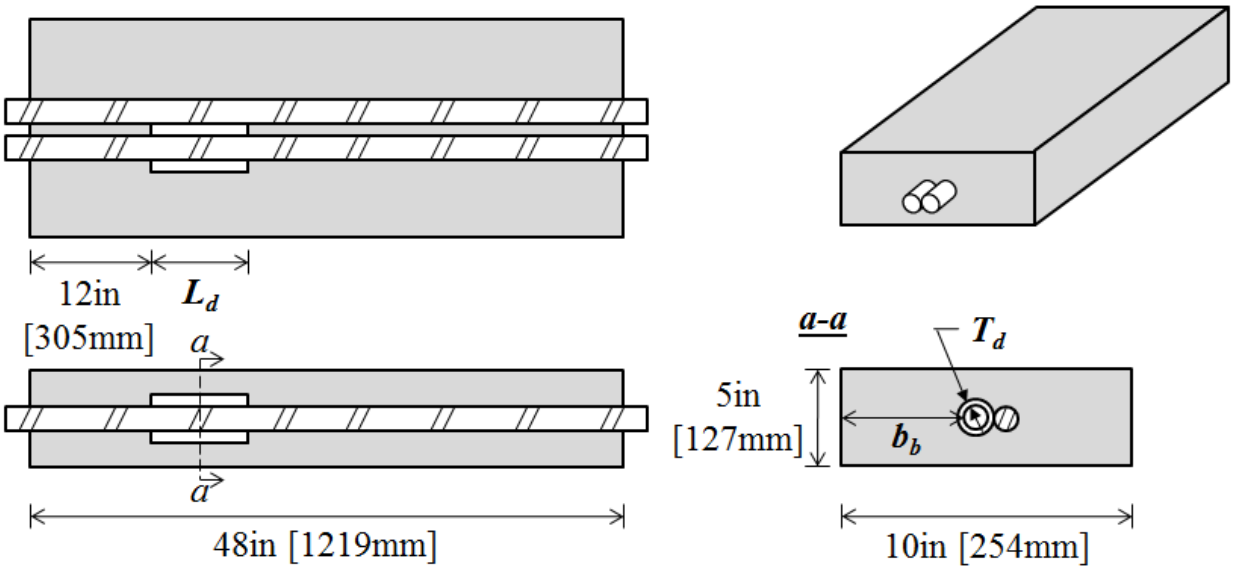

Figure 5-2. Geometry of Samples Containing Two Reinforcing Bars.

Table 5-1 shows the values assigned to experimental variables for each of the 10 samples evaluated in this chapter. Samples are designed with one and two reinforcing bars such that the effects on the detection of defects at the steel-concrete interface using impact-echo when adjacent bars have different interface conditions are assessed. The minimum value for L_d is chosen to be equal to the approximate value of 2 in. (51 mm) for r in the employed impact-echo system. This means that the reflection of waves will occur at a consistent interface along the length between the impact-point and the transducer, so that the simple models described by Eq. 4-11 and Eq. 4-12 can be used to predict the reflection frequency. Other values of L_d are 4 in. (102 mm) and 8 in. (203 mm). The minimum value assigned to T_d, 0.005 in. (0.13 mm), is the minimum value for which the adhesive could be applied evenly along L_d. This thickness value is obtained using a digital caliper to measure the diameter of the bar and the defect. Subsequent coats of adhesive were applied to produce thickness values of approximately 0.008 in. (0.20 mm) and 0.010 in. (0.25 mm). Some variation is noted in these values due to the difficulty in achieving perfect consistency in thickness with relatively small values of T_d. T value assigned to b_b places the geometric center of the reinforcement coincident with the geometric center of the cross-section.

Table 5-1. Values of Experimental Variables in Laboratory Experiment.

Sample ID	Number of Reinforcing Bars	Defect Length, L_d in. (mm)	Defect Thickness, T_d in. (mm)	Lateral Bar Placement, b_b in. (mm)
S1	1	8 (203)	0.010 (0.25)	4.5 (114)
S2	1	4 (102)	0.010 (0.25)	4.5 (114)
S3	1	2 (51)	0.010 (0.25)	4.5 (114)
S4	1	8 (203)	0.008 (0.20)	4.5 (114)
S5	1	8 (203)	0.005 (0.13)	4.5 (114)
D1	2	8 (203)	0.010 (0.25)	4 (102)
D2	2	4 (102)	0.010 (0.25)	4 (102)
D3	2	2 (51)	0.011 (0.28)	4 (102)
D4	2	8 (203)	0.007 (0.18)	4 (102)
D5	2	8 (203)	0.005 (0.13)	4 (102)

5.2.2 Sample Materials

Concrete was mixed with a water-to-cement ratio of 0.48. Type III cement was used and a measured 28-day compressive strength of 4400 psi (30 MPa) was determined using standard cylinder testing (ASTM C 39). Reinforcing bars meet ASTM Grade 60 requirements. The adhesive used to create defects was a spray-on rubber. It is assumed here that the acoustic impedance of the rubber is less than that of concrete. This assumption is later confirmed.

5.3 DATA COLLECTION

Data were collected using a commercially assembled point-test impact-echo system. Prior to performing point by point scans, C_p is measured using the two transducer method. Thirty speed tests are performed on each sample and the sample mean and coefficient of variation (COV) are calculated from sample data. Though multiple records are captured for each sample, a malfunction in the A/D system introduced an effective noise that did not allow for proper data processing in all records. Only the n records for which the system malfunction did not interfere with wave speed calculations are included in the calculation of sample statistics.

Reflection frequencies are predicted using the mean value for C_p, sample geometry, and Eq. 4-11 and Eq. 4-12. The cross-sectional dimensions of the samples give rise to two modal vibration frequencies, f_{D1} and f_{D2}, calculated according to Eq. 4-11. The frequency, f_{D1}, is the frequency associated with the P-wave reflections from the external boundary at the full depth of the member. The frequency of reflections from an undisturbed steel concrete interface, f_{bonded}, is calculated according to Eq. 4-12. The frequency of P-wave reflections from an interface containing a defect, f_{defect}, is calculated according to Eq. 4-11. The results of the speed testing and frequency prediction are shown in Table 5-2. Sample mean values of C_p range from 13,367 ft/s (4074 m/s) to 14,989 ft/s (4569 m/s) with COVs no greater than 0.072. The minimum difference between predicted frequencies is 6.4 kHz. The maximum value of Δf should be half of this difference to ensure that the frequencies of interest are always distinguishable from one another.

Table 5-2. Results of Speed Testing and Frequency Prediction.

Sample ID	Samples, n	C_p ft/s (m/s)	COV	f_{D1} (kHz)	f_{D2} (kHz)	f_{bonded} (kHz)	f_{defect} (kHz)
S1	20	14,277 (4352)	0.038	17.1	34.3	26.1	42.9
S2	24	14,507 (4422)	0.050	17.4	34.8	25.9	42.1
S3	27	14,989 (4569)	0.072	18.0	36.0	26.3	42.6
S4	29	13,879 (4230)	0.034	16.7	33.3	24.9	40.6
S5	12	14,268 (4349)	0.071	17.1	34.2	25.0	40.6
S6	12	13,367 (4074)	0.068	16.0	32.1	23.8	38.8
D1	30	14,647 (4464)	0.041	17.6	35.2	27.9	46.5
D2	24	14,837 (4522)	0.049	17.8	35.6	28.7	48.0
D3	29	14,409 (4392)	0.035	17.3	34.6	26.5	43.6
D4	29	14,529 (4428)	0.056	17.4	34.9	28.1	47.0
D5	28	14,278 (4352)	0.054	17.1	34.3	27.2	45.2

5.3.1 Procedural Details

Impact-echo tests are performed on the 10 in. (254 mm) by 48 in. (1219 mm) face with the impact and sensor located directly above the reinforcing bar. The impact is generated using an impactor consisting of a steel sphere with diameter 0.25 in. (6.3 mm) attached to a spring rod. The associated value for t_d is 27 μs, which, by use of Eq. 4-1, results in an f_{max} of 46.3 kHz. The sensor is a piezoelectric displacement transducer with a flat response between 1 kHz and 67 kHz. This range includes all of the predicted frequencies in Table 5-2. The test procedure consists of the operator consistently impacting the specimen such that r is greater than 1.23 in. (31 mm) and less than 1.73 in. (43 mm). The lower limit of this range is half of the diameter of the transducer casing, and the upper limit is determined by adding half of the diameter of the transducer casing to an approximate distance within which impact can be made consistently by the operator. The diameter of the transducer casing is 2.46 in. (62 mm) and impact is made consistently within

approximately 0.50 in. (12 mm) from the edge of the transducer casing. Using the limits of this range with Eq. 4-6, the interfaces below 4.33 in. (110 mm) should be consistently detected by this configuration, with interfaces below 3.08 in. (78 mm) possibly detected. However, there is no indication that this equation takes into account reflections from an interface where $Z_1 < Z_2$, such as the steel-concrete interface, for which the frequency of reflection is described by Eq. 4-12. Because the periodic distance of reflection is 4 in. (101.6 mm) for the interface between concrete and steel in these samples, it is hypothesized that reflections of this frequency will appear in the impact-echo response of this specific configuration. As a consequence of r, the frequency, f_{defect}, may not be present in the recorded response.

Impact-echo tests are performed at an interval of 1 in. (25.4 mm) along the length of the sample. Sampling is performed using values of 1 μs and 2048 samples for Δt and N, respectively, resulting in a Δf of 0.488 kHz using Eq. 4-8. This value results in roughly 13 frequency intervals between the most closely spaced predicted frequencies. The maximum observable frequency due to the value chosen for Δt is 100 kHz using Eq. 4-7. Aside from requiring extra data storage, there is no disadvantage to providing this level of redundancy in the testing parameters. These values were therefore selected to provide maximum resolution in the frequency domain. To measure the variance in the results of individual tests, 10 tests are performed at each interval, and the mean value and COV are determined in the frequency domain. The results of individual tests are normalized using the procedure for calculating the simulated transfer function prior to calculating sample statistics and plotted as a function of test location using a color map.

5.3.2 Signal Processing

The options for additional signal DSP are examined by applying the techniques introduced in Chapter 2 to the scan results from sample S1. The techniques are applied individually and in appropriate combinations. Their effects are examined qualitatively to determine which signal processing techniques increase the clarity of the signal. After this combination of DSP techniques has been established, it will be used to process the results of impact-echo scanning on the remaining samples. Figure 5-3 shows the mean results of 10 scans performed on sample S1. The dominant frequency content is first identified as the line with the highest mean amplitude near f_{D1}. From Table 5-2, the predicted value for f_{D1} is 17.1 kHz, and

the dominant line of frequencies is observable at approximately 18 kHz. The slight difference in the predicted and observed frequencies may be due to the increase in cross-sectional stiffness caused by the presence of the reinforcing bar. This increase is not accounted for in the simple model for P-wave reflection represented by Eq. 4-11. There is a break in the dominant line between 12 in. (305 mm) and 20 in. (508 mm) corresponding to the location of the defect at the steel-concrete interface. In the interval between 12 in. (305 mm) and 20 in. (508 mm), the dominant frequency shifts to approximately 15 kHz due to the decrease in the stiffness of the cross-section resulting from the presence of the defect. Therefore, the interruption in the line of dominant frequency content may be used as an indicator of the defect in these samples. The dominant frequency content is strongly sensitive to changes in cross-sectional stiffness, and in ASR/DEF-affected structures, the associated map cracking may cause a reduction in cross-sectional stiffness, thereby altering the dominant frequency content without necessarily indicating the presence of a defect. Additionally, this frequency content is a result of the small-scale nature of this experiment, and therefore this defect indicator should not be used to detect defects at the steel-concrete interface in full-scale samples.

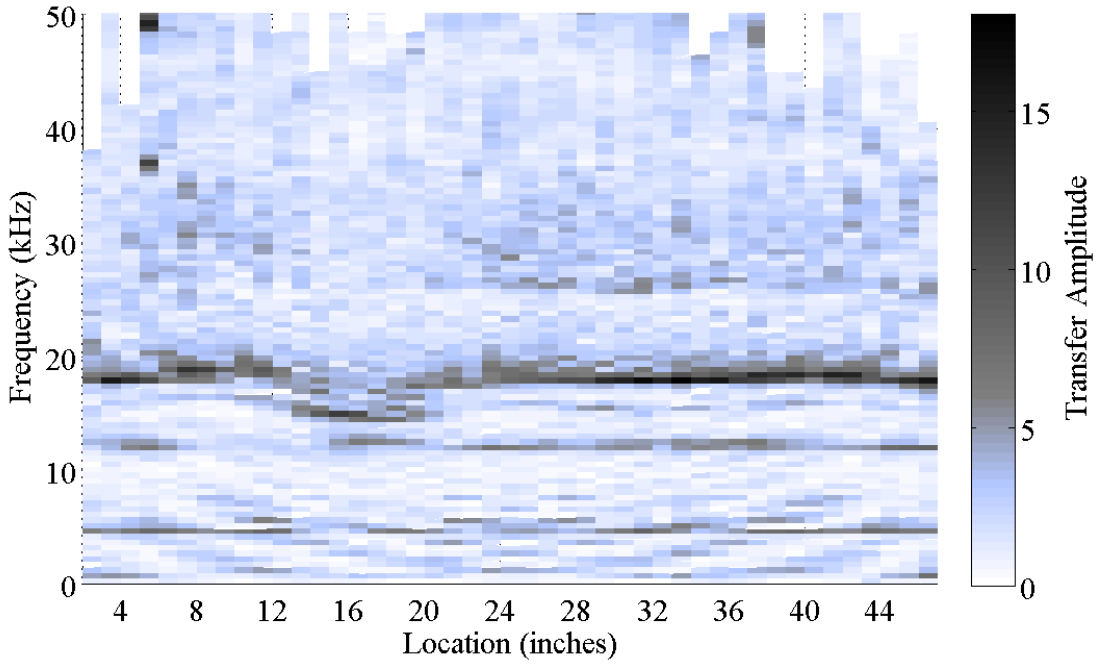

Figure 5-3. Mean Results of 10 Impact-Echo Scans of Sample S1 (1 in. = 25 mm).

After identifying the dominant frequency content, the portion of the response attributed to reflections from the steel-concrete interface can be located at approximately 26 kHz, which is in

good agreement with the predicted value of f_{bonded} of 26.1 kHz from Table 5-2. This line is interrupted between 12 in. (305 mm) and 20 in. (508 mm), which corresponds to the location of the defect at the steel-concrete interface. This confirms the assumption the acoustic impedance of the rubber defect is less than that of concrete, as the interface containing a defect is not reflecting the P-waves according to Eq. 4-12. Therefore, the interruption in the line of frequency content associated with P-wave reflections from the steel-concrete interface may be used as a defect indicator in these samples. Additionally, this content may be useful in detecting defects in full-scale samples due to the full-scale nature of the excitation, geometry, and material properties that influence this portion of the response. Above 26 kHz, there is no distinguishable frequency content. The second modal frequency, f_{D2}, may not be excited due to both the frequency content of the impact and the geometry of the sample. The frequency content at f_{defect} is also not distinguishable. The apparent absence of content at f_{defect} is likely due to the value of r, which is a consequence of the physical dimensions of the displacement sensor and cannot be overcome while using this specific impact-echo system. Thus, a void can be located using the response at f_{bonded}, but not characterized due to the absence of the f_{defect} response in the recorded signal.

At some relatively high frequencies, an absence of data can be observed. This is due to variation in the measured value of t_d and corresponding f_{max}. Only the frequency content below f_{max} is included in the calculation of sample mean and sample COV, leaving an absence of usable frequency content in the color map at some locations. Below 10 kHz, the viewable frequency content can be attributed to geometry effects on reflecting surface and body waves. The faint line of frequency content at approximately 12 kHz is not attributable to any of the reported or predicted content. This content may be the results of a surface wave or the surface component of a body wave reflecting from the external boundaries, effectively grouping it with the geometry effects. Figure 5-4 shows the sample COV corresponding to the data used to generate Figure 5-3. In general, the sample COV is low in the portions of the response where there is significant recorded frequency content. Above approximately 35 kHz, the COV becomes relatively large.

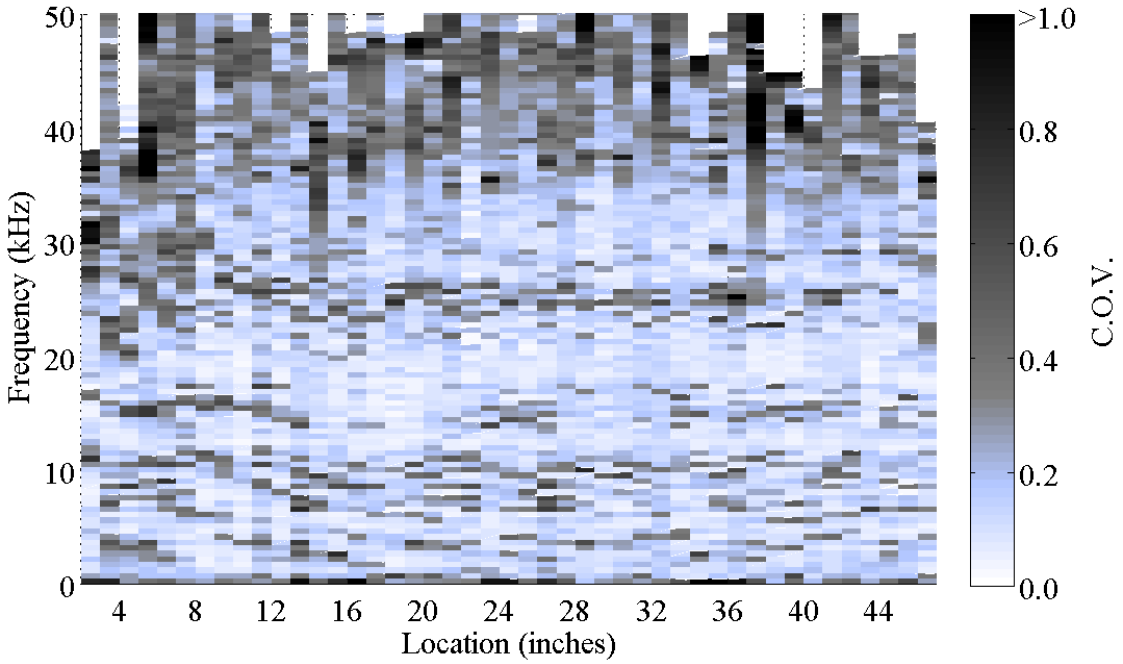

Figure 5-4. COV of 10 Impact-Echo Scans of Sample S1 (1 in. = 25 mm).

The reflection and refraction of the P-wave from the steel-concrete interface gives rise to multiple wave paths within the cover concrete and the steel bar, meaning that the surface displacements occur quasi periodically at a group of closely spaced, but not identical frequencies. In the scan result, the P-wave reflections from a sufficiently bonded interface appear in the frequency response at a range of frequencies, the lower bound of which is the predicted value, f_{bonded}. The interruption in the f_{bonded} content is the defect indicator that is likely to translate well from the small-scale laboratory testing to assessing the steel-concrete interface in field structures. Thus, the full scan results can be narrowed to examine only this content as a function of the test location. In this study, the f_{bonded} content is isolated at each test location by taking the mean value of the amplitude over the range of frequencies associated with P-wave reflections from a sufficiently bonded steel-concrete interface. The results of this procedure are plotted as a function of test location. Figure 5-5 shows the narrowed frequency response for the scan of sample S1, with sample mean shown with ±1 sample standard deviation. In this representation, relatively low mean values of the transfer amplitude can be observed between 8 in. (203 mm) and 24 in. (610 mm), with the most dramatic contrast in amplitude values at the location of the defect between 12 in. (305 mm) and 20 in. (508 mm).

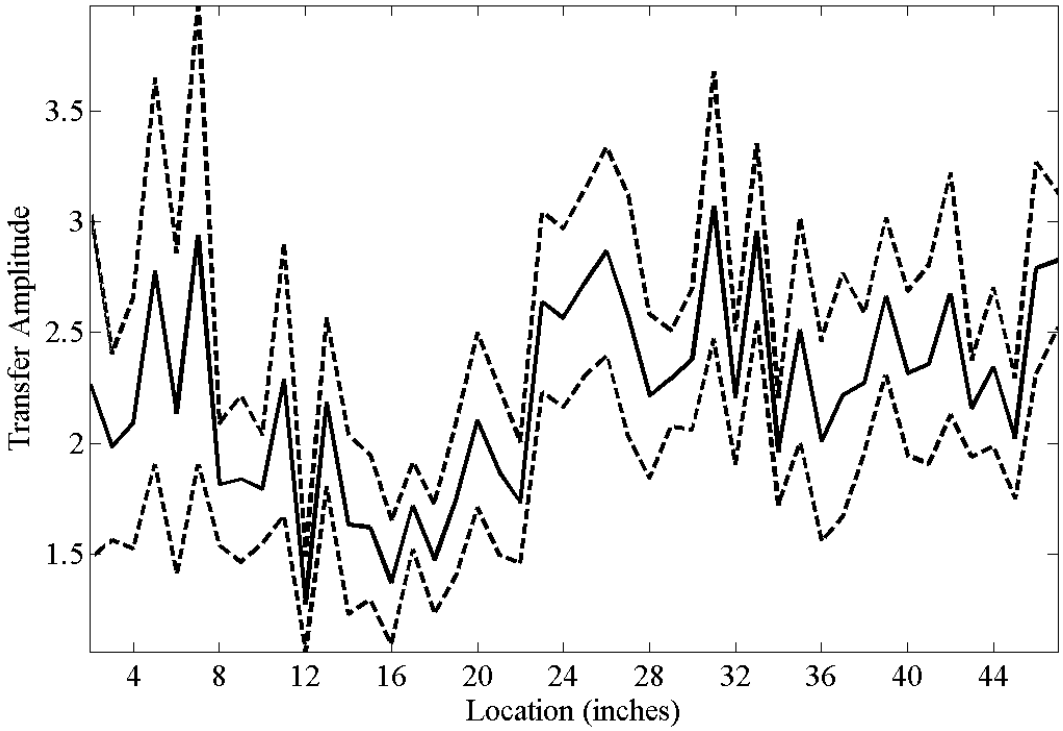

Figure 5-5. Narrowed Results of 10 Impact-Echo Scans of Sample S1 (1 in. = 25 mm).

The observations that are made based on that data presented in Figure 5-5 can be seen more clearly after the application of a smoothing technique to the data. In this case, the smoothing technique is a running mean, where the smooth value at a specific location represents the mean of the data taken at that location and both adjacent data sets. Figure 5-6 shows a smoothed frequency response for the scan of sample S1. In this case, there is no dramatic change in the conclusion that can be made based on the smoothed data, but the qualitative examination of the data can be made without much effort. The lowest values of the mean transfer amplitude are observed between 12 in. (305 mm) and 20 in. (508 mm), which is the true location of the defect.

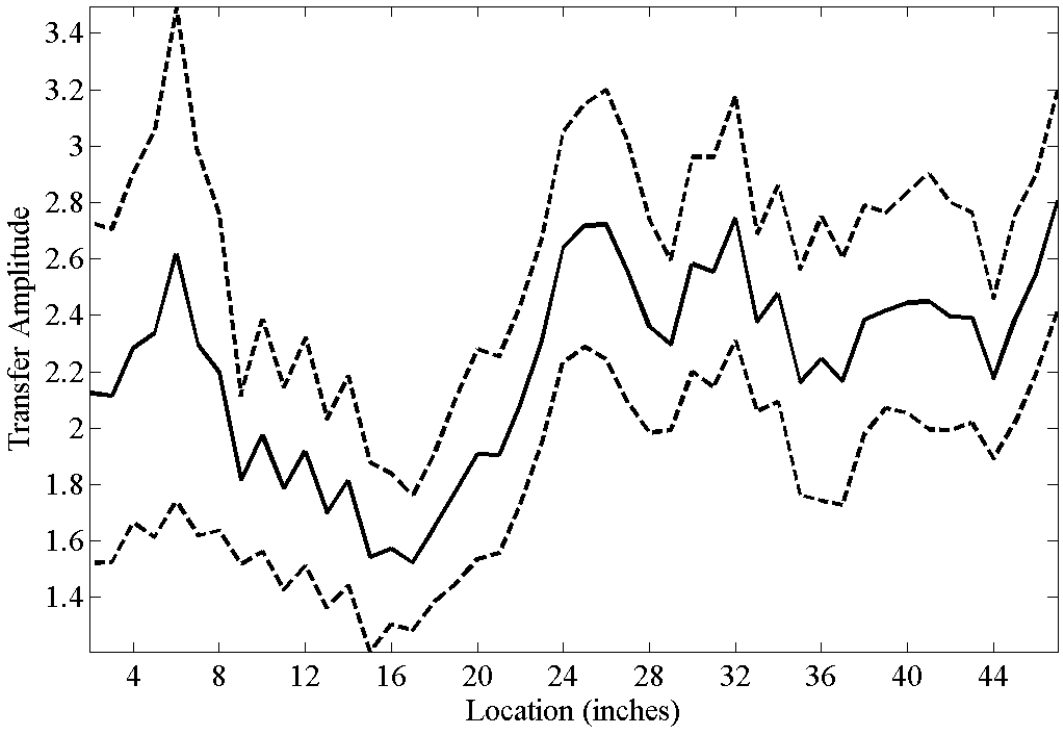

Figure 5-6. Smooth Narrowed Results of 10 Impact-Echo Scans of Sample S1 (1 in. = 25 mm).

The application of additional signal processing techniques is examined to determine which techniques may increase the qualitative confidence with which the scan results are interpreted. Figure 5-7 and Figure 5-8 show the mean and COV, respectively, of the results from the same 10 scans after they are processed using R-wave removal on the time-displacement signal. The R-wave removal slightly alters the results in this representation, and the same conclusions may be drawn as with the results without R-wave removal. Figure 5-9 shows the smooth scan results narrowed to the frequency of reflection from the steel-concrete interface after the application of R-wave removal. The mean value of the transfer amplitude is consistently diminished in the interval containing the defect, i.e., from 12 in. (305 mm) to 20 in. (508 mm). The dip is more pronounced than in the results without R-wave removal shown in Figure 5-6. The increase in the confidence with which the defect can be detected suggests that R-wave removal is useful and should be used to process all signals.

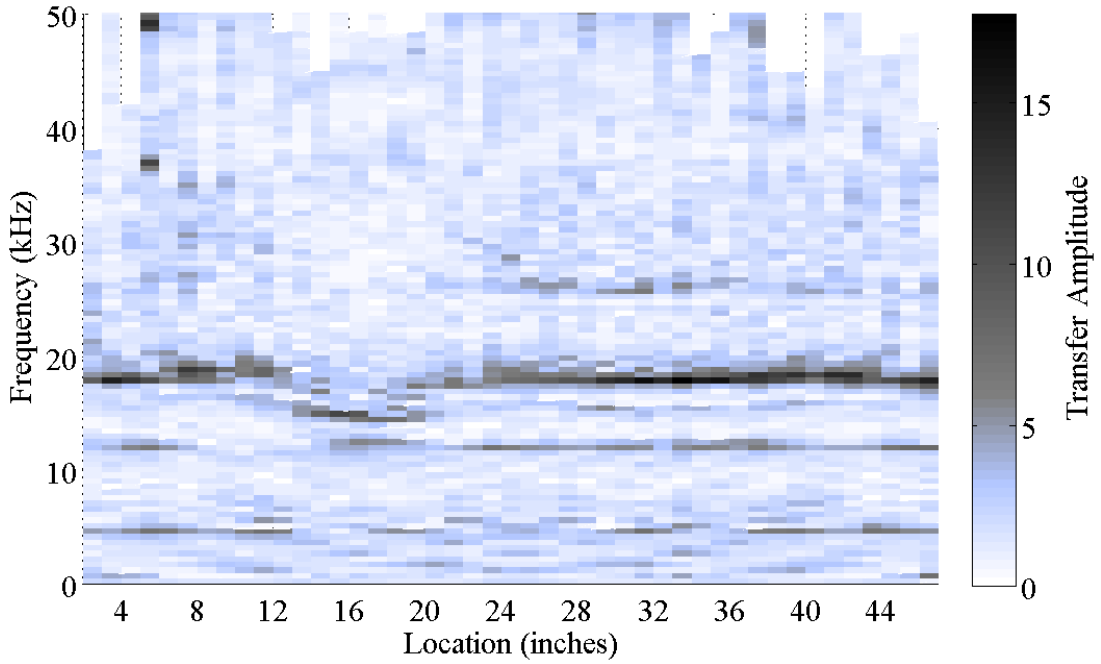

Figure 5-7. Mean Results of 10 Impact-Echo Scans of Sample S1 Processed Using R-Wave Removal (1 in. = 25 mm).

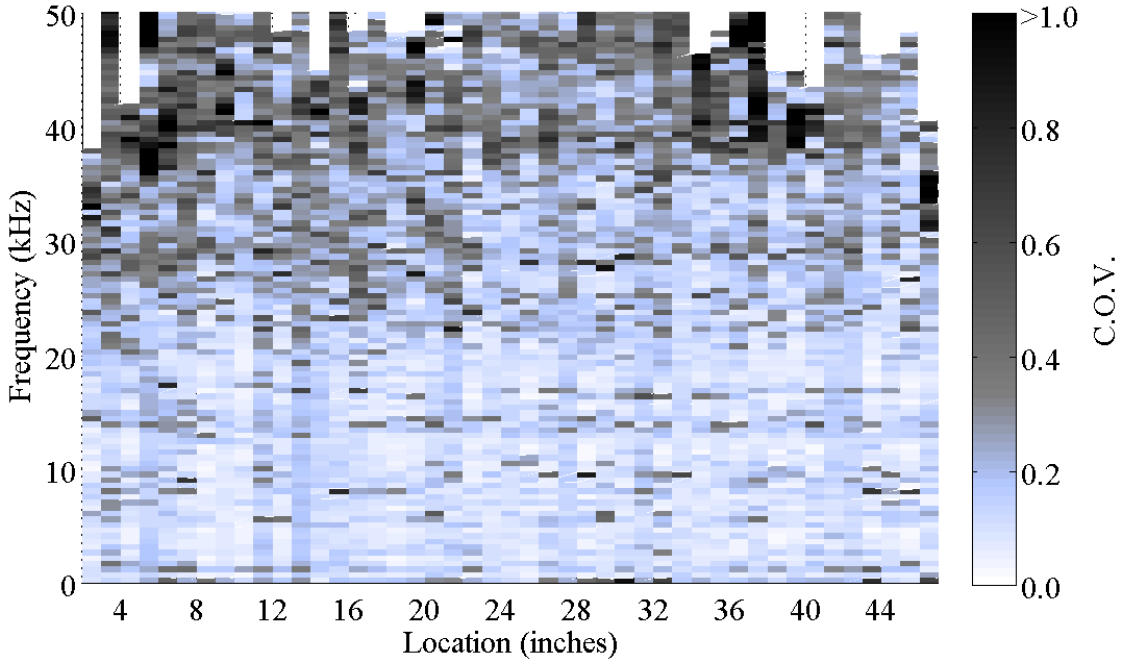

Figure 5-8. COV of 10 Impact-Echo Scans of Sample S1 Processed Using R-Wave Removal (1 in. = 25 mm).

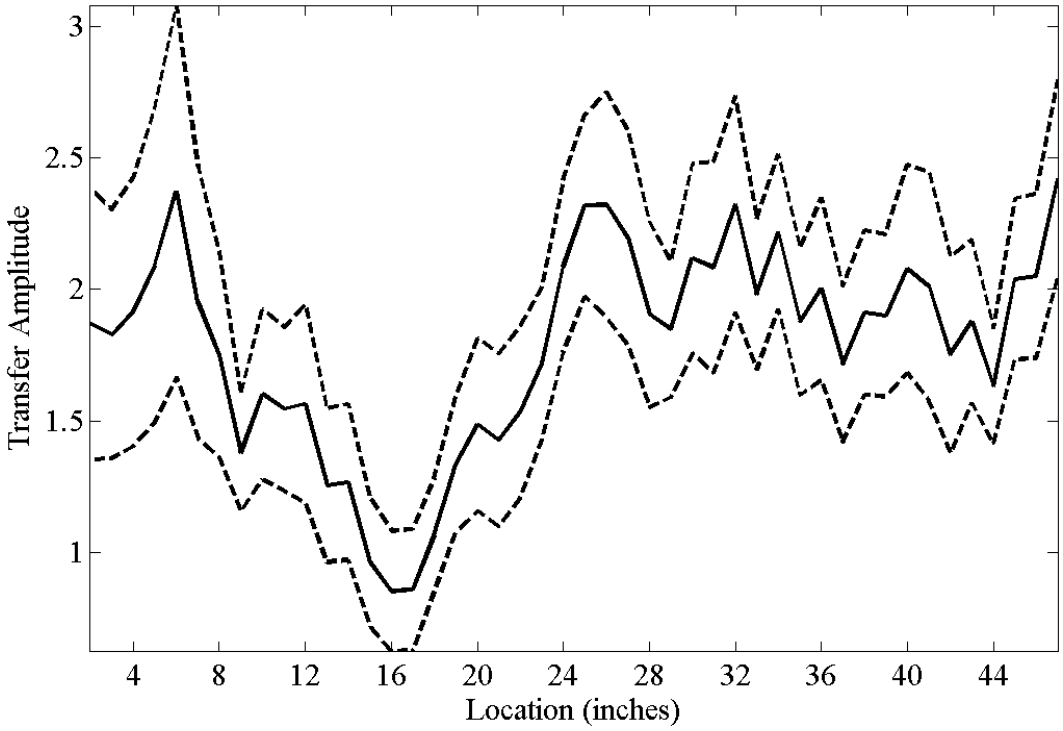

Figure 5-9. Smooth Narrowed Results of 10 Impact-Echo Scans of Sample S1 Processed Using R-Wave Removal (1 in. = 25 mm).

Figure 5-10 and Figure 5-11 show the mean and COV, respectively, of the results from the same 10 scans after they are processed using signal shortening on the time-displacement signal with (a) $SF = ½$ and (b) $SF = ¼$. The signal shortening process does not alter this representation of the data in any way that improves the qualitative detection of the defect using the f_{bonded} content. Figure 5-12 shows the smooth scan results narrowed to the frequency of reflection from the steel-concrete interface after the application of signal shortening with (a) SF = ½ and (b) SF = ¼. Both applications of the signal shortening technique show a reduction in the transfer amplitude in the interval containing the defect. As with the R-wave removal technique alone, the dip in the mean transfer amplitude is more pronounced than in the unprocessed results shown in Figure 5-5.

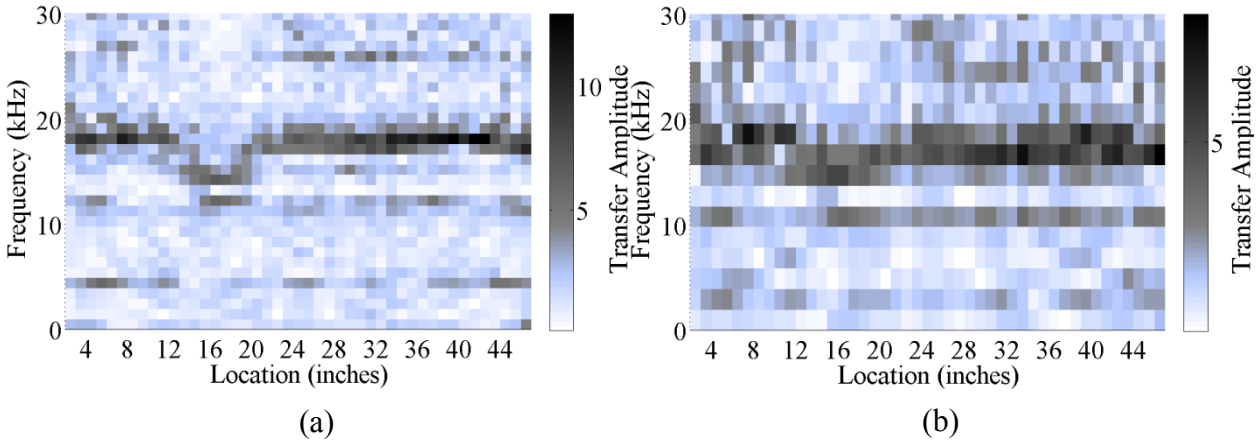

Figure 5-10. Mean Results of 10 Impact-Echo Scans of Sample S1 Processed Using Signal Shortening with (a) *SF* = ½ and (b) *SF* = ¼ (1 in. = 25 mm).

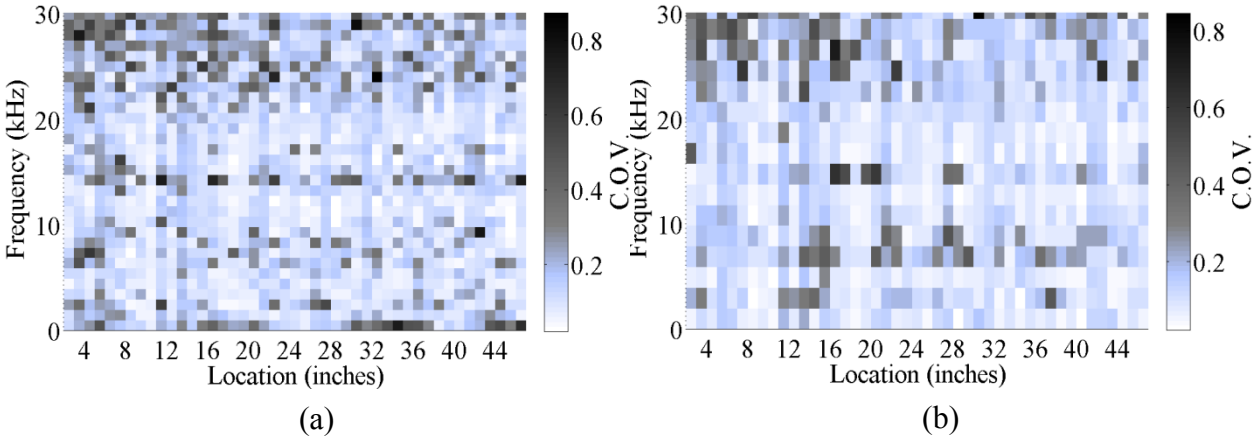

Figure 5-11. COV of 10 Impact-Echo Scans of Sample S1 Processed Using Signal Shortening with (a) *SF* = ½ and (b) *SF* = ¼ (1 in. = 25 mm).

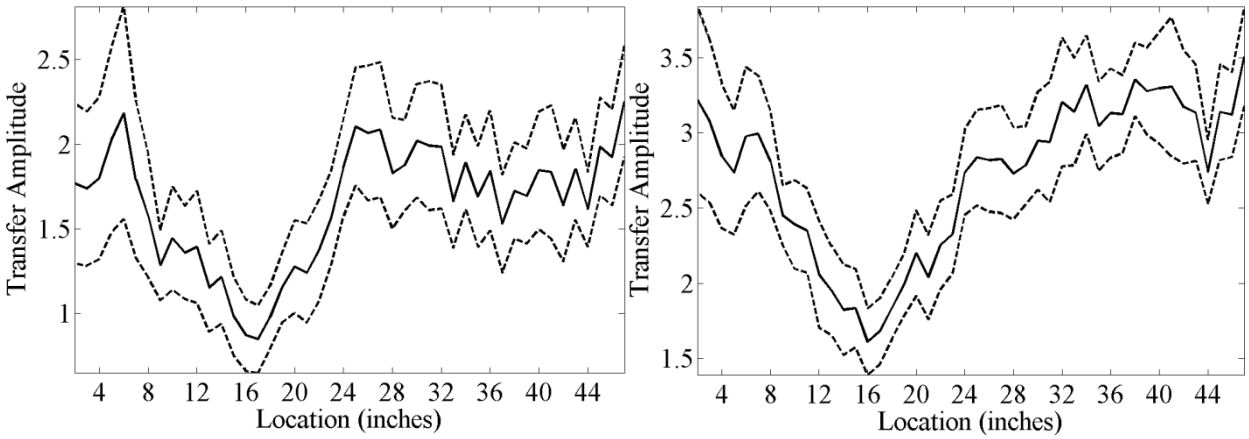

Figure 5-12. Smooth Narrowed Results of 10 Impact-Echo Scans of Sample S1 Processed Using Signal Shortening with (a) *SF* = ½ and (b) *SF* = ¼ (1 in. = 25 mm).

Figure 5-13 and Figure 5-14 show the mean and COV, respectively, of the data obtained from the same 10 scans after they are processed using windowing on the time-displacement signal with a window width of (a) 1000 μs, (b) 750 μs, (c) 500 μs, (d) 250 μs. Figure 5-13 shows that, as the window width is reduced and the earlier portions of the time-displacement signals are emphasized, the f_{bonded} content at approximately 27 kHz can be observed with increasing clarity. Figure 5-15 shows the smooth scan results narrowed to the frequency of reflection from the steel-concrete interface after the application of windowing with a window width of (a) 1000 μs, (b) 750 μs, (c) 500 μs, (d) 250 μs. As the window width becomes smaller, the reduction in the mean transfer amplitude in the interval containing the defect, 12 in. (305 mm) to 20 in. (508 mm), becomes more pronounced. At a window width of 250 μs shown in Figure 5-15d, the dip in the transfer amplitude is a clear indicator of the defect.

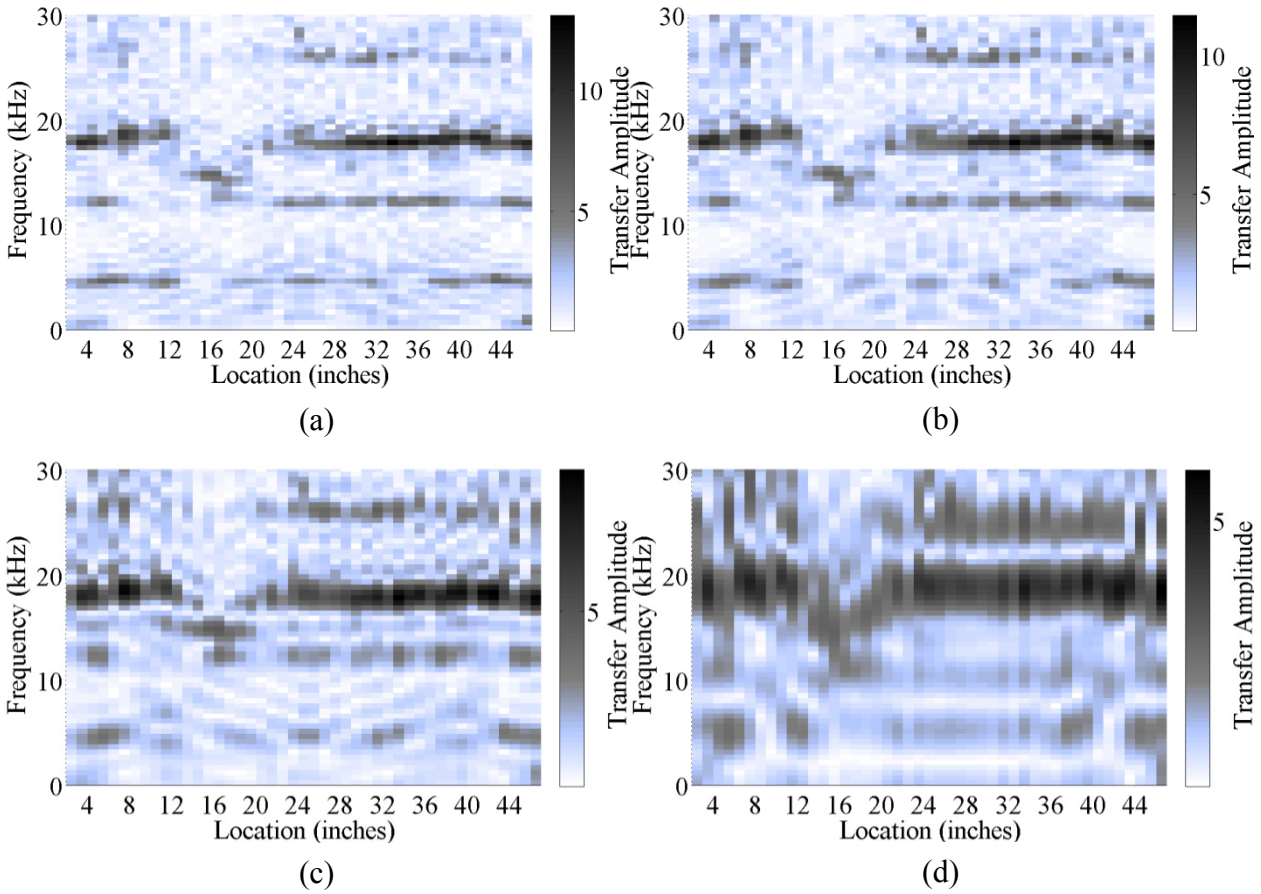

Figure 5-13. Mean Results of 10 Impact-Echo Scans of Sample S1 Processed Using Windowing with a Window Width of (a) 1000 µs, (b) 750 µs, (c) 500 µs, and (d) 250 µs (1 in. = 25 mm).

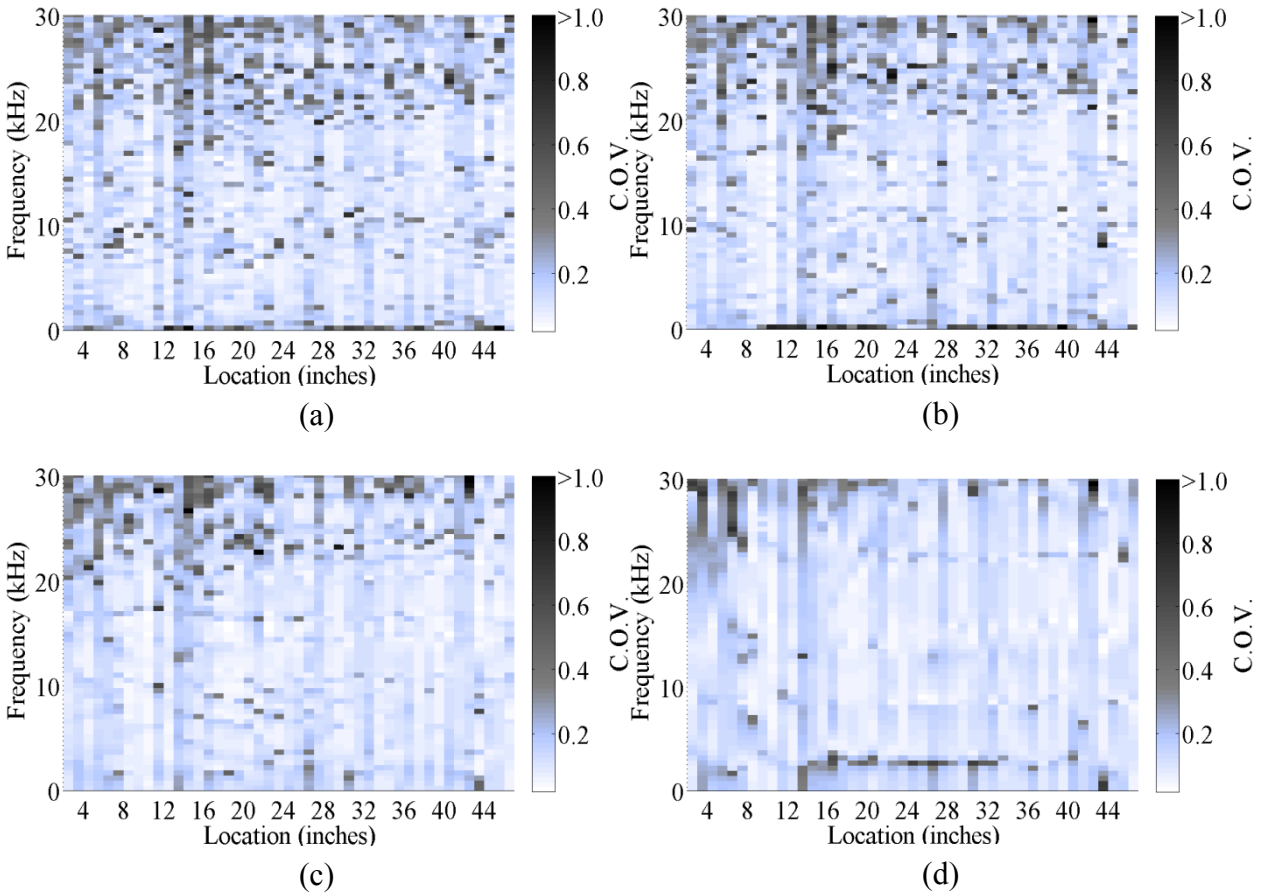

Figure 5-14. COV of 10 Impact-Echo Scans of Sample S1 Processed Using Windowing with a Window Width of (a) 1000 µs, (b) 750 µs, (c) 500 µs, and (d) 250 µs (1 in. = 25 mm).

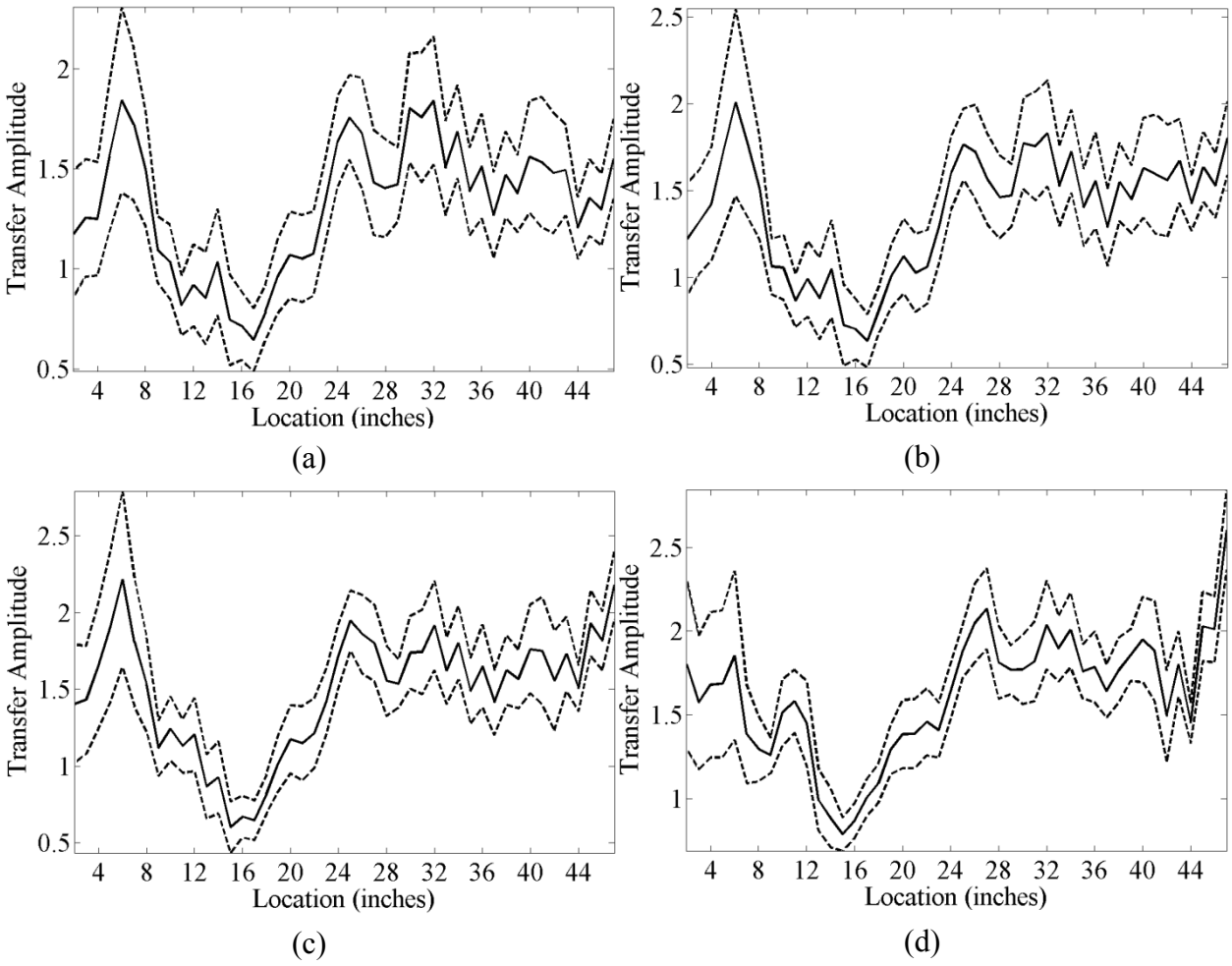

Figure 5-15. Smooth Narrowed Results of 10 Impact-Echo Scans of Sample S1 Processed Using Windowing with a Window Width of (a) 1000 µs, (b) 750 µs, (c) 500 µs, and (d) 250 µs (1 in. = 25 mm).

Figure 5-16 shows the mean results of the same 10 scan after the application of autocorrelation and (a) R-wave Removal, (b) Signal Shortening with SF = ½, (c) Windowing with a window width of 1000 µs, (d) 750 µs, (e) 500 µs, and (f) 250 µs. The f_{bonded} content is observable in all of these representations; however the application of autocorrelation and a windowing with window width of 250 µs shows this content with the most clarity. However, the content is not as evident in this representation when compared to the non-autocorrelated data shown in Figure 5-13d. Figure 5-17 shows the COVs corresponding to the means shown in Figure 5-16. A comparison of these values with their non-autocorrelated counterparts in Figure 5-8, Figure 5-11, and Figure 5-14 shows that there is an increase in variation with the application

of autocorrelation. Figure 5-18 shows the smooth scan results narrowed to the frequency of reflection from the steel-concrete interface after the application of autocorrelation and (a) R-wave Removal, (b) Signal Shortening with SF = ½, (c) Windowing with a window width of 1000 μs, (d) 750 μs, (e) 500 μs, and (f) 250 μs. The autocorrelated and windowed signal in Figure 5-18f shows the clearest indication of the defect, which is the drastic reduction in the transfer power on the interval containing the defect. Additionally, there is no significant difference between the confidences with which a defect is identified using Figure 5-18f when compared to Figure 5-15f.

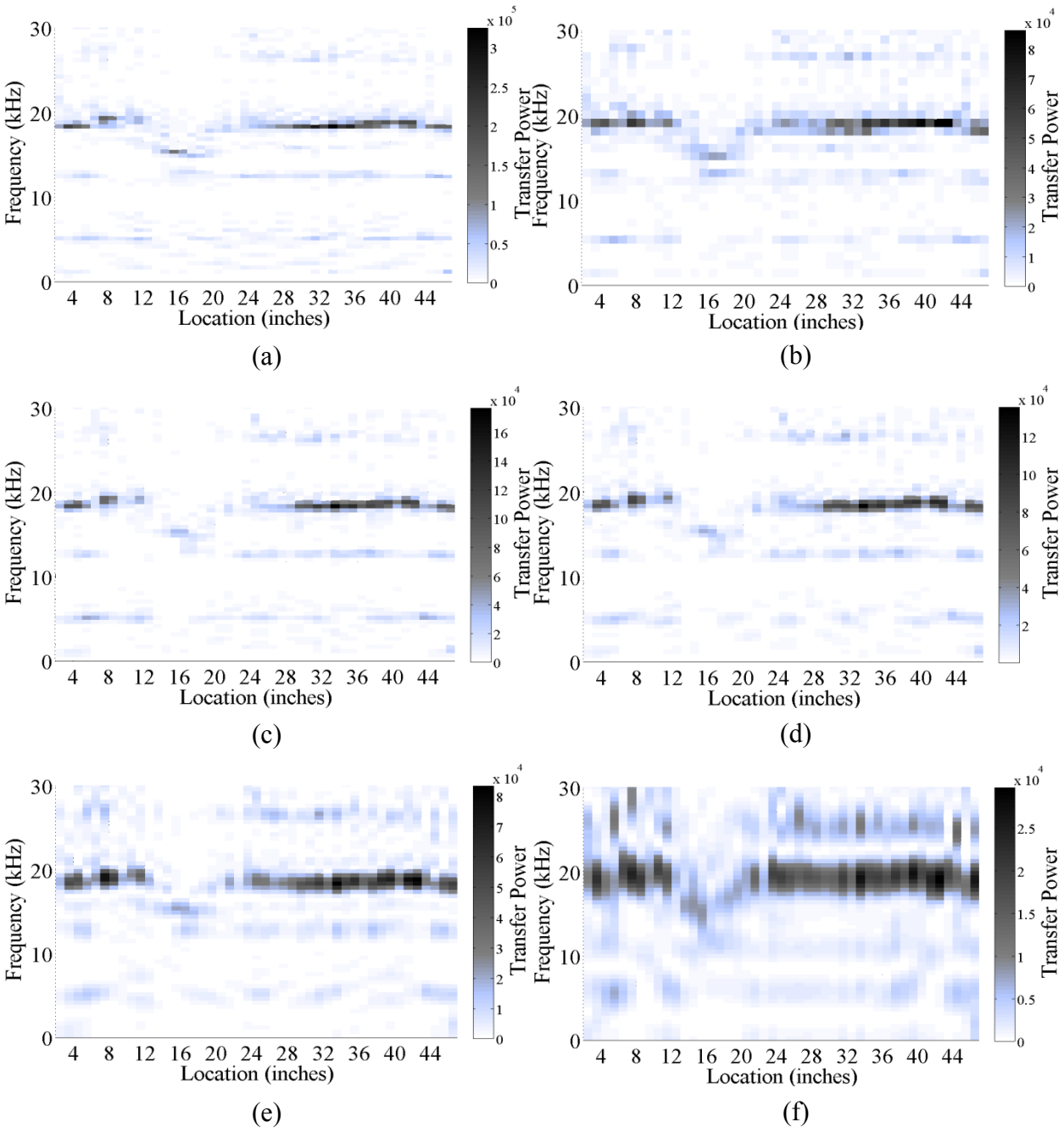

Figure 5-16. Mean Results of 10 Impact-Echo Scans of Sample S1 Processed Using Autocorrelation and (a) R-Wave Removal, (b) Signal Shortening with NF = ½, (c) Windowing with a Window width of 1000 µs, (d) 750 µs, (e) 500 µs, and (f) 250 µs (1 in. = 25 mm).

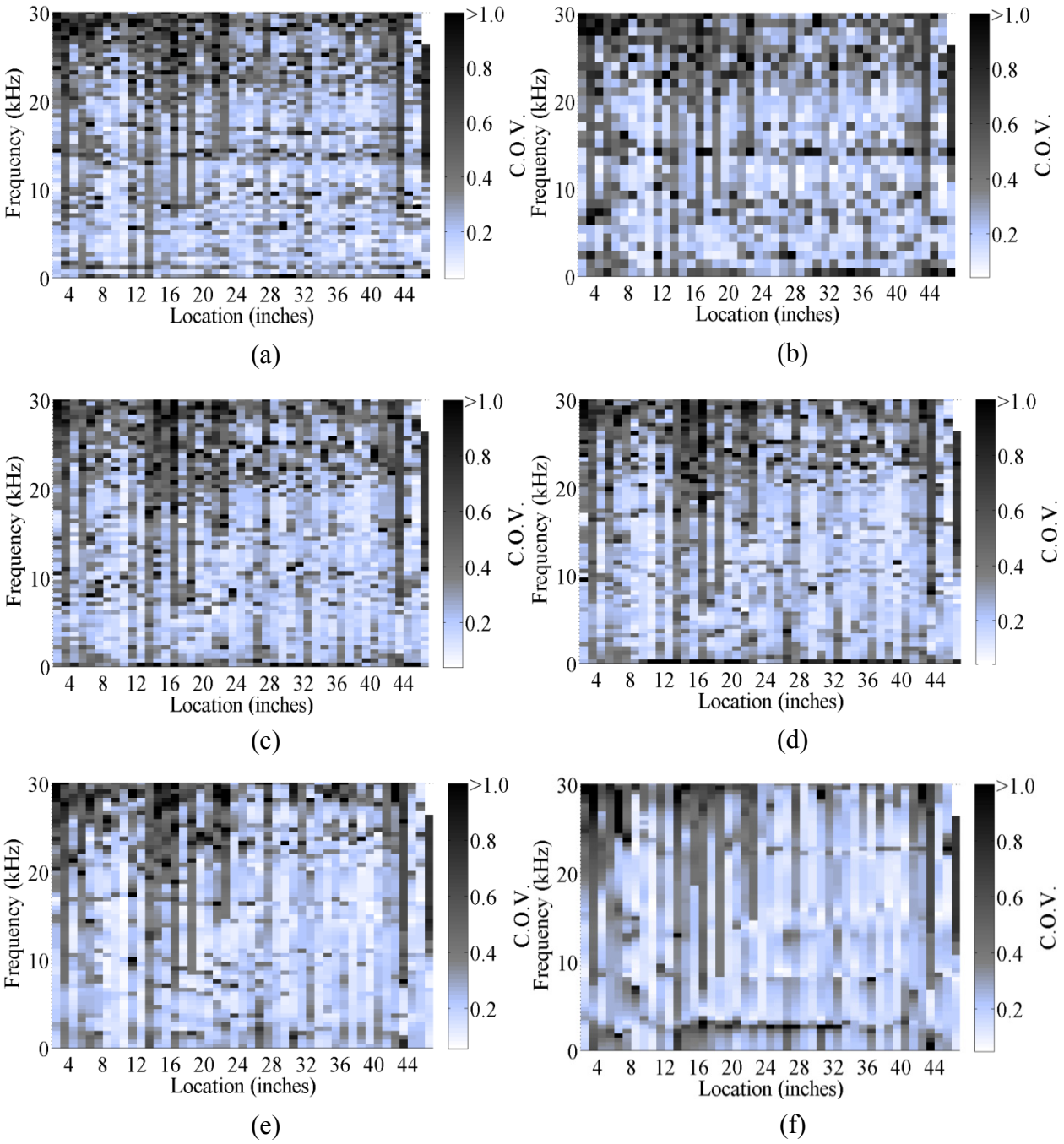

Figure 5-17. COV of 10 Impact-Echo Scans of Sample S1 Processed Using Autocorrelation and (a) R-Wave Removal, (b) Signal Shortening with NF = ½, (c) Windowing with a Window Width of 1000 µs, (d) 750 µs, (e) 500 µs, and (f) 250 µs (1 in. = 25 mm).

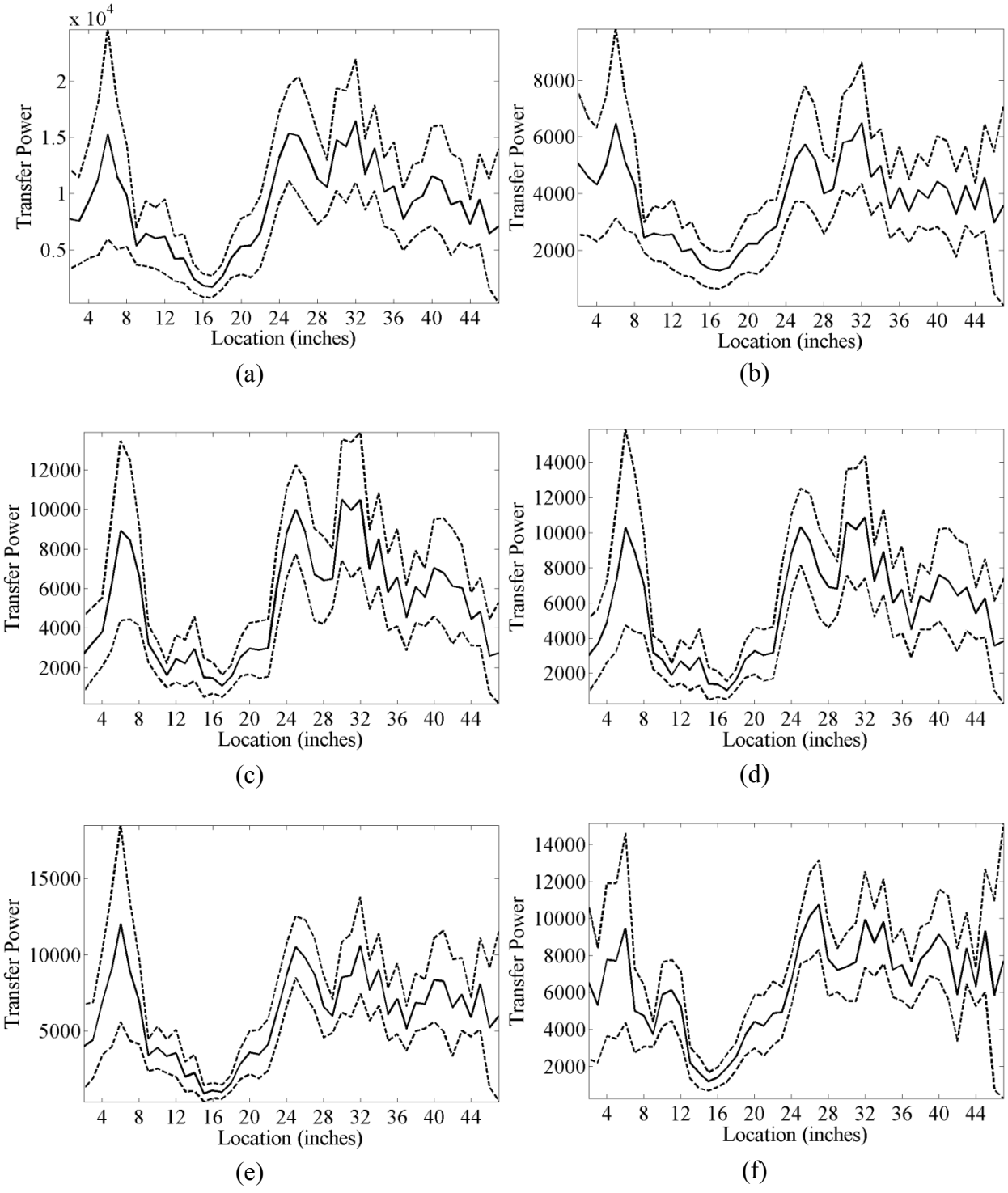

Figure 5-18. Smooth Narrowed Results of 10 Impact-Echo Scans of Sample S1 Processed Using Autocorrelation and (a) R-Wave Removal, (b) Signal Shortening with NF = ½, (c) Windowing with a Window Width of 1000 µs, (d) 750 µs, (e) 500 µs, and (f) 250 µs (1 in. = 25 mm).

Figure 5-19 shows the mean results of the same 10 scan after the application of bandwidth-weighted autocorrelation, and (a) R-wave Removal, (b) Signal Shortening with SF = ½, (c) Windowing with a window width of 1000 μs, (d) 750 μs, (e) 500 μs, and (f) 250 μs. The f_{bonded} content is observable in all of these representations; however the application of bandwidth-weighted autocorrelation and a windowing with window width of 250 μs shows this content with the most clarity. The content is not as evident in this representation when compared to the non-autocorrelated data shown in Figure 5-13d. Figure 5-20 shows the COVs corresponding to the means shown in Figure 5-19. A comparison of these values with their non-autocorrelated counterparts in Figure 5-8, Figure 5-11, and Figure 5-14 shows that there is an increase in variation with the application of bandwidth-weighted autocorrelation. Figure 5-21 shows the smooth scan results narrowed to the frequency of reflection from the steel-concrete interface after the application of bandwidth-weighted autocorrelation and (a) R-wave Removal, (b) Signal Shortening with SF = ½, (c) Windowing with a window width of 1000 μs, (d) 750 μs, (e) 500 μs, and (f) 250 μs. The bandwidth-weighted autocorrelated and windowed signal in Figure 5-21f shows the clearest indication of the void, which is the drastic reduction in the transfer power on the interval containing the defect. Additionally, there is no drastic difference between the confidences with which a defect is identified using Figure 5-21f when compared to Figure 5-15f.

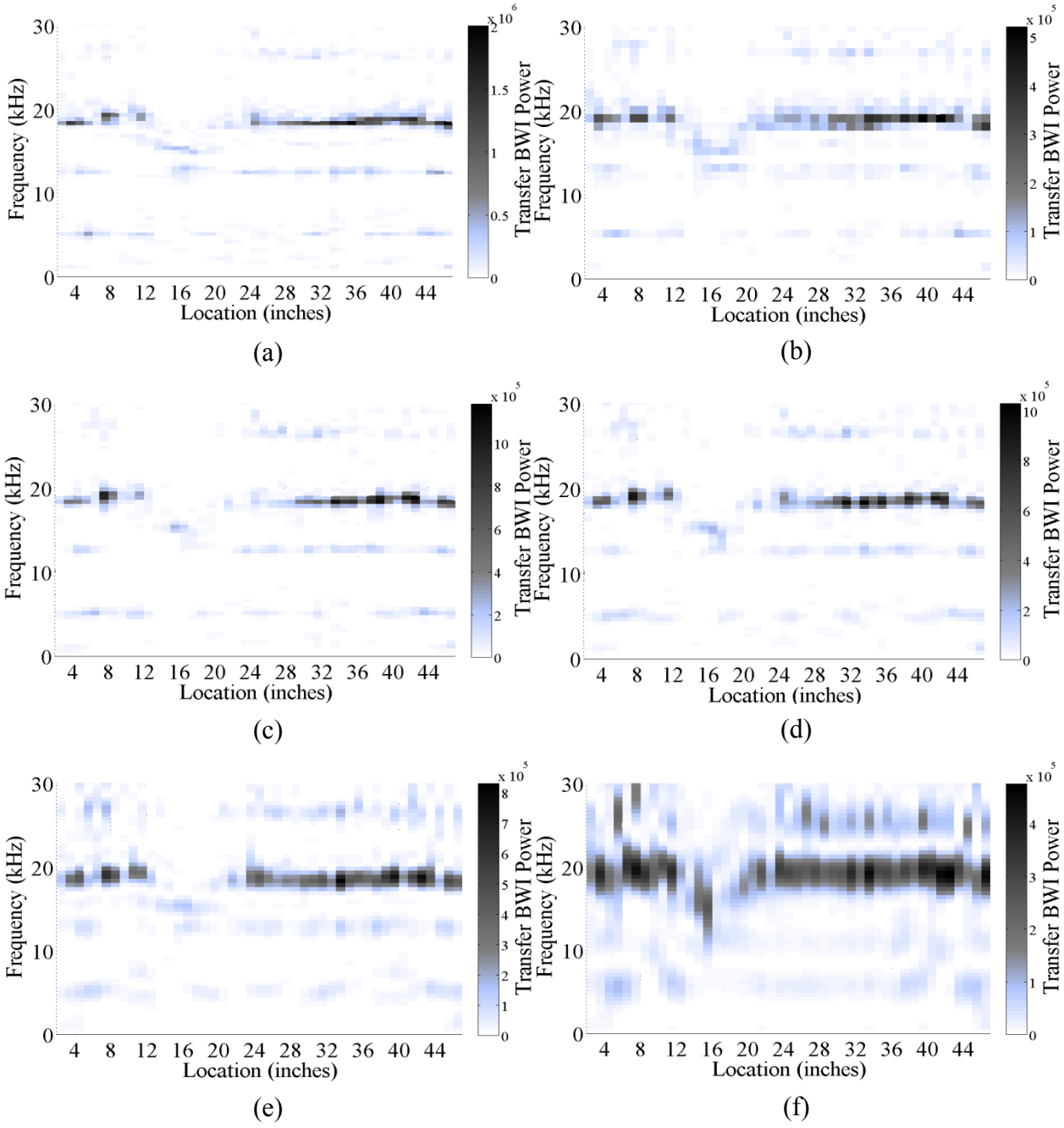

Figure 5-19. Mean Results of 10 Impact-Echo Scans of Sample S1 Processed Using Bandwidth-Weighted Autocorrelation and (a) R-Wave Removal, (b) Signal Shortening with NF = ½, (c) Windowing with a Window Width of 1000 µs, (d) 750 µs, (e) 500 µs, and (f) 250 µs (1 in. = 25 mm).

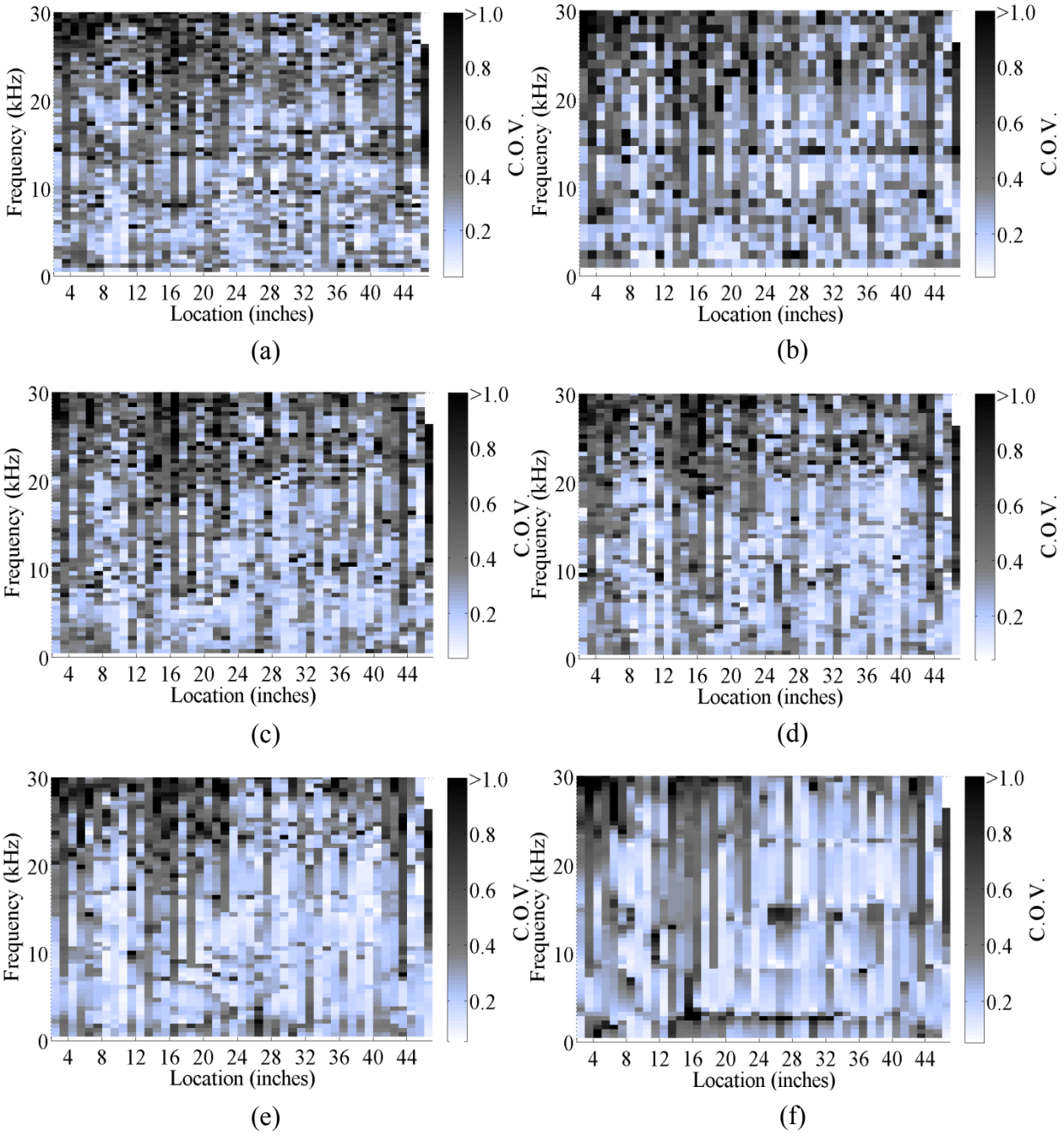

Figure 5-20. COV of 10 Impact-Echo Scans of Sample S1 Processed Using Bandwidth-Weighted Autocorrelation and (a) R-Wave Removal, (b) Signal Shortening with NF = ½, (c) Windowing with a Window Width of 1000 µs, (d) 750 µs, (e) 500 µs, and (f) 250 µs (1 in. = 25 mm).

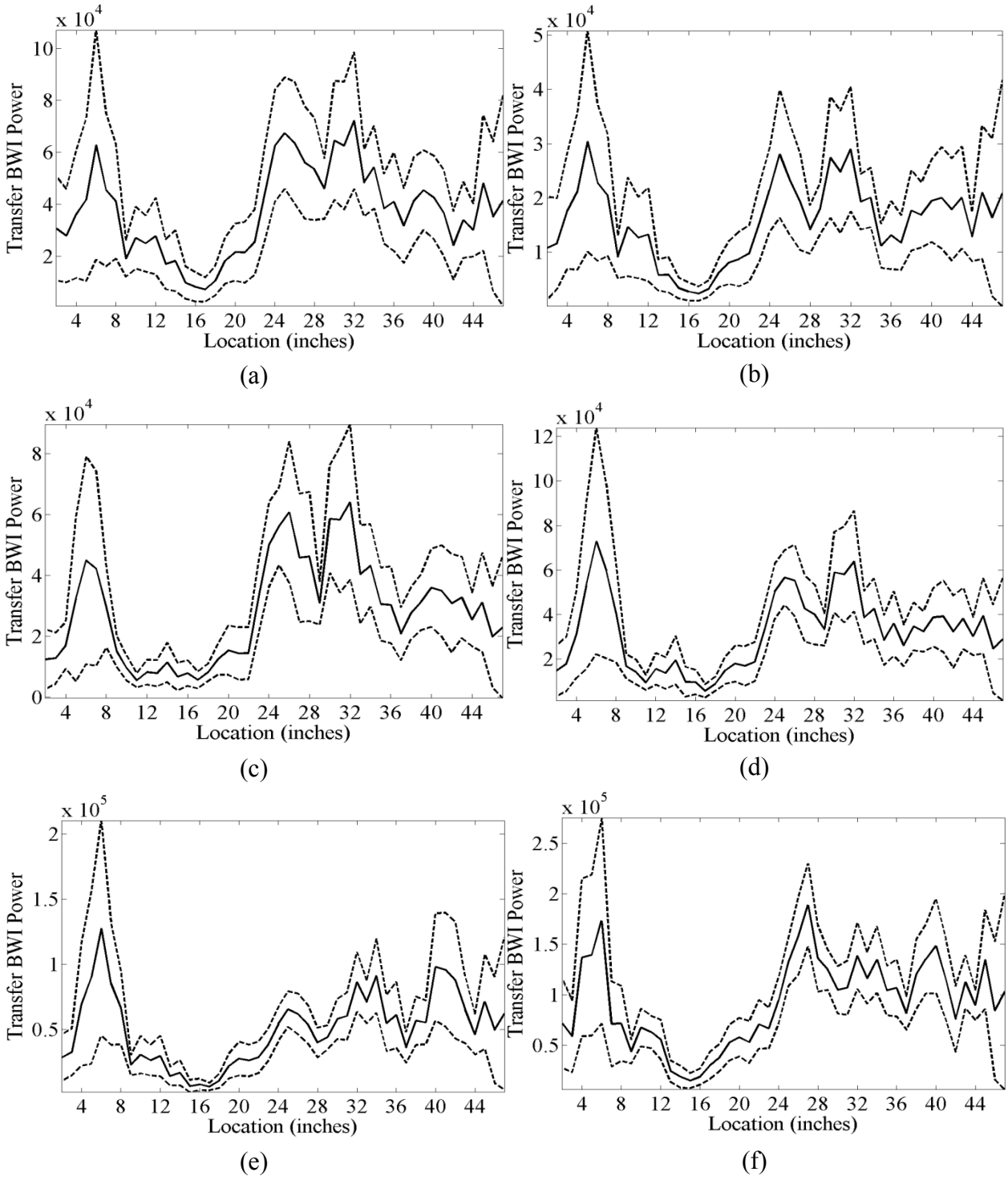

Figure 5-21. Smooth Narrowed Results of 10 Impact-Echo Scans of Sample S1 Processed Using Bandwidth-Weighted Autocorrelation and (a) R-Wave Removal, (b) Signal Shortening with NF = ½, (c) Windowing with a Window Width of 1000 µs, (d) 750 µs, (e) 500 µs, and (f) 250 µs (1 in. = 25 mm).

Examination of the results of the additional DSP confirms the concept that the signal-to-noise ratio for impact-echo signals is greater within the early portions of the signal, where the effects of divergence and attenuation are minimal. Through the application of signal shortening or windowing, emphasizing the early portions in the time domain increases the clarity with which the f_{bonded} content can be observed in the frequency domain. Both procedures attempt to correct for the same issues; however, the windowing procedure is slightly more favorable as it does not affect the numerical value of the frequency resolution, Δf. These techniques should be applied in a manner that eliminates the frequency content associated with the observation of the R-wave in the time-displacement signal. Based on the results of impact-echo testing on sample S1, additional manipulation of the signal using autocorrelation and the bandwidth procedure does not significantly improve the qualitative detection of a defect at the steel-concrete interface. The results of testing on the remaining samples are processed using a combination of R-wave removal and windowing with a window width of 250 μs. The results are narrowed to examine only the f_{bonded} content, and smoothed to allow for more confident defect identification using qualitative observation of the scan results.

5.3.3 Results

For direct comparison, examination of samples S1, S2, and S3 is done to explore the effect of defect length L_d on the confidence with which a defect may be qualitatively detected. Figure 5-22 shows the smooth narrowed scan results from samples (a) S1 (L_d = 8 in.), (b) S2 (L_d = 4 in.) and (c) S3 (L_d = 2 in.). As previously observed, there is a pronounced amplitude reduction in the scan results from sample S1 at the true location of the 8 in. (203 mm) defect between 12 in. (305 mm) and 20 in. (508 mm). In the scan results of sample S2, the minimum value of the sample mean amplitude does not occur within the interval containing the 4 in. (102 mm) defect from 12 in. (305 mm) to 16 in. (406 mm). This inconsistency will be discussed later. However, the scan of sample S3 does show an accurate indication of the 2 in. (51 mm) defect in the sharp reduction of in the transfer amplitude at 14 in. (356 mm), which is within the interval containing the defect from 12 in. (305 mm) 14 in. (356 mm).

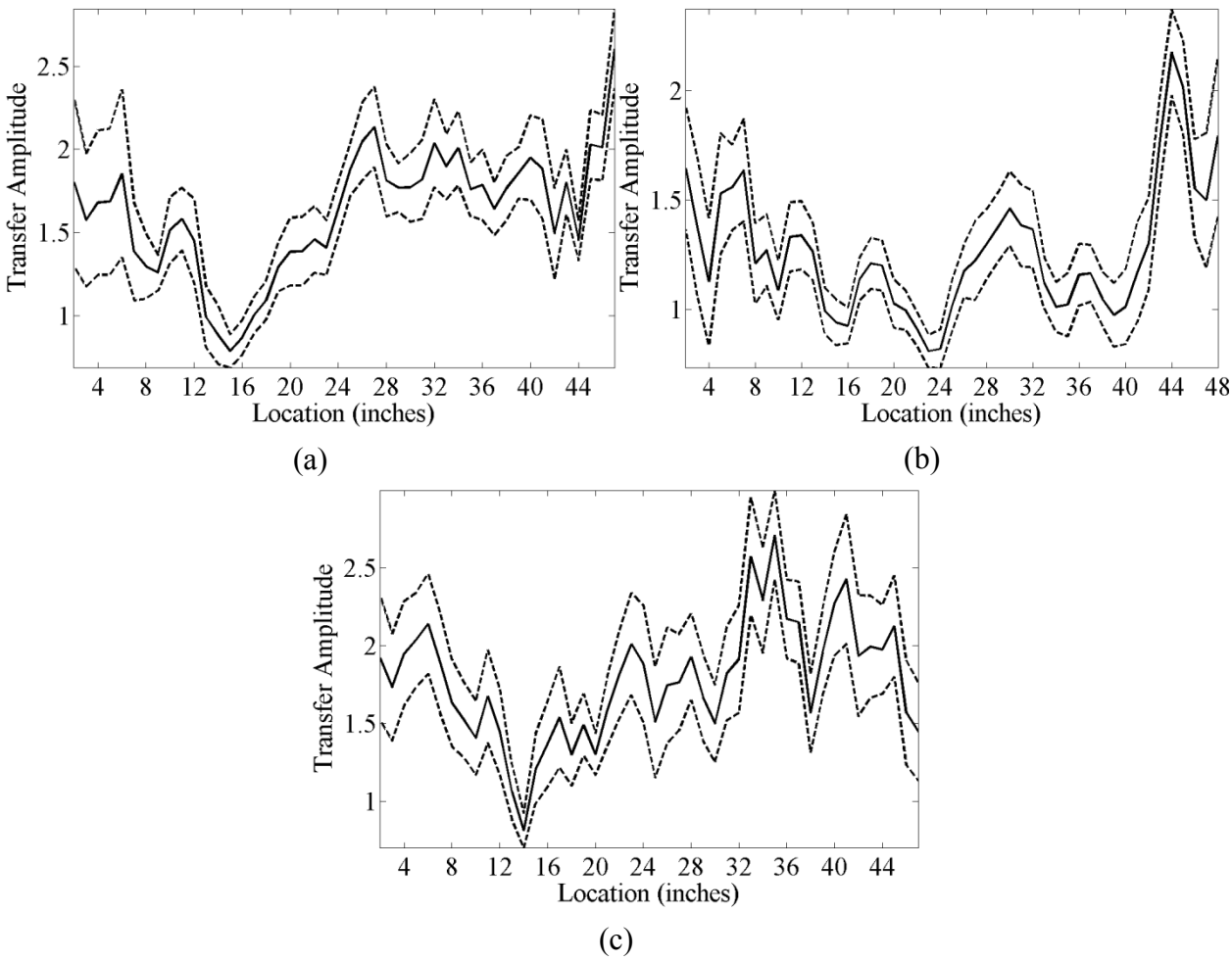

Figure 5-22. Scan Results from Samples (a) S1 (L_d = 8 in. [203 mm]), (b) S2 (L_d = 4 in. [102 mm]), and (c) S3 (L_d = 2 in. [51 mm]) (1 in. = 25 mm).

There is a clear inconsistency in the scan results of samples S2 and S3. If there is no accurate indication of the 4 in. (102 mm) in sample S2, than it should be expected that a shorter defect would also not be accurately indicated. This is not case with the 2 in. (51 mm) defect in the results from sample S3. To investigate this inconsistency, it is noted in Figure 5-22b that dips in the transfer amplitude occur between 20 in. (508 mm) and 24 in. (610 mm), and 32 in. (813 mm) and 42 in. (1067 mm). The dip between 14 in. (305 mm) and 16 in. (406 mm) is within the planed defect location, however it should be considered that the other two pronounced dips are possibly the result of unplanned defects at the steel-concrete interface. Unplanned defects may occur as a result of insufficient consolidation during sample construction. Assessing this

hypothesis can be done by examining the f_{D1} content in the non-narrowed frequency scan results. Figure 5-23 shows the scan results from sample S2 after R-wave removal. At the location of the defect, the f_{D1} content shifts from approximately 18 kHz to approximately 15 kHz. A similar shift does not occur in the test data at any other location, indicating that there are no unplanned defects at any other location that are of sufficient dimension to cause an indicator in the f_{D1} content. This implies that defect length and defect thickness can have different effects on contents generated at different frequencies. In any case, unplanned defects cannot be ruled out as a reason for the poor indication of the defect in the scan data from sample S2.

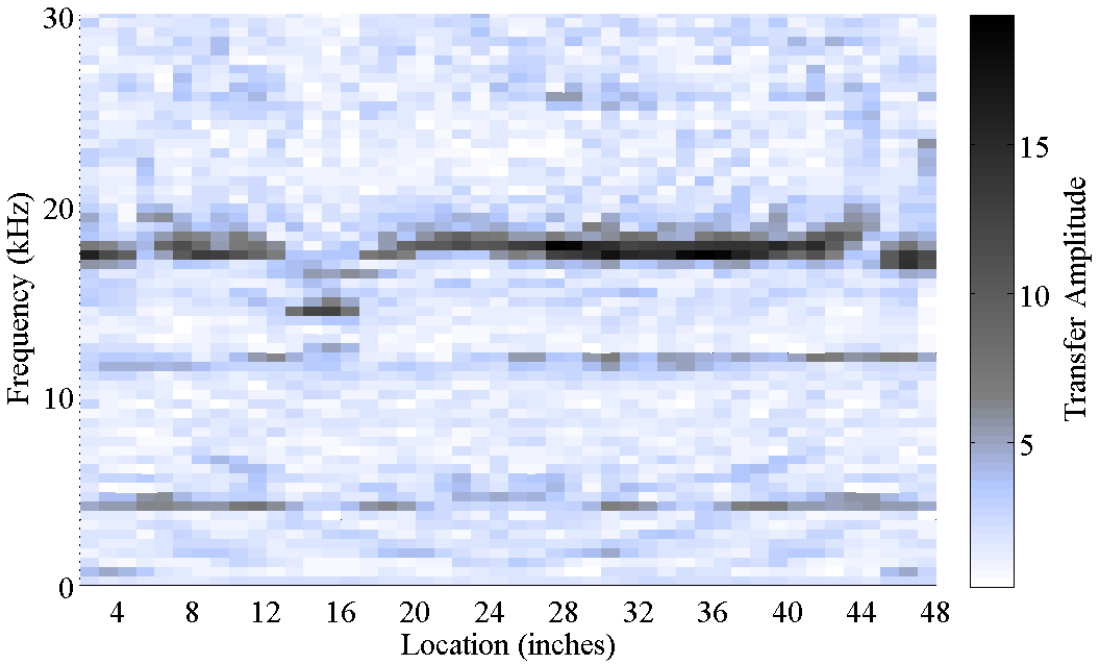

Figure 5-23. Scan Results of Sample S2 after R-Wave Removal (1 in. = 25 mm).

Examination of Samples S1, S4, and S5 is done to explore the effect of defect thickness T_d on the confidence with which a defect may be qualitatively detected. Figure 5-24 shows the smooth narrowed scan results from samples (a) S1 (T_d = 0.010 in. [0.25 mm]), (b) S4 (T_d = 0.008 in. [0.20 mm]) and (c) S5 (T_d = 0.005 in. [0.13 mm]). The absolute minima in each of the scan results occur within the interval containing the defect from 12 in. (305 mm) to 20 in. (508 mm). This indicates that defects on single bars that are 8 in. (203 mm) in length and longer are detectable when the defect thickness is as small as 0.005 in. (0.13 mm).

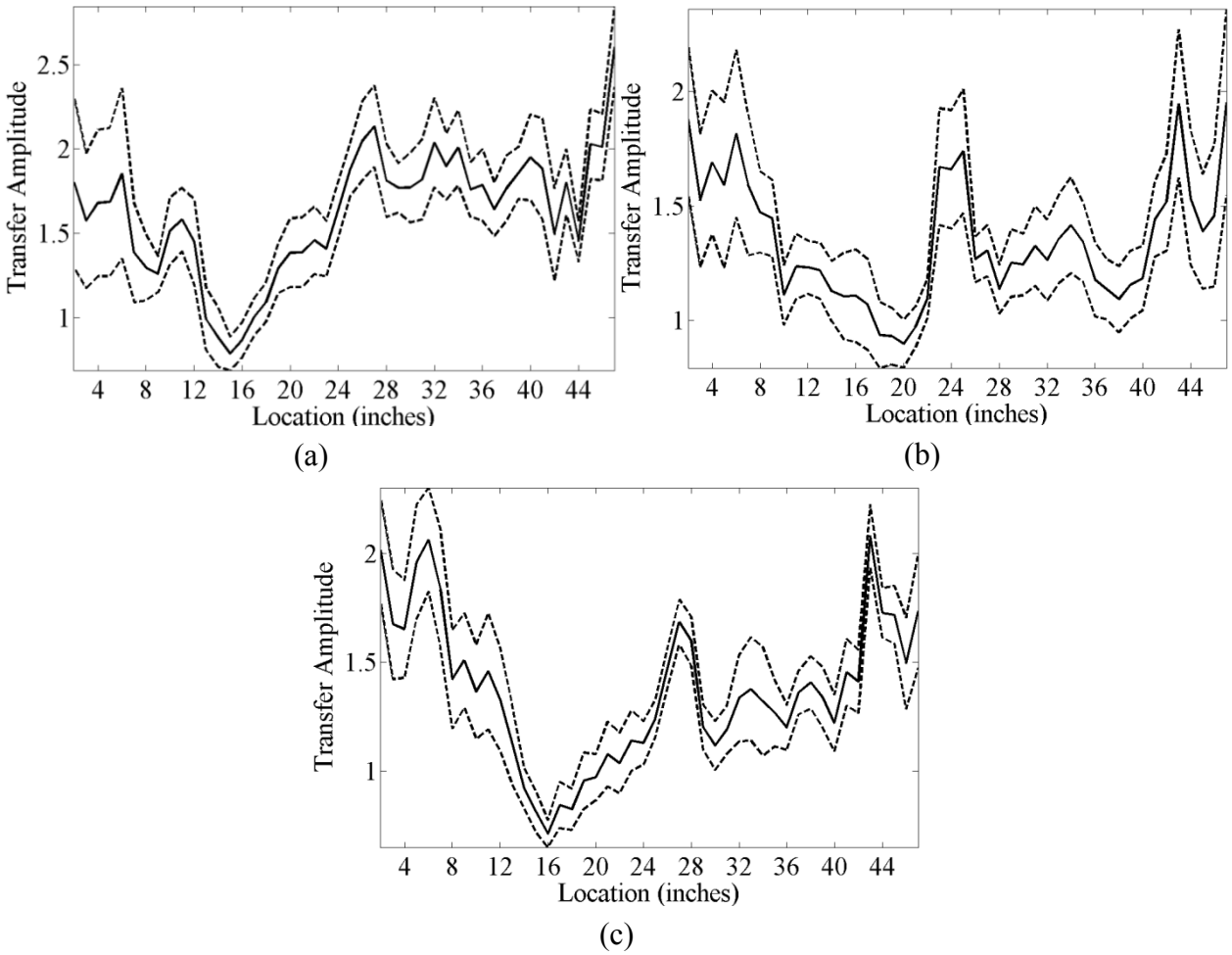

Figure 5-24. Scan Results from Samples (a) S1 (T_d = 0.010 in. [0.25 mm]), (b) S4 (T_d = 0.008 in. [0.20 mm]), and (c) S5 (T_d = 0.005 in. [0.13 mm]) (1 in. = 25 mm).

As previously stated, examining the f_{D1} content to detect the location of a defect is likely not reliable in field structures affected by ASR/DEF. However, we may examine the f_{D1} content in the scan results of sample S1, S4, and S5 in an attempt to determine the effects of defect thickness on this content. This may aid in addressing the previously discussed inconsistency in the scan results from sample S2. Figure 5-25 shows the scan results after the application of R-wave removal from samples (a) S1 (T_d = 0.010 in. [0.25 mm]), (b) S4 (T_d = 0.008 in. [0.20 mm]) and (c) S5 (T_d = 0.005 in. [0.13 mm]). In the results from all three samples, a similar shift of the f_{D1} content is observed within the interval containing the defect from 12 in. (305 mm) and 20 in. (508 mm). This result indicates that 8 in. (203 mm) defects at the steel-concrete interface on single bars can cause a shift in the f_{D1} content at values of T_d as small as 0.005 in. (0.13 mm).

Additionally, the possible unplanned defects in sample S2 would be less than 0.005 in. (0.13 mm) in thickness.

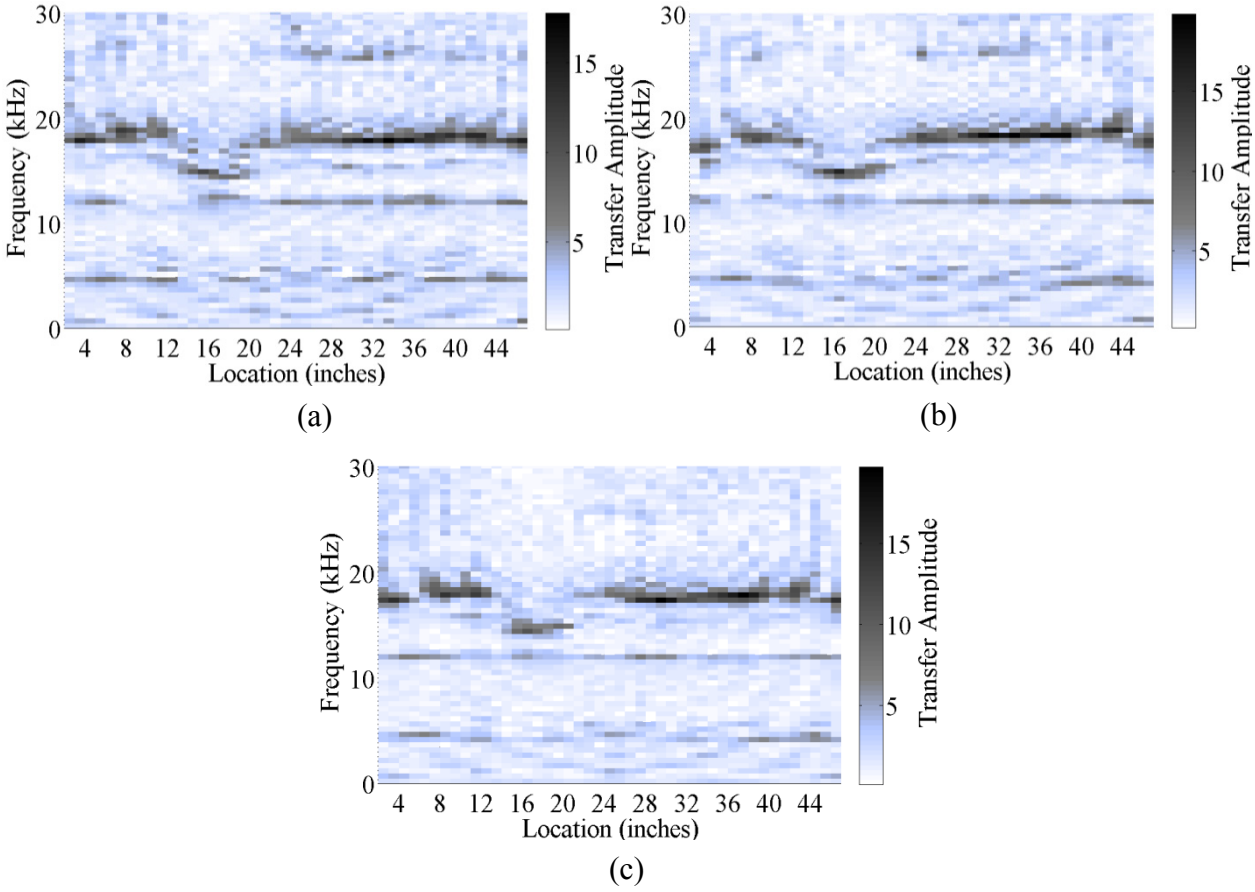

Figure 5-25. Scan Results after R-Wave Removal for Samples (a) S1 (T_d = 0.010 in.), (b) S4 (T_d = 0.008 in.), and (c) S5 (T_d = 0.005 in.) (1 in. = 25 mm).

Examination of Samples S1 and D1 is done to explore the effect of adjacent reinforcing bars on the confidence with which a defect can be qualitatively detected. Figure 5-26 shows the smooth narrowed scan results from samples (a) S1 and (b) D1. The indication of the defect in the scan results from sample D1 is only mildly less prevalent than that from sample S1. Examination of samples S2, S3, D2, and D3 is done to further explore the effects of adjacent reinforcing bars and defect length L_d on the confidence with which a defect may be qualitatively detected. Figure 5-27 shows the smooth narrowed scan results from samples (a) S2 (L_d = 4 in. [102 mm]), (b) S3 (L_d = 2 in. [51 mm]), (c) D2 (L_d = 4 in. [102 mm]), and (d) D3 (L_d = 2 in. [51 mm]). The scan results from samples D2 and D3 show no indication of the defect in the narrowed results. Comparison of the results from samples S2 and D2 is challenging due to the

questions regarding unplanned defects in sample S2. A comparison of samples S3 and D3 shows that the placement of adjacent steel impedes the detection of defects with an L_d of 2 in. (51 mm) and a T_d of 0.010 in. (0.25 mm).

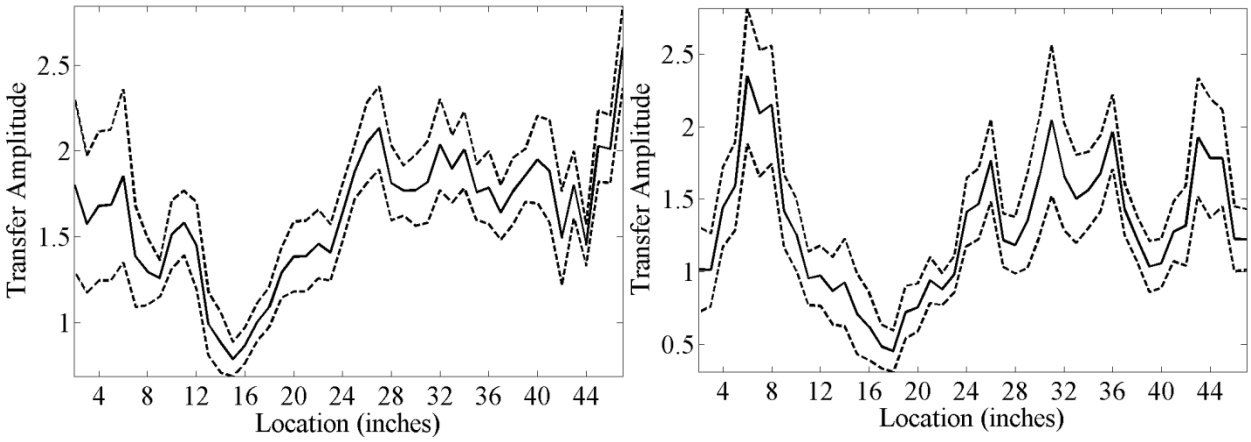

Figure 5-26. Scan Results from Sample (a) S1 and (b) D1 (1 in. = 25 mm).

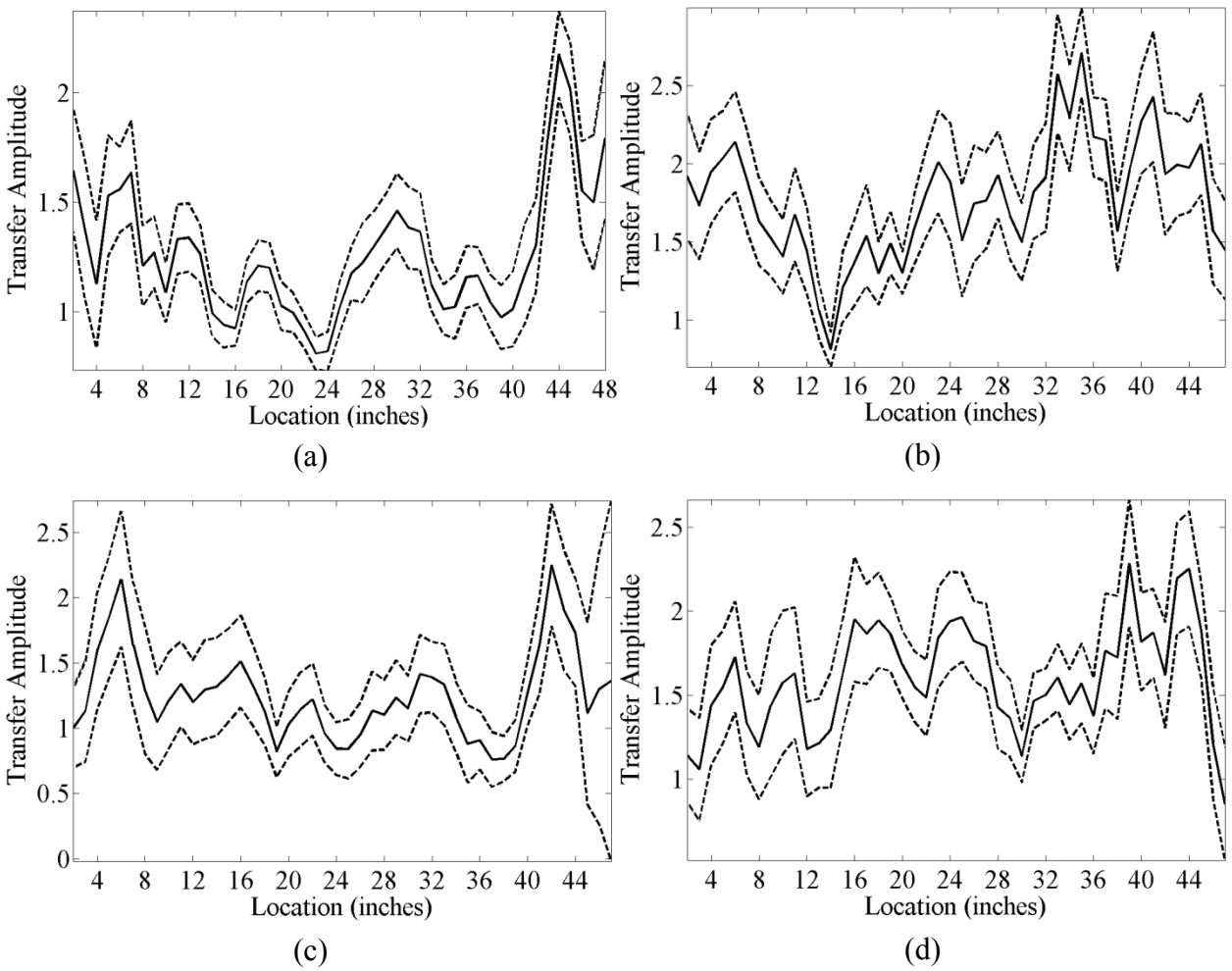

Figure 5-27. Scan Results from Samples (a) S2 (L_d = 4 in.), (b) S3 (L_d = 2 in.), (c) D2 (L_d = 4 in.), and (d) D3 (L_d = 2 in.) (1 in. = 25 mm).

Examination of samples S4, S5, D4, and D5 is done to further explore the effects of adjacent reinforcing bars and defect thickness T_d on the confidence with which a defect may be qualitatively detected. Figure 5-28 shows the smoothed scan results from samples (a) S4 (T_d = 0.008 in. [0.20 mm]), (b) S5 (T_d = 0.005 in. [0.13 mm]), (c) D4 (T_d = 0.007 in. [0.18 mm]), and (d) D5 (T_d = 0.005 in. [0.13 mm]). The scan results from sample D4 show a dip in the mean transfer amplitude along the interval containing the defect from 12 in. (305 mm) to 20 in. (508 mm). In the same set of results, relatively low values of the mean transfer amplitude are observed between 1 in. (25 mm) and 5 in. (127 mm). The f_{D1} content is again examined to determine if this result in the f_{bonded} content is the result of an unplanned defect at the steel concrete interface. Figure 5-29 shows the sample mean of the scan results for sample D4 after the application of R-wave removal. In this case, the f_{D1} content appears at a lower frequency

between 1 in. (25 mm) and 5 in. (127 mm) when compared with the locations without planned defects. This result indicates that an unplanned defect is likely causing the relatively low values of the mean transfer amplitude between 1 in. (25 mm) and 5 in. (127 mm) in the narrowed response. Returning to the results shown in Figure 5-28, the scan results from sample D5 do not show a single indicator of the defect between 12 in. (305 mm) and 20 in. (508 mm). Instead, two distinct dips in the mean transfer amplitude are observed at 12 in. (305 mm) and 20 in. (508 mm). The comparison of the results from samples S4 and D4 shows little to no change in confidence with which the defect location can be identified in the presence of an adjacent steel reinforcing bars. However, the comparison of the results from S5 and D5 shows that the presence of adjacent steel reinforcing bars likely influences the confidence with which a defect is located when the void has a length of 8 in. (203 mm) or less and a thickness of 0.005 in. (0.13 mm) or less.

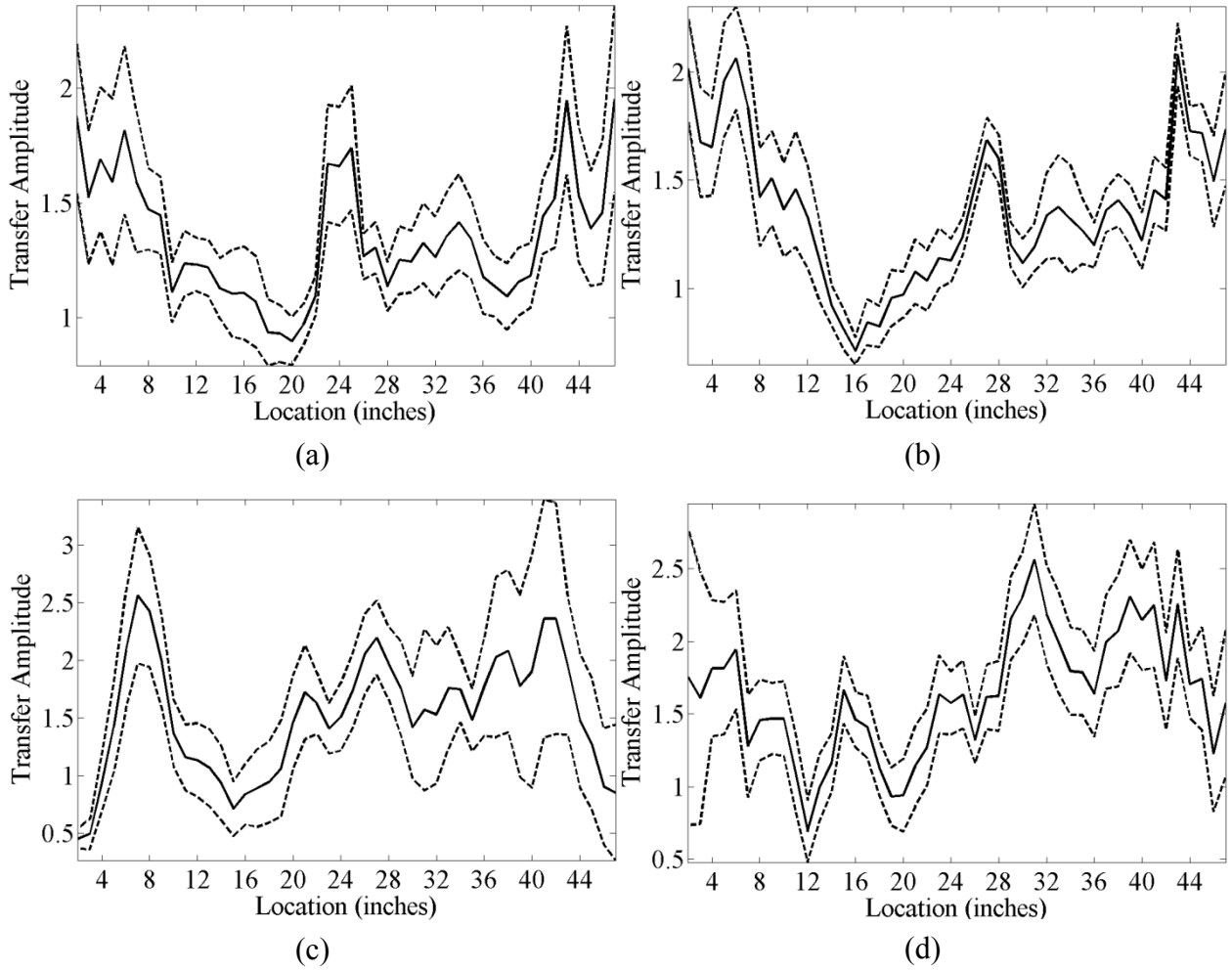

Figure 5-28. Scan Results from Samples (a) S4 (T_d = 0.008 in.), (b) S5 (T_d = 0.005 in.), (c) D4 (T_d = 0.007 in.), and (d) D5 (T_d = 0.005 in.) (1 in. = 25 mm).

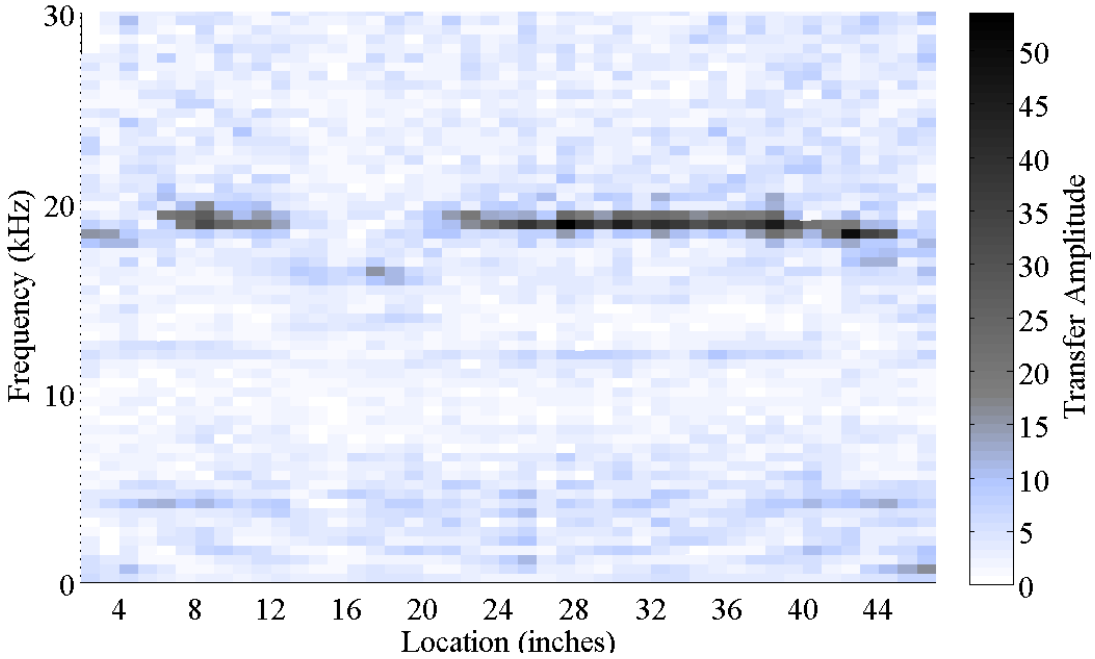

Figure 5-29. Scan Results of Sample D4 after R-Wave Removal (1 in. = 25 mm).

5.4 SUMMARY

To establish a baseline for the limitations of impact-echo in assessing the state of the steel-concrete interface in ASR/DEF affected structures, a set of small-scale RC samples are examined using a commercially available point-test impact-echo system. Examination of data from these samples aides the process of determining appropriate procedural details such as test set-up, scanning parameters, digital sampling configuration, and appropriate signal processing. Ten samples are examined in this study. The samples are rectangular prisms containing either one or two reinforcing bars placed at a cover depth of 2 in. (51 mm). A defect at the steel-concrete interface is created on one bar in each of the samples. The defect consists of multiple coats of spray-on rubber applied over a length varying from 2 in. (51 mm) to 8 in. (203 mm) with a radial thickness varying from 0.005 in. (0.13 mm) to 0.011 in. (0.28 mm).

One sample is examined using Fourier transform-based signal processing, and the results are narrowed to frequencies that are likely to translate well from small- to large-scale testing. Additional signal processing methods are applied individually and in appropriate combinations to determine the optimal approach for extracting the desired information from impact-echo signals. The application of R-wave removal and windowing is the combination of the least number of techniques that produces clear indication of the defect in the scan results within the

range of frequencies associated with P-wave reflections from the steel-concrete interface. Additional techniques such as autocorrelation and the bandwidth procedure may be applied, but do not create a noticeable change in the defect indication.

Examination of the remaining samples is carried out to determine the effects of length and radial thickness on the confidence with which a defect may be identified. With regards to the detectable defect length in samples containing one reinforcing bar, defects as short as 2 in. (51 mm) with a radial thickness of 0.01 in. (0.25) can be observed in the scan results; however, there may be unplanned defects in the sample containing the 4 in. (102 mm)-defect, making these results difficult to confirm. Defects that are 8 in. (203 mm) in length may be observed in samples containing a single bar at a radial thickness as small as 0.005 in. (0.13 mm), and possibly smaller. The placement of an adjacent reinforcing bar does not affect the confidence of detection of a defect that is 8 in. (203 mm) in length and 0.010 in. (0.25 mm) in radial thickness; however, when the defect length is reduced to 4 in. (102 mm) while holding the value of the radial thickness, the defect may no longer be confidently detected. If the defect length is held to 8 in. (203 mm), defects with radial thickness greater than or equal to 0.007 in. (0.18 mm) may be confidently detected in the presence of well-bonded adjacent steel reinforcement.

6 APPLICATION OF IMPACT-ECHO TO LARGE SCALE SAMPLES WITH ASR

6.1 INTRODUCTION

The samples that are assessed in Chapter 5 represent simplified models of a complex deterioration process. Field structures with real ASR and DEF may contain additional obstacles to accurately assess the steel-concrete interface using impact-echo. These challenges may include surface map cracking, internal defects with inconsistent geometries, and other consequences specific to the size, material properties, or deterioration mechanisms of ASR and/or DEF. To begin identifying and overcoming these obstacles, some of the large-scale samples discussed in Chapter 2 are examined using impact-echo.

Ideally, a complete assessment of each large-scale sample would be made immediately prior to the respective load test so that the results of impact-echo testing could be correlated with the force displacement results; however, the time-sensitive nature of the load testing did not allow for ideal impact-echo data collection within the duration of this project. Impact-echo testing was performed on large-scale samples. Data from the testing will be classified into three distinct sets. Samples C7 and C8 were examined using impact-echo prior to their destructive testing in summer 2011. Though the timing of this examination was close to the testing date, the accelerated schedule of Project 0-5722 required that this assessment be completed prior to establishing the procedure presented and used to examine the small-scale samples in Chapter 5. Thus, the procedure was not well-established when this testing was performed. C1-C6 were load tested prior to the identification of impact-echo as a candidate test method. Unfortunately, no other load testing was performed during the remaining duration of Project 0-6491, and thus, no correlation between impact-echo results and structural performance can be determined at this time. Though the timing of testing was not ideal, a limited assessment was performed on one large-scale specimen scheduled for future load testing (C9). Additionally, one specimen that had already undergone load testing (C6) was examined at locations with minimal damage approximately 2 years after load testing. The results of these three examinations (C7 and C8, C9, and C6) are presented next.

6.2 DATA COLLECTED FROM C7 AND C8 (IMMEDIATELY PRIOR TO LOAD TESTING)

Samples C7 and C8 were examined using impact-echo scanning immediately preceding their load testing in July 2011. The locations on each sample for impact-echo testing were selected based on several contributing factors. Due to the orientation of the specimens prior to load testing, access to certain surfaces was limited. Additionally, the face where concrete finished by hand during the casting process is typically too rough to record the impact-echo response. This challenge may be overcome with the use of a concrete surface grinder to reduce the roughness of the surface, but this option was not employed here due to concerns regarding the effects of this practice on the experimental program of Project 0-5722. This should not be an issue with field structures, as most column surfaces have smooth finishes as a result of casting against formwork. To examine the steel-concrete interface using impact-echo, test locations should be directly above the reinforcing bar. For the purpose of this experiment, construction drawings were used to determine the location of reinforcing bars. Tests were carried out within the lap-splice regions of the specimens. Figure 6-1 shows sample C7 at the time of the impact-echo assessment.

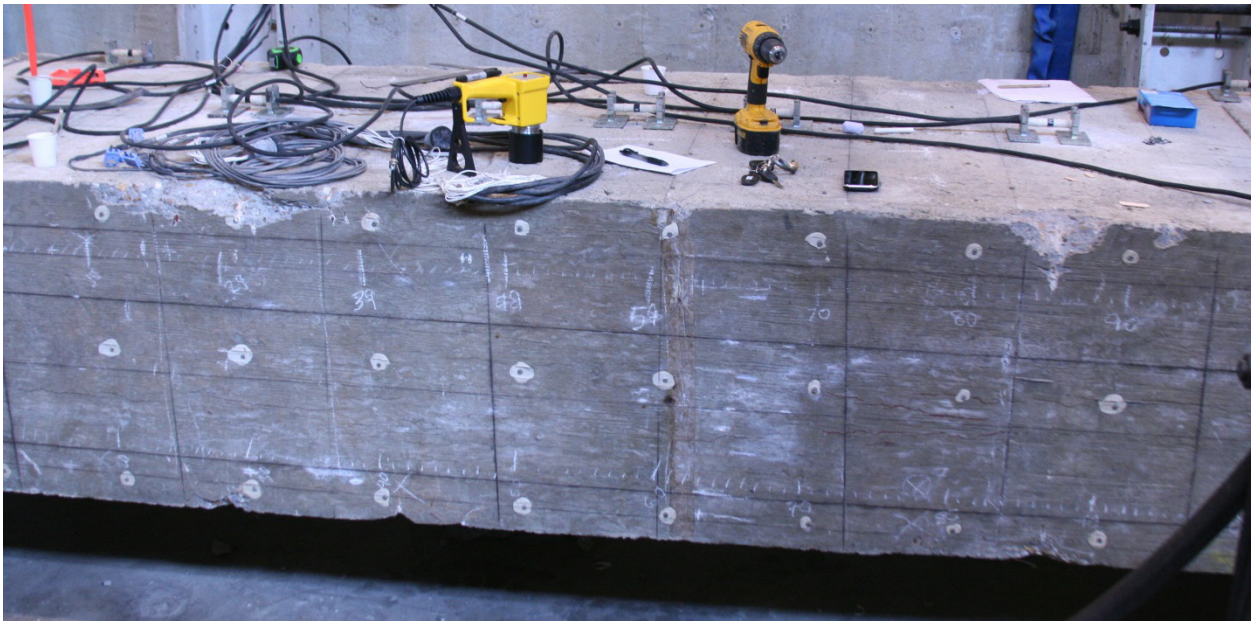

Figure 6-1. Large-Scale Samples C5 at the Time of Impact-Echo Testing (1 in. = 25 mm).

Figure 6-2 shows the locations for impact-echo testing on sample C7 (A, B, C, and D). At the time of testing, sample C7 was located in the testing apparatus with the hand-finished, rough surface facing up. This orientation did not allow for testing on either of the 48 in.

(1219 mm) by 300 in. (7620 mm) faces. Impact-echo testing was performed on the 24 in. (610 mm) by 300 in. (7620 mm) faces, as shown in Figure 6-2. Figure 6-3 shows the cross-sectional impact-echo testing locations for sample C8. While C7 was being load tested, C8 was stored with one of the 24 in. (610 mm) by 300 in. (7620 mm) faces resting on wooden blocks. This allowed for testing on the 48 in. (1219 mm) by 300 in. (7620 mm) face at locations E and F. After sample C8 was moved to the testing apparatus, the testing schedule of Project 0-5722 only allowed for testing at location C and D, as shown.

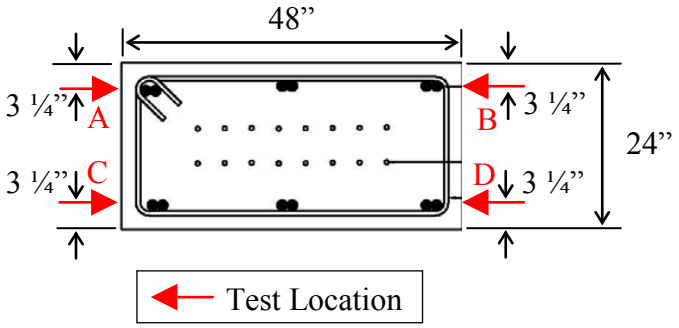

Figure 6-2. Impact-Echo Test Locations on the Cross Section of C7 within the Lap-Splice Region (1 in. = 25 mm).

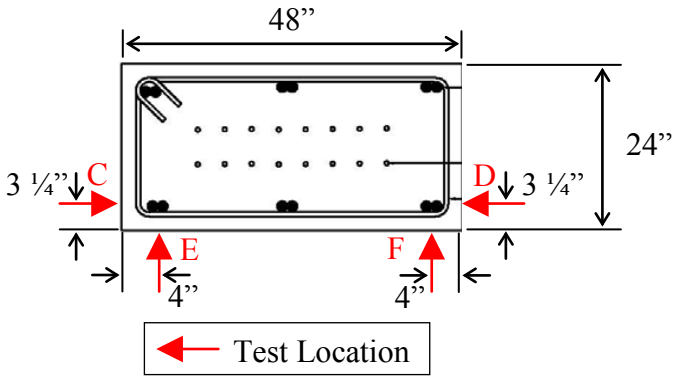

Figure 6-3. Impact-Echo Test Locations on the Cross Section of C8 within the Lap-Splice Region (1 in. = 25 mm).

Impact-echo requires a sufficiently smooth surface to produce accurate results. Though most of the surfaces of the sample are sufficiently smooth, surface irregularities exist within the testing lengths that obstruct impact-echo testing. Figure 6-4 shows examples of these surface irregularities. Some of these irregularities can be removed through the use of a concrete surface grinder, such as the irregularities shown in Figure 6-4a, Figure 6-4b, and Figure 6-4c. However, as previously stated, surface grinding was not an option in these experiments due to the potential changes in ASR or DEF damage. Figure 6-4d shows one of the demountable mechanical (DEMEC) measurement points located on the surface of all of the large-scale samples. These

points are located on 10 in. (254 mm) by 10 in. (254 mm) grids and serve as fixed points for surface expansion measurements; however, they are occasionally located within the planned testing grid and obstruct impact-echo testing at these locations. These irregularities create discontinuous scan lines and their locations will be noted in test results.

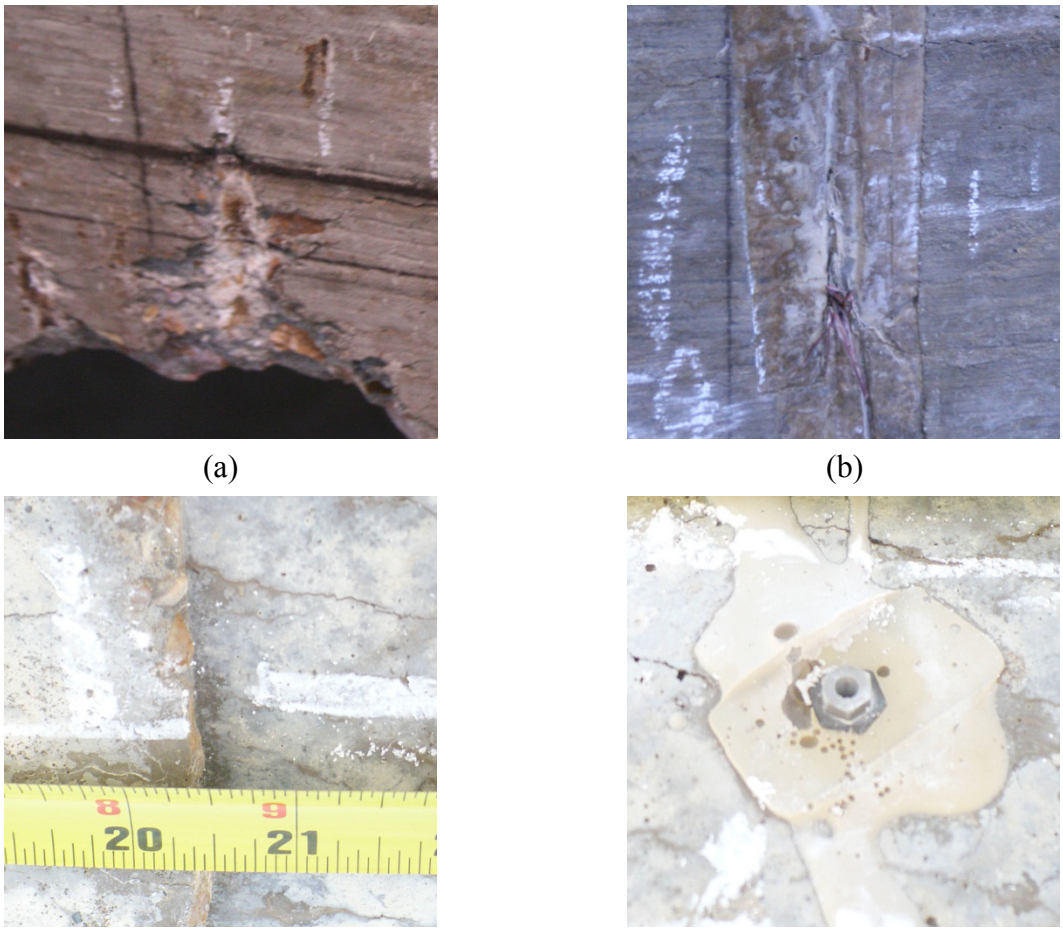

(a) (b)

(c) (d)

Figure 6-4. Examples of Surface Irregularities within the Testing Grid: (a) Damage from Lifting Chains, (b) Rough Surface, (c) Surface Discontinuity, and (d) Demountable Mechanical (DEMEC) Measurement Point.

Data were collected using the commercially assembled point-test impact-echo system that was used in the experiments presented in Chapter 5. Prior to performing point by point scans, C_p is measured using the two transducer method. Forty speed tests are performed on each sample and the sample mean and COV are calculated from the sample data. Though multiple records are captured for each sample, a malfunction in the A/D system introduced an effective noise that did not allow for proper data processing in all records. Only the n records for which the system

malfunction did not interfere with wave speed calculations are included in the calculation of sample statistics. Reflection frequencies are predicted according to Eq. 4-11 and Eq. 4-12 using the sample mean value for C_p and cross-sectional geometry. The cross-sectional dimensions of the specimens give rise to one modal vibration frequency, f_{D1}, calculated according to Eq. 4-11. The frequency, f_{D1}, is the frequency associated with the P-wave reflections from the external boundary at the full depth of the member. The frequency of reflections from an undisturbed steel concrete interface, f_{bonded}, is calculated according to Eq. 4-12. The frequency of P-wave reflections from a steel-concrete interface containing a defect is not calculated, as the physical dimensions of the impact-echo testing system prevent the observation of this portion of the response. Table 6-1 shows the results of the P-wave speed, C_p testing, and frequency predictions. The frequency predictions for sample C8 are shown twice in the table because the value for the depth, D, varies for the different test locations.

Table 6-1. Results of Speed Testing and Frequency Prediction for Samples C7 and C8.

Sample ID	Samples, n	C_p ft/s (m/s)	COV	f_{D1} (kHz)	f_{bonded} (kHz)
C7	23	14,019 (4274)	0.117	3.5	22.7
C8 (B,D)	23	13,515 (4120)	0.016	3.4	21.8
C8 (E,F)	23	13,515 (4120)	0.016	1.7	21.8

Four impact-echo tests are performed at each point on an interval of 1 in. (25.4 mm) within the lap-splice region, ranging from 96 in. (2438 mm) to 204 in. (5182 mm). Due to time constraints on performing the tests prior to the scheduled load testing, this interval was reduced to a range of 96 in. (2438 mm) to 180 in. (4572 mm). Values of 1 μs and 1024 samples are selected for the sampling parameters Δt and N, respectively, resulting in a Δf of 0.976 kHz using Eq. 4-8. The maximum observable frequency due to the value chosen for Δt is 100 kHz using Eq. 4-7.

Figure 6-5 shows an individual impact-echo response signal that is typical of those recorded while performing impact-echo testing on these specific large-scale structures. When compared to the typical signal recorded during small-scale testing (shown in Figure 4-6) a

stronger attenuation of the signal is noticeable, especially given the reduced length of the signal obtained during the large-scale testing. This is due to the decreased role played by the first modal frequency f_{D1}, given that the P-wave travels a longer distance from the impacted surface to the opposite external boundary. The increase in the distance traveled by the wave, as well as the ASR-damaged concrete, cause the wave to attenuate and diverge at a higher rate.

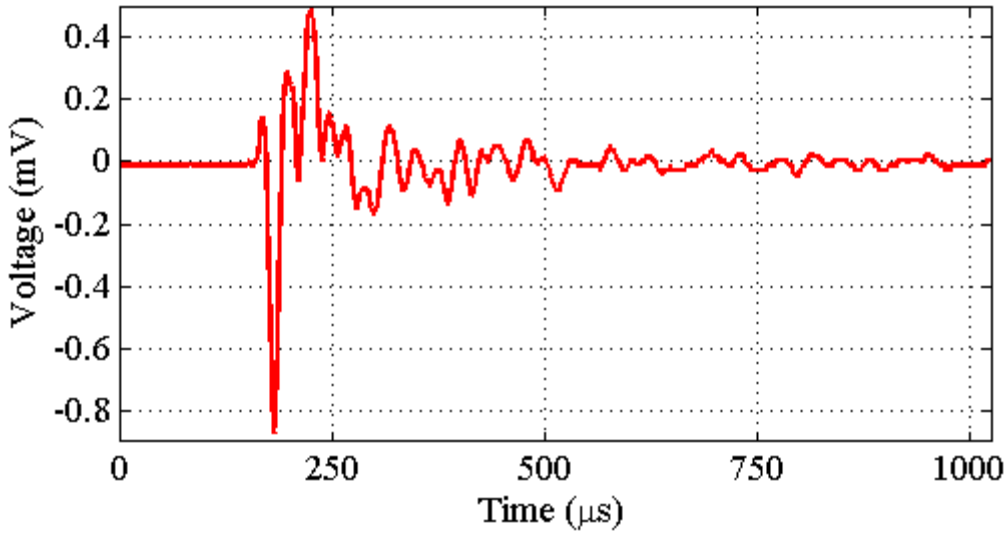

Figure 6-5. Typical Impact-Echo Signal from Testing on Large-Scale Specimens.

Figure 6-6 shows the windowed scan results from testing at position A of sample C7. The locations of surface irregularities are denoted by the red vertical stripes in the color map. There is a significant response at the band of frequencies between 0 kHz and 7 kHz that is attributable to the f_{D1} content. This content is not sharp in amplitude because it is only recorded during a brief portion of the signal. This brevity is due to divergence and attenuation over the long reflection path. The remainder of the frequency spectrum shows a considerable amount of content that is not attributable to a known interface. There is no strong indication of the f_{bonded} content, and consequently, the spectrum cannot be accurately narrowed. This may be an indication that there are ASR-induced defects at the steel-concrete interface; however, the non-attributable content may be acting as noise and masking the f_{bonded} content. This noise may be the result of waves reflecting from the ASR-induced cracks and defects.

Similar results can be seen in the results of scans performed at locations B, C, and D. Figure 6-7 shows the windowed scan results from position B of C7, Figure 6-8 shows the windowed scan results from position C of C7, and Figure 6-9 shows the windowed scan results

from position D of C7. Additionally, the testing performed on C8 yields equally ambiguous results. Figure 6-10 shows the windowed scan results from position C of C8, and Figure 6-11 shows the windowed scan results from position D of C8. Figure 6-12 shows the windowed scan results from position E of C8, and Figure 6-13 shows the windowed scan results from position F of C8.

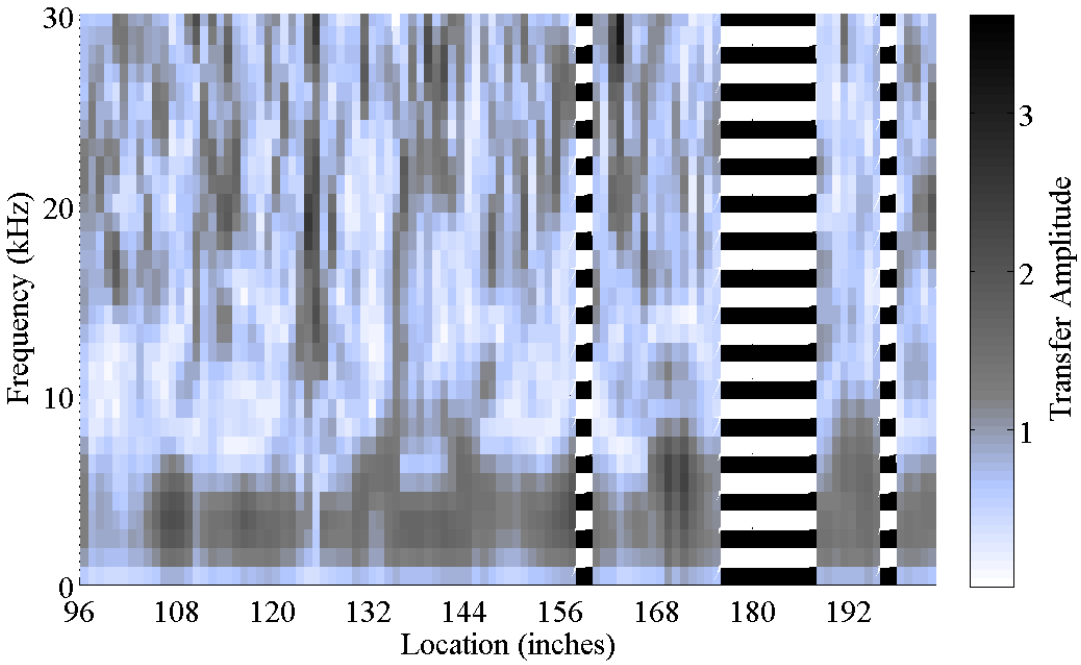

Figure 6-6. Windowed Scan Results from Position A of C7 (1 in. = 25 mm).

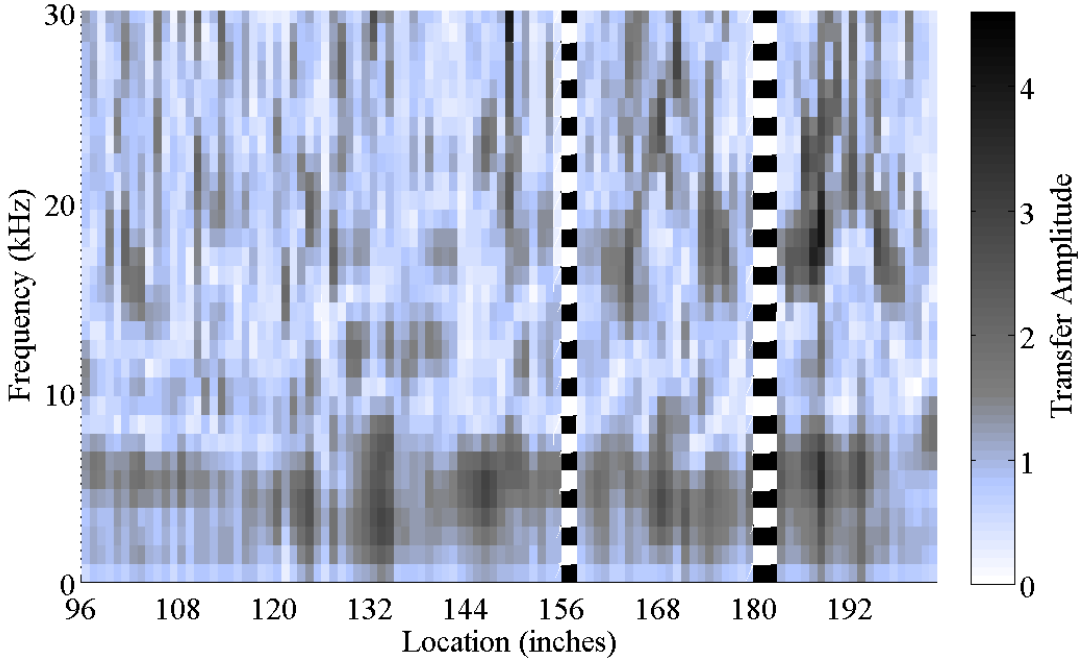

Figure 6-7. Windowed Scan Results from Position B of C7 (1 in. = 25 mm).

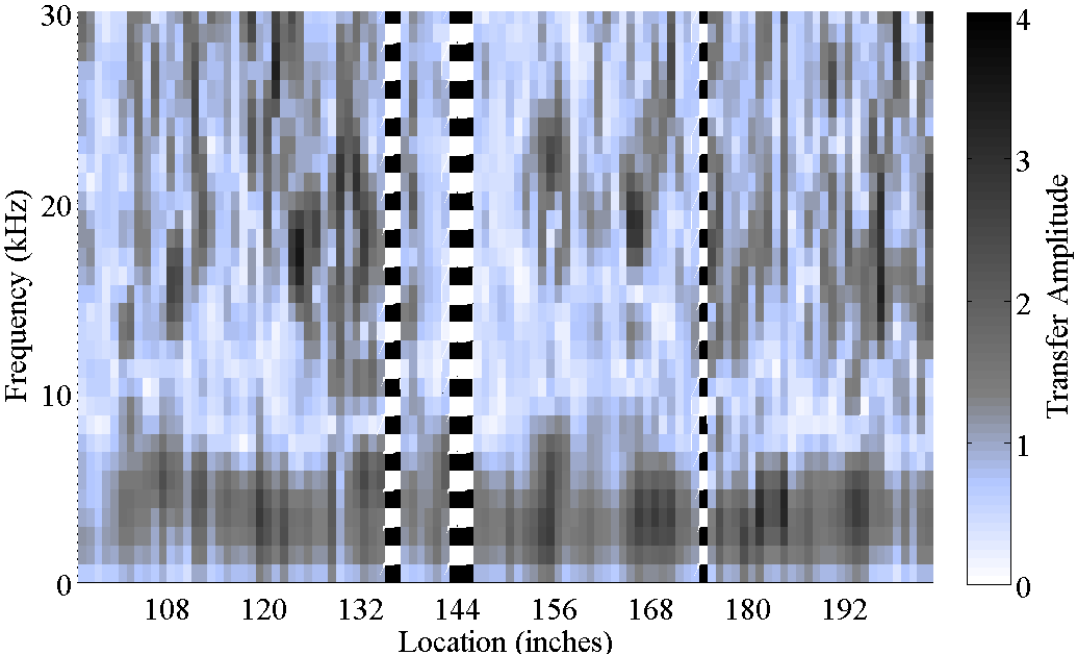

Figure 6-8. Windowed Scan Results from Position C of C7 (1 in. = 25 mm).

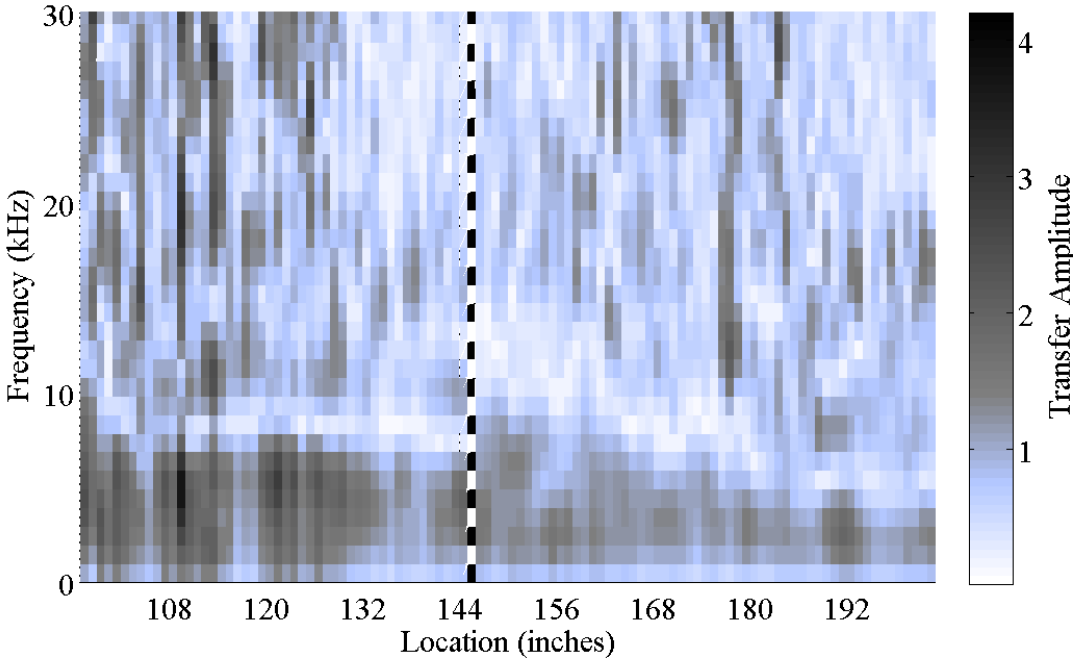

Figure 6-9. Windowed Scan Results from Position D of C7 (1 in. = 25 mm).

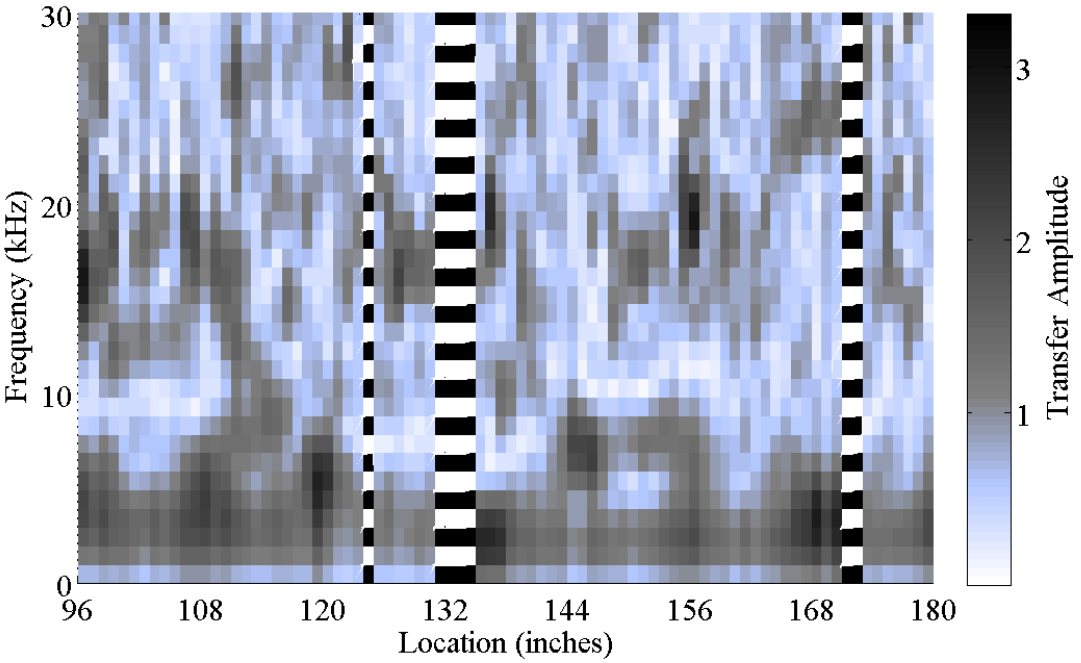

Figure 6-10. Windowed Scan Results from Position C of C8 (1 in. = 25 mm).

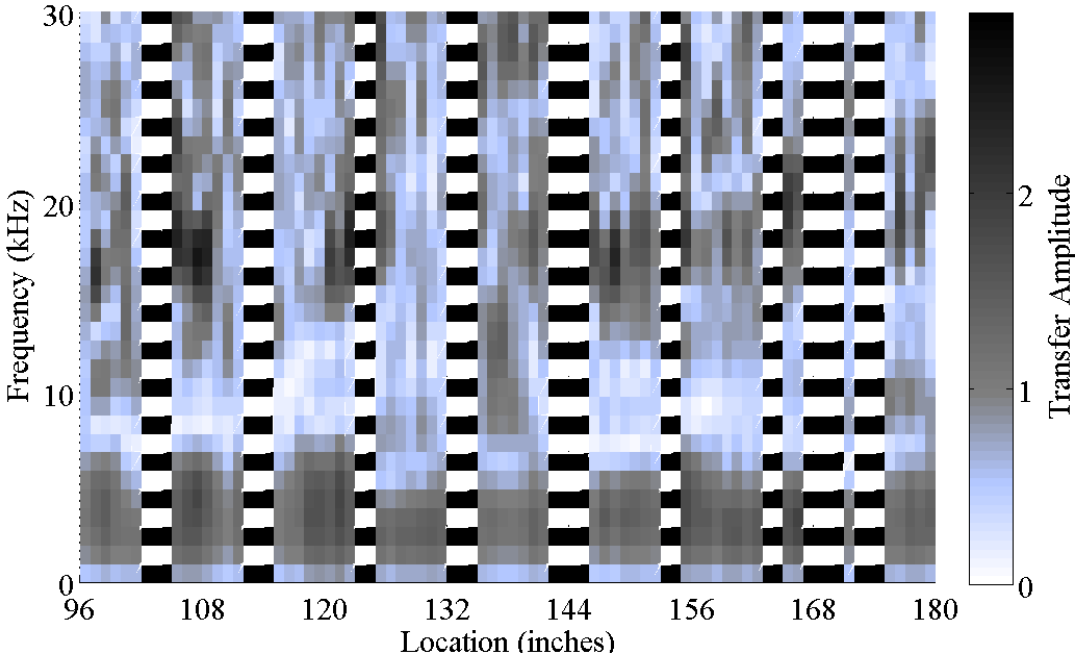

Figure 6-11. Windowed Scan Results from Position D of C8 (1 in. = 25 mm).

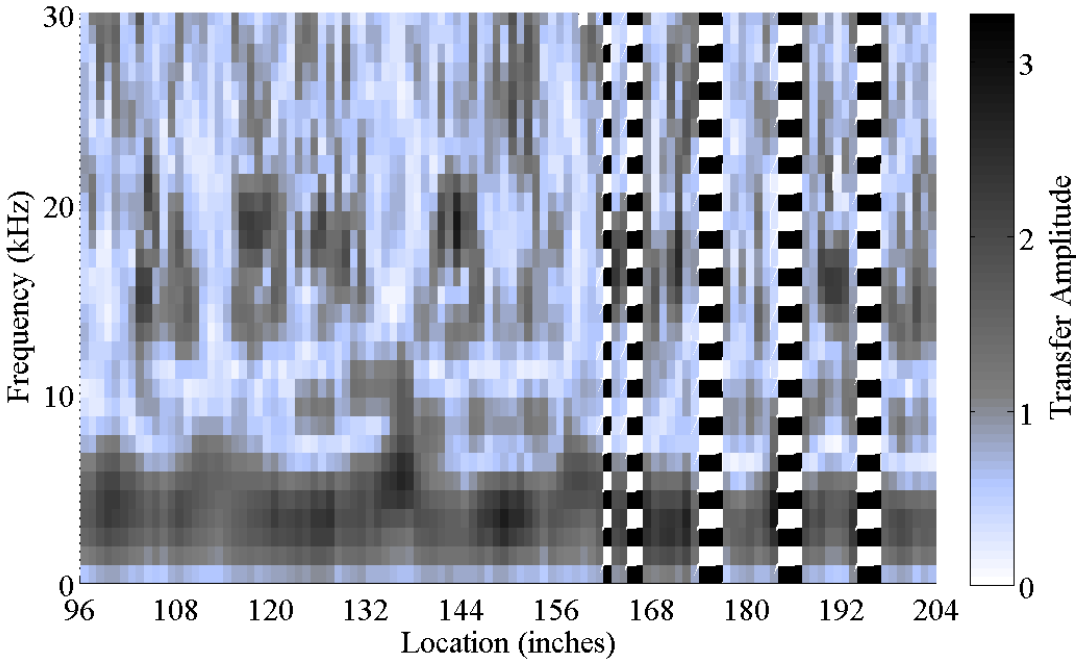

Figure 6-12. Windowed Scan Results from Position E of C8 (1 in. = 25 mm).

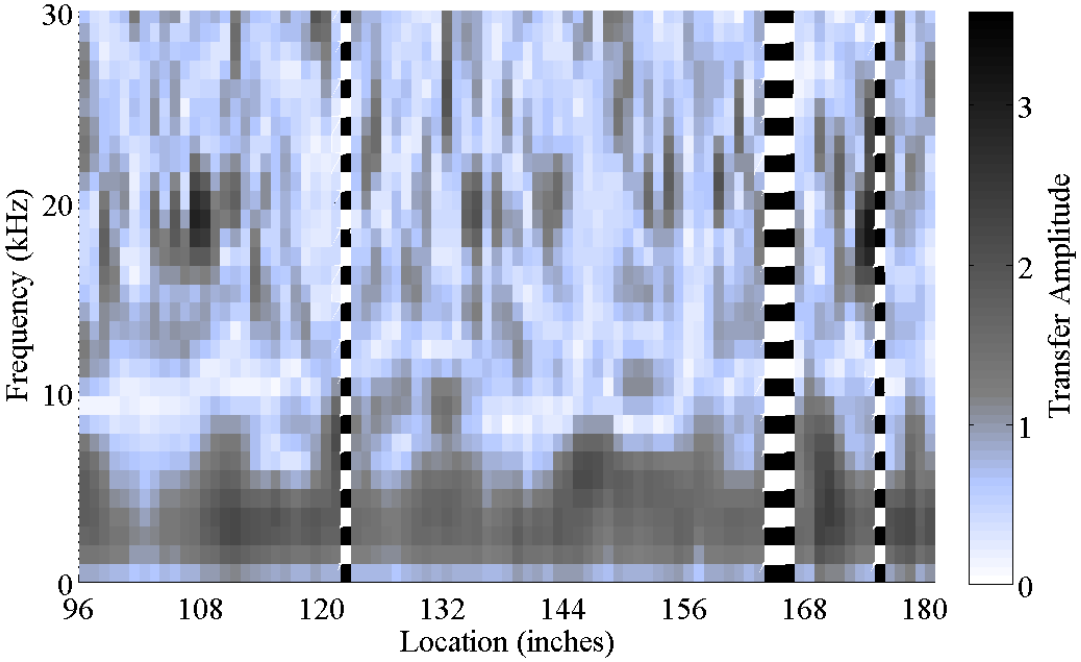

Figure 6-13 Windowed scan results from position F of C8 (1 in. = 25 mm)

6.3 DATA COLLECTED FROM C9 (PRIOR TO LOAD TESTING)

In August 2012, an assessment using impact-echo scanning was performed on one large-scale specimen that had not yet been load tested. At the time of this assessment, a schedule for the load testing of this specimen had not been established. This specimen is referred to as specimen C9. In August 2012, sample C9 was stored at the exposure site for Project 0-5722. Figure 6-14 shows the orientation of all specimens stored at the exposure site in August 2012. The smooth 48 in. (1219 mm) by 300 in. (7620 mm) face is exposed, while the specimens are positions such that 24 in. (610 mm) by 300 in. (7620 mm) faces are difficult to access. The impact-echo assessment was performed in a manner that did not interrupt the exposure schedule set forth by Project 0-5722. In accordance with this constraint, data were collected between watering periods after the surface was dry enough to not damage the electronics of impact-echo equipment. Data were only collected in the early morning hours to avoid overheating the impact-echo equipment.

Figure 6-14. Orientation of C6 and C9 at Exposure Site during Impact-Echo Testing.

Impact-echo testing was performed at 2 in. (51 mm) intervals along the length of C9 from 72 in. (1829 mm) to 108 in. (2743 mm). This length was selected because it contains the minimum amount of developed steel that will be engaged during the load tests performed as a part of Project 0-5722. Two different cross-sectional geometries are present within this interval. Figure 6-15 shows the impact-echo testing locations for sample C9 (a) from 84 in. (2134 mm) to 108 in. (2743 mm) and (b) from 72 in. (1829 mm) to 84 in. (2134 mm). At the time of impact-echo testing, the orientation of sample C9 allowed for testing at locations G, H, I, and J, as shown. An eddy current rebar detector was used to locate the main longitudinal reinforcement. The operator selected the testing locations based on the rebar detector readings in the interval from 72 in. (1829 mm) to 84 in. (2134 mm). When comparing the test locations to the planned rebar locations, there is a clear inconsistency between the rebar detector readings and the construction drawings. This is likely the result of inaccurate rebar detector readings within the heavily reinforced end-region of the large-scale specimens. Because of potential discrepancies in rebar location, tests performed at locations H and I may not yield information about the effects of ASR/DEF on the steel-concrete interface.

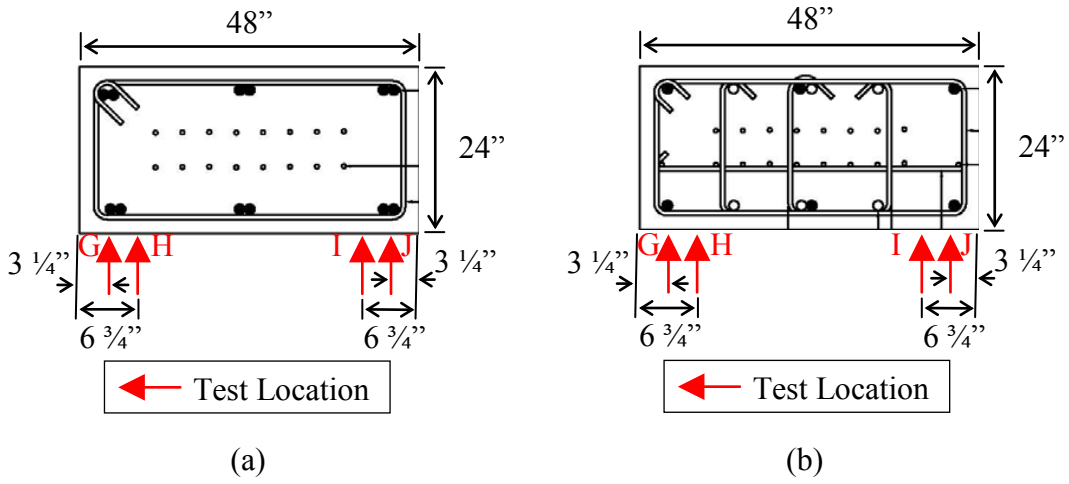

Figure 6-15. Impact-Echo Test Locations on the Cross Section of C9 (a) within the Lap-Splice Region and (b) within the End Region.

Data were collected using the commercially assembled point-test impact-echo system that was used in the experiments presented in Chapter 5. Prior to performing point by point scans, C_p is measured using the two transducer method. Ten speed tests were performed between both adjacent sets of test lines (G-H and I-J) for a total of 20 tests on the sample. Only the n records for which the previously mentioned system malfunction did not interfere with wave speed calculations are included in the calculation of sample statistics. Reflection frequencies are predicted according to Eq. 4-11 and Eq. 4-12 using the sample mean value for C_p and cross-sectional geometry. The cross-sectional dimensions of the specimens give rise to one modal vibration frequency, f_{D1}, calculated according to Eq. 4-11. The frequency, f_{D1}, is the frequency associated with the P-wave reflections from the external boundary at the full depth of the member. The frequency of reflections from an undisturbed steel concrete interface, f_{bonded}, is calculated according to Eq. 4-12. The frequency of P-wave reflections from a steel-concrete interface containing a defect is not calculated, as the physical dimensions of the impact-echo testing system prevent the observation of this content. Table 6-2 shows the results of the speed testing and frequency prediction for C9.

Table 6-2. Results of Speed Testing and Frequency Prediction for Sample C9.

Sample ID	Samples, *n*	C_p ft/s (m/s)	COV	f_{D1} (kHz)	f_{bonded} (kHz)
C9 (G,H)	6	13,292 (4052)	0.099	3.3	20.5
C9 (I,J)	4	12,452 (3796)	0.123	3.1	18.5

Values of 1 μs and 2048 samples are selected for the sampling parameters Δt and N, respectively, resulting in a Δf of 0.448 kHz using Eq. 4-8. The maximum observable frequency due to the value chosen for Δt is 100 kHz using Eq. 4-7. Figure 6-16 shows the windowed scan results from sample C9 at (a) position G, (b) position H, (c) position I, and (d) position J. Locations of surface irregularities are indicated by the dashed vertical stripes. These results contain a wide variety of frequency content at all frequencies of interest. The f_{bar} content cannot be clearly identified in any of the scan results, and consequently, these results cannot be accurately narrowed to show the f_{bar} content. The additional frequency content that prevents the identification of the content of interest may be the result of multiple wave reflections from the ASR-induced cracks and defects in the concrete.

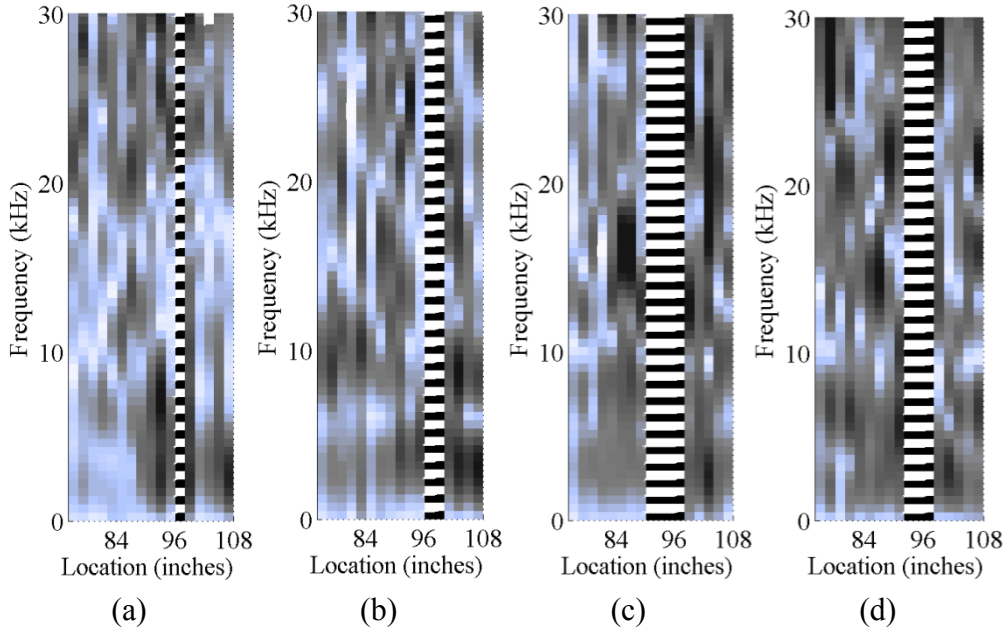

Figure 6-16. Windowed Scan Results from C9 at (a) Position G, (b) Position H, (c) Position I, and (d) Position J (1 in. = 25 mm).

6.4 DATA COLLECTED FROM C6 (2 YEARS AFTER LOAD TESTING)

In addition to the impact-echo testing performed on sample C9, a limited assessment of one previously load-tested large-scale specimen, sample C6, was performed using impact-echo scanning. At the time of testing, sample C6 was stored at the exposure site of Project 0-5722. Figure 6-14 shows the orientation of all specimens stored at the exposure site. As was the case with sample C9, the smooth 48 in. (1219 mm) by 300 in. (7620 mm) face is exposed, while the 24 in. (610 mm) by 300 in. (7620 mm) faces are difficult to access. Testing was performed under the same set of constraints imposed on the testing of sample C9.

Impact-echo testing was performed along the length of sample C6 from 42 in. (1067 mm) to 54 in. (1372 mm). This length, approximately two member depths from both the post-tensioning and the nearest loading point, was selected because it is the point where load-induced bond damage and cracking due to the spreading of the load from the post-tensioning system at the end of the sample should be minimal. The test locations were selected based on the locations of the rebar in the construction drawings. Figure 6-17a shows cross-sectional test locations as they correspond to the geometry of the lap-splice region. The length along which impact-echo scanning was carried out was within the end region of the sample that contains distinctly different reinforcement geometry than expected. Figure 6-17b shows the cross-sectional test locations as they correspond to the cross-sectional geometry of the tested cross-section. Locations G and J are located as before in Figure 6-15. Because tests were not performed directly above reinforcement, tests performed at locations K and L may not yield information about the effects of ASR/DEF on the steel-concrete interface.

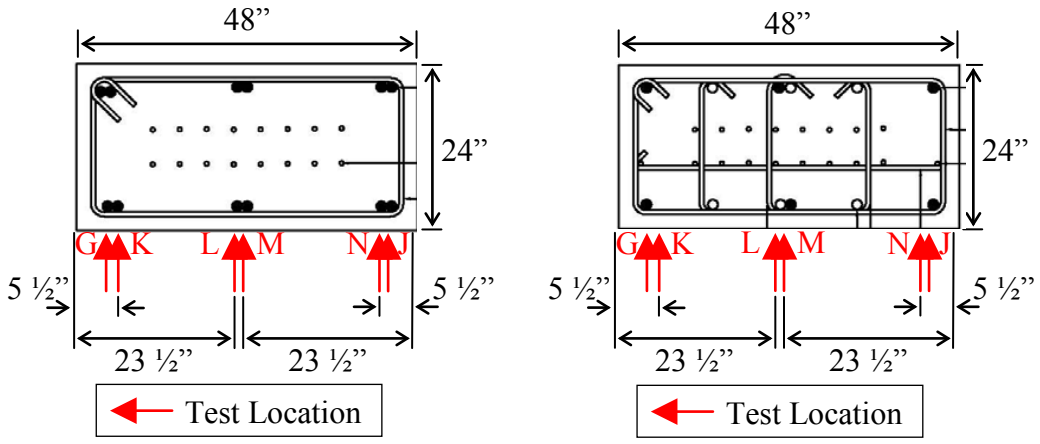

Figure 6-17. Impact-Echo Test Locations on the Cross Section of C6 (a) within the Lap-Splice Region and (b) within the End Region (1 in. = 25 mm).

Data were collected using the commercially assembled point-test impact-echo system that was used in the experiments presented in Chapter 5. Prior to performing point by point scans, C_p is measured using the two transducer method. Ten speed tests were performed at the three adjacent sets of test lines (G-K, L-M, and N-J) for a total of 30 tests on the sample. Only the n records for which the previously mentioned system malfunction did not interfere with wave speed calculations are included in the calculation of sample statistics. Reflection frequencies are predicted according to Eq. 4-11 and Eq. 4-12 using the sample mean value for C_p and cross-sectional geometry. The cross-sectional dimensions of the specimens give rise to one modal vibration frequency, f_{D1}, calculated according to Eq. 4-11. The frequency, f_{D1}, is the frequency associated with the P-wave reflections from the external boundary at the full depth of the member. The frequency of reflections from an undisturbed steel concrete interface, f_{bonded}, is calculated according to Eq. 4-12. The frequency of P-wave reflections from a steel-concrete interface containing a defect is not calculated, as the physical dimensions of the impact-echo testing system prevent the observation of this content. Table 6-3 shows the results of the speed testing and frequency prediction for sample C6.

Table 6-3. Results of Speed Testing and Frequency Prediction for Sample C6.

Sample ID	Samples, n	C_p ft/s (m/s)	COV	f_{D1} (kHz)	f_{bonded} (kHz)
C6 (G,K)	7	13264 (4044)	0.038	3.3	20.1
C6 (L,M)	9	13875 (4230)	0.073	3.5	24.0
C6 (N.J)	6	13342 (4068)	0.018	3.3	22.6

Values of 1 μs and 2048 samples are selected for the sampling parameters Δt and N, respectively, resulting in a Δf of 0.448 kHz using Eq. 4-8. The maximum observable frequency due to the value chosen for Δt is 100 kHz using Eq. 4-7. Figure 6-18 shows the windowed scan results from C6 at (a) position G, (b) position K, (c) position L, (d) position M, (e) position N, and (f) position J. Similar to the results from sample C9, these results contain a wide variety of frequency content at all frequencies of interest. The f_{bar} content cannot be strictly identified in any of the scan results, and consequently, these results cannot be accurately narrowed to show the f_{bar} content. The additional frequency content that prevents the identification of the content of interest may be the result of multiple wave reflections from the ASR-induced cracks and defects in the concrete.

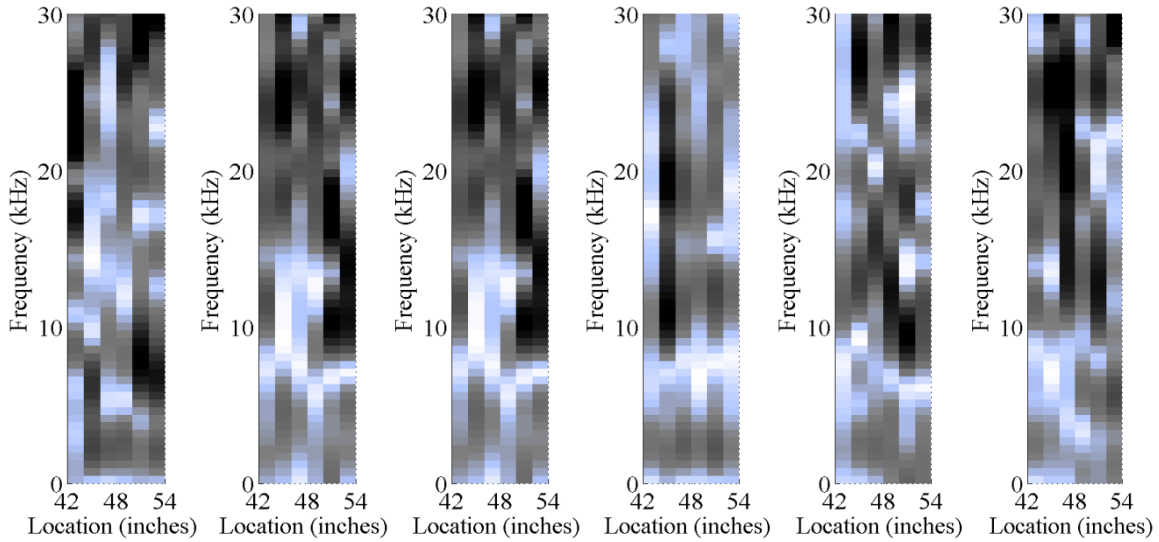

Figure 6-18. Windowed Scan Results from C9 at (a) Position G, (b) Position K, (c) Position L, (d) Position M, (e) Position N, and (f) Position J (1 in. = 25 mm).

6.5 DISCUSSION

Impact-echo testing on the large-scale RC samples affected by ASR in this study results in responses that contain content that cannot be attributed to known interfaces. This content may be the result of multiple P-, S-, and R-wave reflections from ASR-induced surface cracking and internal defects. This noise in the response spectrum may mask the portion of the signal corresponding to reflections from the steel-concrete interface. Given the promise shown by impact-echo in the small-scale experiments of Chapter 5 and that the most complete assessment of the large-scale sample was performed prior to establishing the testing procedure used in Chapter 5 it is possible that with further signal processing not explored within the scope of this project that these results could be used to draw more substantial conclusions about the state of the steel-concrete interface. Additionally, creating a thorough and well-informed testing plan and performing testing according to this plan prior to future load testing may yield more conclusive results.

6.6 SUMMARY

Impact-echo scanning is used to examine four of the large-scale RC lap-splice specimens of Project 0-5722 at different stages of deterioration. Samples C7 and C8 are examined immediately preceding their load testing. Impact-echo data were collected from the lap splice regions of these specimens. The nature of these data leads to ambiguous interpretation due to noise in the response spectrum. One specimen that has not been scheduled for a load test, identified as sample C9, and one specimen that was two years removed from load testing, C6, were also the subjects of a limited impact-echo. Between the testing times, the testing procedure was refined in the laboratory. Additional future testing that incorporates the lessons learned from this project would be beneficial in providing field methodologies for assessing ASR/DEF effects at the steel-concrete interface.

7 SUMMARY, CONCLUSIONS, AND RECOMMENDED FUTURE WORK

The observation of ASR in RC bridge columns and the potential for DEF raised concerns about the safety and reliability of the structures exhibiting these forms of premature deterioration. Expansive products (ASR gel or ettringite formation) may result in a change in steel-concrete bond behavior, a decrease in bond strength in critical areas (such as areas where bars are lapped), and may lead to changes in the flexural capacity and demand of the column. This could result in a reduction in the bridge reliability. As a result, this project responded to the need for a tool to assess the bond in critical areas of RC columns such that the reliability and safety of the structure can be assessed.

To assess the impact of ASR on the bond-slip behavior of steel reinforcement embedded in concrete, this project developed four models for the bond-slip behavior. Each model corresponds to one of four different levels of ASR deterioration in RC columns. The models were calibrated using force-displacement data obtained from four-point load testing of eight large-scale bridge columns subject to different levels of ASR. The data from the load testing of the large-scale bridge columns were provided by TxDOT Project 0-5722. The calibrated models show that some ASR can improve the bond behavior; however, once ASR deterioration reaches a certain level, the bond strength begins to decrease, possibly due to the excessive ASR cracking. This evidence of deterioration in bond behavior emphasizes the importance of having a tool that can assess the state of bonding between concrete and reinforcing steel.

This project considered multiple NDE techniques as potential options to assess the state of the interface between reinforcing steel and concrete. Based on the results of an initial investigation, the impact-echo method was selected for further study. Impact-echo is typically used for other applications, so a thorough literature review was performed to gain an understanding of the physical phenomenon of stress wave propagation in concrete, how it is observed and measured, and how the measurements are processed to reveal the most accurate information about the steel-concrete interface.

A set of small-scale samples with deliberately created defects at the steel-concrete interface were designed and examined using the impact-echo. A range of signal processing techniques was applied to the results of the impact-echo testing on these samples, and the relative merits of each processing technique were determined. Ultimately a testing and data analysis

procedure was developed that clearly allowed for the identification of defects in the controlled samples. Based on the testing of the small-scale samples, it is concluded that:

- Impact-echo is a strong candidate for detecting damage at the steel-concrete interface in ASR-affected structures.
- The incorporation of additional signal processing techniques, such as the simulated transfer function, R-wave removal, and windowing, increases the confidence with which voids can be detected.
- Void thickness has not been shown to significantly affect the detectability of a void.
- Both a reduction in void length and the presence of adjacent steel can reduce the confidence with which a void can be detected.

In addition to examining the small-scale samples, large-scale RC column specimens from TxDOT Project 0-5722 already used for the calibration of the bond-slip model were also examined using impact-echo scanning. However, these examinations were made at different times during the course of TxDOT Project 0-6491. Those that were made with the most complete knowledge on how to employ the procedure were the most limited due to time and access constraints. In general, the results of impact-echo scanning on the large-scale specimens yielded ambiguous results regarding the state of the steel-concrete interface.

TxDOT Project 0-5722 has received an extension to destructively test eight remaining large scale samples in the coming two years to allow additional damage (in particular from DEF) to take place. Therefore, we recommend that the efforts started with TxDOT Project 0-6491 be continued as part of TxDOT Project 0-5722 to further refine and implement the promising procedures developed under TxDOT Project 0-6491 to large scale samples. Continued calibration of bond-slip models with additional data will allow for the assessment of ASR/DEF-related changes in bond behavior at higher levels of deterioration. More complete and well-planned NDE assessments of the remaining large-scale samples will provide more data that may allow the development of a precise NDE testing protocol that is most useful to TxDOT to assess the state of the steel-concrete interface in ASR/DEF affected structures.

REFERENCES

AASHTO, "LRFD Bridge Design Specifications," American Association of State Highway and Transportation Officials, Washington D.C., 2007.

ACI Committee 318, "Building Code Requirements for Structural Concrete (ACI 318-08) and Commentary," American Concrete Institute, Farmington Hills, MI, 2008.

Algernon, D. "Impact Echo Data Analysis Based on Duration and Bandwidth of Signal Components," Journal of the Transportation Research Board, No. 2050, pp. 127-133. 2008.

Algernon, D. and Wiggenhauser, H. "Impact-echo Signal Processing," *Proceedings of the NDE Conference on Civil Engineering*, St. Louis, MO, USA, 2006.

American Society for Testing and Materials, ASTM C1383: Standard Test Method for Measuring the P-wave Speed and the Thickness of Concrete Plates Using the Impact-echo Method, Annual Book of ASTM Standards: Volume 04.02, Concrete and Aggregates. West Conshohocken, PA, 2010.

American Society for Testing and Materials. ASTM C39-01 Standard Test Method for Compressive Strength of Cylindrical Concrete Specimens, Annual Book of ASTM Standards: Volume 04.02, Concrete and Aggregates. West Conshohocken, PA, 2001.

Bracci, J.M., Gardoni, P., Trejo, D., and Eck, K. "Performance of lap splices in large scale column specimens affected by ASR and/or DEF," TxDOT Report No. 0-5722, Texas Transportation Institute, Texas Department of Transportation, Austin, Texas, USA. 2011.

Bracewell, R.N. *The Fourier Transform and its Applications*, McGraw Hill, 2000.

Carino, N. J. "The Impact-echo Method: An Overview," *Proceedings of the 2001 Structures Congress & Exposition*, Washington D.C., May 21-23, 2001.

CEB-FIP. State-of-the-Art Report on Bond of Reinforcement in Concrete, FIB -Féd. Int. du Béton: 1-97. 2000.

Cheng, C.-C, Lin, Y., Hsiao, C.-M., and Chang, H.-C. "Evaluation of Simulated Transfer Functions of Concrete Plate Derived by Impact-echo Method," *NDT&E International*, 40, pp. 239-249. 2007.

Cheng, C.-C. and Sansalone, M. "Effects on Impact-echo Signals Caused by Steel Reinforcing Bars and Voids around Bars," *ACI Materials Journal*, V. 90, No. 5, pp. 421-434. 1993.

Cheng, C.-C. and Yu, C.P. "An Investigation of the Transfer Function of the Impact-echo Response and its Application," *15th World Conference on Nondestructive Testing*, Rome, Italy, 2000.

Folliard, K.J., R. Barborak, T. Drimalas, L. Du, S. Garber, J. Ideker, T. Ley, S. Williams, M. Juenger, M. Thomas, and B. Fournier., "Preventing ASR/DEF in New Concrete : Final Report," Technical Report No. 0-4085-5, The University of Texas at Austin, Center for Transportation Research, 2006.

Guo, Zhenhai, and Xudong Shi. Reinforced Concrete Theory and Analysis. Super Star Digital Library. Qing Hua Da Xue Chu Ban She: Beijing, China. 2003.

Haddad, R.H., and Numayr, K.S. "Effect of alkali-silica reaction and freezing and thawing action on concrete-steel bond," Construction and Building Materials, 21, 428-435. 2007.

Han, J.-H., Kim, Y.-J., Pagnotta, A., and Gardoni, P. "Array-Measurement-Based Algorithm for Detecting Debonded Regions between Concrete Matrix and Steel Reinforcing Bars in Concrete Samples," *41st International Conference and Exposition on Noise Control Engineering*, New York, New York, USA, August 19-22, 2012.

Hsu, K.-T., Cheng, C.-C., and Lin, Y. "Use Impact-echo to Evaluate Bond of Reinforced Concrete Subjected to Early-Age Vibration," *Journal of Solid Mechanics and Materials Engineering*, V.2, 12, 1528-1538, 2008.

Kahan, M. *Non Destructive Structure Evaluation: An Application of Seismic Signal Analysis*, Master's Thesis, Massachusetts Institute of Technology, 2003.

Krautkrämer, J. and Krautkrämer, H. *Ultrasonic Testing of Materials*, 4th Ed., Springer-Verlag, NY.1990.

Malhotra, V.M. and Carino, N.J. *Handbook on Nondestructive Testing of Concrete*, CRC Press, Boca Raton, FL, 2004.

MIRA, Germann Instruments, Web, September 23, 2012 http://www.germann.org/Brochures/Mira.pdf.

Multon, S., Seignol, J.F., and Toulemonde, F. Structural Behavior of Concrete Beams Affected by Alkali-Silica Reaction, ACI Materials Journal. 102(2) 62-76. 2005.

Na, W.-B., Kundu, T., and Ehsani, M. R. "Ultrasonic Guided Waves for Steel Bar Concrete Interface Testing," *Materials Evaluation*, 60, 437-444, 2002.

Nilson, A H. Internal Measurement of Bond-Slip. ACI Journal Proceedings. 69(7): 439-441.

1972.

Olson, L.D., Tinkey, Y., and Miller, P. "Concrete Bridge Condition Assessment with Impact Echo Scanning," Geotechnical Special Publication No. 218, ASCE, 2011.

Owen, M. *Practical Signal Processing*, Cambridge University Press, Cambridge, UK, 2007.

Popovics, J.S. "Effect of Poisson's Ratio on Impact-echo Test Analysis," *Journal of Engineering Mechanics*, Vol. 123, No. 8, August, 1997.

Popovics, J.S., Song, W., Achenback, J.D., Lee, J.H., and Andre, R.F. "One-Sided Stress Wave Velocity Measurement in Concrete," *Journal of Engineering Mechanics*, Vol. 124, No. 12, pp.1346-1353. 1998.

Powanusorn S. and Bracci J. Behavior of Reinforced Concrete Members Prone to Shear Deformations: Part II – Effect of Interfacial Bond Stress-Slip, ACI Structural Journal, 103(5), 747-753. 2006.

Rots, J. G. Computational Modeling of Concrete Structures, PhD dissertation, Delft University of Technology, The Netherlands. 1988.

Sansalone, M. J. and Streett, W. B. *Impact-echo: Nondestructive Evaluation of Concrete and Masonry*, Bullbrier Press, Ithaca, NY, 1997.

Schubert, F. "Geometrical Effects of Impact-echo Testing on Finite Concrete Specimens," *International Symposium for Nondestructive Testing in Civil Engineering*, Berlin, 2006.

Shieh, J., Huber, J.E., Fleck, N.A., and Ashby, M.F. "The Selection of Sensors," *Progress in Materials Science*, 46, 461-504. 2001.

Swamy R., and Al-Asali, M. "Effect of alkali-silica reactions on the structural behavior of reinforced concrete beams," ACI Materials Journal, 86(4): 451-459. 1989.

Tassios, T P. Properties of Bond between Concrete and Steel under Load Cycles Idealizing Seismic Action. National Technical University Athens. Greece. 1982.

Zhu, J. and Popovics, J. S. "Imaging Concrete Structures Using Air-Coupled Impact-echo," *Journal of Engineering Mechanics*, Vol. 133, No. 6, June 1, 2007.